TECHNISCHE UNIVERSITÄT DRESDEN

INSTITUT FÜR KERN- UND TEILCHENPHYSIK

Masterarbeit

zur Erlangung des Hochschulgrades

Master of Science

im Studiengang

Master-Studiengang Physik

Sensitivity study on the Higgs boson's trilinear self-coupling with the VBS ssWWh signal at the ATLAS detector

vorgelegt von

Lisa Marie Lehmann

geboren am 20.08.1999 in Hoyerswerda

Institut für Kern- und Teilchenphysik
Fakultät Physik
Bereich Mathematik und Naturwissenschaften
Technische Universität Dresden

2024

Eingereicht am 24. April 2024

Erstgutachter:	Dr. Frank Siegert
Zweitgutachter:	Jun.-Prof. Dr. Joany Manjarres

Abstract

Since the discovery of the Higgs boson in 2012 great progress has been made in precisely establishing its properties. Nonetheless, numerous questions remain open about the dynamics underlying the electroweak symmetry breaking of the SM, and therefore the nature of the Higgs boson itself. To shed light on this question, this project focuses on studying the Higgs boson's trilinear self-interactions, modeled by κ_λ. The experimental measurement of the Higgs boson's self-coupling strengths will verify the shape of the Higgs potential around its minimum and validate or reject associated theories beyond the Standard Model. While di-Higgs production has been the conventional channel to access κ_λ, this project explores an alternative process: The production of two same-sign W bosons and a Higgs boson via vector boson scattering (VBS ssWWh). This project presents the first detector-level study of VBS ssWWh in final states with the W bosons decaying leptonically and the Higgs boson decaying into b quarks, using the full simulation of the ATLAS detector corresponding to $\sqrt{s} = 13\,\mathrm{TeV}$ and an integrated luminosity of $139\,\mathrm{fb}^{-1}$. With this work, we demonstrated that studies performed by the theory community on the sensitivity of VBS ssWWh to κ_λ underestimated the background-to-signal ratio by a factor of 90. Using a first data-driven estimate on the background in the optimized signal region we perform a statistical analysis with the asymptotic formulae for significance computation with a one-bin histogram not including systematic uncertainties. The limits on κ_λ obtained in this study, $\kappa_{\lambda,Run2} \in [-121, 121]$, show that with this first cut-based signal region selection, the sensitivity of VBS ssWWh to the Higgs trilinear self-coupling is very low. A projection for the HL-LHC expectations of VBS ssWWh constraining κ_λ results in limits of $\kappa_{\lambda,HL-LHC} \in [-54, 54]$. Although these results are outside the validity regime of the employed framework surrounding κ_λ, they should not be taken as a setback but rather as groundwork for the VBS VVH ATLAS analysis. Since VBS ssWWh is a very rare process, its observation will rely on innovative analysis techniques that will be explored in future work.

Zusammenfassung

Seit der Entdeckung des Higgs Bosons in 2012 wurden dessen Eigenschaften präzise erfasst. Dennoch bleiben viele Fragen in Bezug auf die elektroschwache Symmetriebrechung des Standardmodells und damit dem Ursprung des Higgs Bosons offen. Mit dieser Arbeit wird daher der Ursprung des Higgs Bosons durch das Analysieren dessen trilinearer Selbst-Wechselwirkung, modifiziert über κ_λ, näher beleuchtet. Die Messung der Kopplungsstärke dieser trilinearen Kopplung des Higgs Bosons wird es ermöglichen, die genaue Form des Higgs Potentials zu bestimmen und darüber hinaus Aussagen zu treffen über Theorien, die über das Standardmodell der Teilchenphysik hinaus gehen. Derzeit ist der Prozess der Wahl, um κ_λ zu analysieren, die Erzeugung zweier Higgs Bosonen. Mit dieser Studie wird ein alternativer Prozess untersucht: Die Erzeugung von einem Higgs Boson und zwei W Bosonen gleicher Ladung durch Vektorbosonenstreuung (VBS ssWWh). Diese Arbeit präsentiert die erste Analyse auf Detektor-Level von VBS ssWWh, in einem Endzustand, bei dem die W Bosonen leptonisch und das Higgs Boson in zwei b-Quarks zerfallen, mithilfe der vollständigen Simulation des ATLAS Detektors bei einer integrierten Luminosität von $139\,\text{fb}^{-1}$ und $\sqrt{s} = 13\,\text{TeV}$. In dieser Analyse wird gezeigt, dass Studien der Sensibilität von VBS ssWWh auf κ_λ aus der Theorie-Community das Verhältnis von Hintergrund zu Signal um einen Faktor 90 unterschätzt haben. Mit einer Abschätzung des datengetriebenen Hintergrunds in der optimierten Signal Region wird eine statistische Analyse unter Nutzung der asymptotischen Formel zur Signifikanzberechnung mit einem ein-Bin Histogramm und ohne Einbeziehung systematischer Unsicherheiten durchgeführt. Mit der zu erwartenden Eingrenzung von κ_λ in $\kappa_{\lambda,Run2} \in [-121, 121]$ wird ersichtlich, dass mit dieser ersten Cut-basierten Signal Region Optimierung die Sensibilität von VBS ssWWh auf κ_λ sehr gering ist. Eine HL-LHC Projektion dieser Ergebnisse führt zur zu erwartenden Eingrenzung von κ_λ in $\kappa_{\lambda,HL-LHC} \in [-54, 54]$. Obwohl die Ergebnisse dieser Studie außerhalb des Gültigkeitsbereichs des Kappa-Frameworks liegen, sollten sie nicht als Rückschlag sondern als Grundlage für die VBS VVH ATLAS Analyse gesehen werden. Da VBS ssWWh ein sehr seltener Prozess ist, wird seine Messung von innovativen Analysetechniken abhängig sein, die in zukünftigen Projekten erforscht und entwickelt werden.

Contents

1 Introduction

Physicists are driven by the search for answers to fundamental questions about the world surrounding us. That is why the dream of having one theory describing everything, a Grand Unified Theory, has existed for decades. The Standard Model of elementary particles (SM) was a quantum leap toward that goal by combining multiple sub-theories that describe three out of the four known fundamental interactions: the electromagnetic interaction, the weak interaction and the strong interaction. Constructed in the 1960s and 1970s, the SM is the best theory particle physicists have so far to describe and predict the interactions of elementary particles. Over the last 50 years, many of the SM predictions have been confirmed. With the discovery of the Higgs boson in 2012 [1], all predicted particles of the SM were observed. Despite its great success, the SM cannot explain several cosmological observations like the dark matter content of the universe [2] or the matter anti-matter asymmetry [3]. Additionally, the SM is unable to describe gravity or the origin of neutrino masses. The field of particle physics thus finds itself in a precision era. Every prediction of the SM is studied to very high accuracy in order to detect the slightest deviations through which extension of the SM might become possible.

A fundamental concept of the SM is Electroweak Symmetry Breaking (EWSB), describing the transition of the Higgs field from a symmetric ground state to an asymmetric ground state. In this way, EWSB triggers a mechanism that gives most particles their mass and provides an additional massive boson, the Higgs boson. The trilinear and quartic self-couplings of the Higgs boson are another direct result of this mechanism. While properties like the Higgs boson's mass, the Higgs field's ground state, or the electroweak mixing angle have already been studied in great detail, the exact value of the coupling strengths of the Higgs boson's self-interactions is unknown.

The trilinear coupling strength λ_{hhh} of the Higgs boson is a fascinating parameter of the SM, as it appears as a key aspect in theories beyond the SM. For example, the theory of baryogenesis attempts to explain the observed asymmetry of matter and antimatter in the universe. Its main assumptions are that λ_{hhh} is larger than its SM prediction and that the phase transition during EWSB emitted gravitational waves. Such theories allow for collaboration between scientists studying both the very small and the infinitely large, from collision experiments as well as astronomical experiments like LISA [4].

In order to probe such theories very high energies are required. The Large Hadron Collider (LHC) is the world's largest collider, reaching new energies never achieved before [5]. It was built with the purpose of discovering the Higgs boson, now the focus shifted to high-precision measurements and searches for new physics. One of the four large detectors recording the proton-proton collisions at the LHC is the ATLAS detector [6].

Currently, studies on the very rare Di-Higgs production processes try to constrain the value of κ_λ with data recorded with the ATLAS detector. Those studies use advanced analysis techniques like machine learning and suggest that the value of κ_λ must be between -1 and 6 (or so). However, an observation of Di-Higgs production or the precise value of κ_λ will not be possible with the data obtained until 2018 due to limited statistics.

Since the studies on Di-Higgs production are very involved and complicated, we look for new ways to access the trilinear or quartic self-coupling of the Higgs boson.

In this work, we model possible deviations to its value predicted by the SM with the parameter κ_λ with $\kappa_\lambda = 1$ corresponding to the SM prediction of the coupling strength. Different theoretical studies [7],[8],[9] suggested that a triboson production process of WWh via vector boson scattering (VBS) might deliver competitive and thus complementary limits on κ_λ to current Di-Higgs analyses. These intriguing estimates prompted the idea for this study: explore the sensitivity of the WWh process to κ_λ by performing preliminary studies on simulated proton-proton collision data.

In this work, we study the production of two same-charged[1] W bosons and one Higgs boson via vector boson scattering, which we refer to as *VBS ssWWh*. The VBS ssWWh process is a very complex structure with eight final state particles. Due to its specific composition of four jets[2], two of which originate from b-quarks, two leptons and two neutrinos we expect to have only a few irreducible background processes[3]. The main challenge in studying VBS ssWWh will be to suppress background processes that mimic the VBS ssWWh detector signature with misidentified leptons.

This study is the first to explore the VBS ssWWh signature on detector-level, providing a more realistic estimate of the advantages and challenges of this channel.

In chapter 2 we give an introduction to particle physics, where we present the SM and the VBS ssWWh process. We conclude that chapter by explaining how the SM can be extended via effective field theories.

The most important tool of experimental physics is the experiment. Chapter 3 introduces the ATLAS detector at the Large Hadron Collider and the concept of Monte Carlo Simulations of proton-proton collisions. We also give a brief overview of the statistical tools needed in data analysis.

In chapter 4 we acquaint ourselves with the more technical study of VBS ssWWh using Monte Carlo Simulations that do not account for the effects of the detector yet.

Finally, we perform an analysis of VBS ssWWh and possible background processes with Monte Carlo simulated samples at detector-level in chapter 5. We conclude this chapter with an estimate of the sensitivity of VBS ssWWh to κ_λ.

Chapter 6 summarizes and discusses the study we performed on VBS ssWWh and concludes with an outlook on future studies.

[1] We will refer to this also as same-sign.
[2] A jet describes a cone of particles produced in the hadronization process of quarks.
[3] The only background processes we would have if detectors were perfect.

2 Introduction to Particle Physics

The Standard Model of particle physics is the best theory we have so far to describe and predict the interactions of elementary particles of our universe. Section 2.1 presents these fundamental particles and the rules by which they interact with each other, in particular the theoretical framework behind this phenological approach. In section 2.2 we introduce the *VBS* $ssWWh$ process this study focuses on. Finally, we have a look at what could be beyond the SM in section 2.3.
This chapter has been written with the help of [10],[11],[12] and [13].

2.1 Standard Model of Particle Physics

The Standard Model (SM) is a theory describing the interactions of the fundamental particles of our universe. Although the symmetries from which the interactions arise are the more fundamental concepts, we first establish the particle content to get a more compact view of the SM.

The particles described by the SM are elementary, meaning not composed, particles shown schematically in Figure 2.1. They are grouped according to their characteristic properties. In general, particles with integer spin are called bosons and particles of half-integer spin are called Fermions. The fundamental building blocks of matter consist of Fermions with $s = \frac{1}{2}$. If these spin-$\frac{1}{2}$ particles have an integer electromagnetic charge they are called leptons while those with non-integer electromagnetic charge are called Quarks. Quarks and leptons also carry the weak charge I_W^3 while Quarks additionally carry the strong color charge.[1]
There exist 3 generations of Fermions in the SM, where each generation is a more massive copy of the previous one. The number of generations is not a parameter of the SM but an experimental result.
In addition, there exists for each particle an anti-particle which has the same properties as the particle but carries the opposite charges.

The three fundamental forces described by the SM manifest themselves as interactions between particles via the exchange of a boson. Since these mediators have a spin $s = 1$ they are also called Vector bosons[2]. The electromagnetic interaction is mediated by the chargeless and massless photons. There exist 8 types of massless gluons of different color charge that are responsible for the strong interaction. The mediators of the weak interaction are the

[1]Particle physicists often refer to particles with a charge equal to zero as chargeless or not carrying that charge.
[2]The fields of the bosons transform like four-vectors, hence the name vector boson.

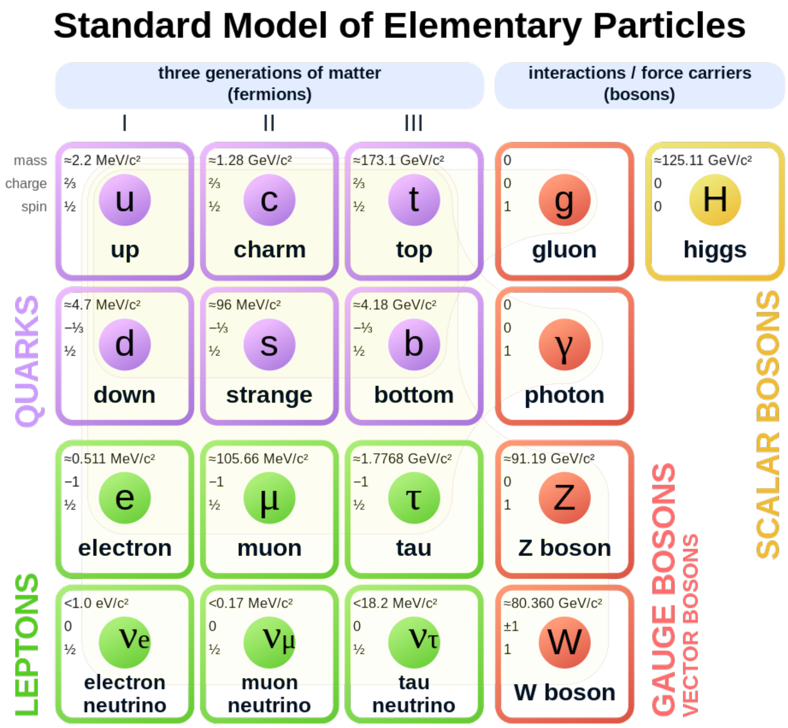

Figure 2.1: Standard Model of Elementary Particles: the 12 fundamental fermions and 5 fundamental bosons. Brown loops indicate which bosons (red) couple to which fermions (purple and green) The charge only refers to the electromagnetic charge. Graphic taken from [14].

electromagnetically neutral Z boson of mass $m_Z = 91.2\,\text{GeV}$ and the electromagnetically charged $W^{\pm}$ bosons of mass $m_W = 80.4\,\text{GeV}$.

Particles only participate in an interaction, i.e. couple to the interaction's mediator, if they carry the corresponding charge. For example, Quarks interact via all three interactions, while electromagnetically neutral leptons, called Neutrinos, only take part in the weak interaction. This is shown by the shaded areas in Figure 2.1.

An elementary particle not mentioned yet is the Higgs boson, which is a scalar, spin 0 boson. It has a special position in our scheme of elementary particles since it is not the mediator of a fundamental interaction in a strict sense. It is the manifestation of the Higgs Mechanism which is the prevalent explanation for the mass of particles and is therefore explained below in more detail.

2.1.1 Symmetries and Lagrangians

The SM is a Quantum Field Theory (QFT). It describes the evolution of quantum fields with their respective equations of motion. In such a theory the dynamics of the system are described via a Lagrangian density $\mathcal{L} = \mathcal{T} - \mathcal{V}$, defined as the kinetic minus potential energy density of the system in question. A system can be described by its underlying symmetries.

Such a symmetry is a transformation of the fields that does not change the evolution of the physical system and as such leaves the Lagrangian[3] invariant.

The SM combines the quantum field theories of the strong interaction (Quantum Chromodynamics - QCD), the weak theory and the electromagnetic interaction (Quantum Electrodynamics - QED). The combination of these QFTs is described with a local $SU(3)_C \times SU(2)_L \times U(1)_Y$ symmetry. That means the Lagrangian this QFT is supposed to stay invariant under local gauge transformations of the quantum fields Ψ:

$$\Psi \to \Psi \cdot \exp\left(ig \sum_a T^a \theta^a(x) \right) \tag{2.1}$$

where T_a is a generator of the corresponding symmetry, g its gauge-coupling strength and $\theta(x)$ a local phase.

In QCD the generators of the symmetry are the unitary 3×3 Gell-Mann-Matrices, the generators for the weak interaction are the unitary 2×2 Pauli-Matrices and QED's generator is $Q \in \mathbb{R}$.

In order to ensure invariance under the transformation (2.1) the covariant derivative D^{mu} defined in equations (2.2) must be introduced The covariant derivative D^μ depends on the bosonic gauge field(s) W^μ, whose transformation is shown in equation (2.3). As a side effect, we introduce interaction terms with the gauge fields when trying to keep the Lagrangian invariant under symmetry transformations.

$$D^\mu = \partial^\mu + ig \sum_a T^a W^{\mu,a}(x) \tag{2.2}$$

with

$$W^{\mu,a} \to W^{\mu,a} - \partial^\mu \theta^a - g f^{abc} \theta^b W^{\mu,c} \tag{2.3}$$

In QED the structure constant is $f^{abc} = 0$ since it is a $U(1)$ symmetry and has only one (thus commuting) generator.
To sum up: for the SM to be a QFT that is gauge invariant under local phase transitions we need to transform the quantum fields and introduce a covariant derivative depending on the gauge fields which have to be transformed at the same time as the quantum fields. It is important to note that at this stage in the development of the theory, the bosons responsible for mediating particle interactions are still massless.

How do charges play into this, since we said above that they are relevant to determine in which interactions particles can take part? Noether's theorem states that every continuous symmetry of the Lagrangian leads to a conserved current. These currents can be identified as charge densities, thus revealing the conserved quantities of our theory: color charge (QCD), electromagnetic charge (QED), weak isospin and weak hypercharge. The latter is the combination of weak isospin and electric charge $Y_W = 2(Q - I_W^3)$ as a result of the electroweak unification.

[3] More precisely, symmetry transformations leave the action $S = \int \mathcal{L}\, dx$ invariant.

The overall structure of the SM can be thought of as follows: It is a theory of the fundamental interactions, where the rules of the interactions follow from specific symmetries. We describe them using quantum fields, with their excitations corresponding to the above introduced elementary particles. These symmetries are generated by the characteristic charges of the elementary particles, which therefore need to be conserved. Figure 2.2 underlines this idea.

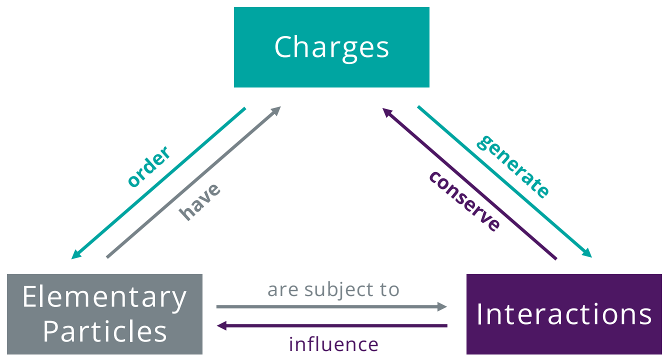

Figure 2.2: Graphic underlining the fundamental concepts of the SM, adapted from [13].

2.1.2 Electroweak Theory

The electromagnetic and weak interactions can be combined into an electroweak theory which covers the local $SU(2)_L \times U(1)_Y$ gauge symmetry of the SM. The three Pauli-Matrices of the weak SU(2) provide us with three gauge bosons $W_1^\mu, W_2^\mu, W_3^\mu$. The U(1) symmetry has only one gauge boson B^μ. These bosons do not directly correspond to the physical bosons, but linear combinations of them do:

$$W^{\pm,\mu} = \frac{1}{\sqrt{2}}(W_1^\mu \mp iW_2^\mu) \tag{2.4}$$

$$A^\mu = B^\mu \cos\theta_W + W_3^\mu \sin\theta_W \tag{2.5}$$

$$Z^\mu = -B^\mu \sin\theta_W + W_3^\mu \cos\theta_W \tag{2.6}$$

where θ_W is the weak mixing angle with $\sin^2\theta_W \approx 0.2$ and A^μ corresponds to the photon field.

With the experiment by Wu in 1957 [15] it became apparent that weak and thus electroweak interactions do not conserve parity[4]. In the electroweak theory, this is implemented through

[4] space-time mirror symmetry with parity operator γ_0.

the inclusion of the chiral projection operator γ_5 as the vertex factor of weak charged-currents. In general, a field u can be split into its left- and right-handed components:

$$u = u_L + u_R = P_L u + P_R u = \frac{1}{2}(1-\gamma^5)u + \frac{1}{2}(1+\gamma^5)u \tag{2.7}$$

Only left-handed fermions and right-handed anti-fermions take part in the weak interaction. These projections thus need to be included in the particle content of the SM Lagrangian $\mathcal{L}_{SM}$.
The left-handed fermions are grouped into SU(2)$_L$-doublets of weak isospin $I_W = \frac{1}{2}$ while the right-handed fermions act as singlets of $I_W = 0$. This means that gauge transformations as shown in equation (2.1) only act on left-handed particles and right-handed anti-particles.

$$\begin{pmatrix}\nu_e\\ e\end{pmatrix}_L, \begin{pmatrix}\nu_\mu\\ \mu\end{pmatrix}_L, \begin{pmatrix}\nu_\tau\\ \tau\end{pmatrix}_L, \begin{pmatrix}u\\ d\end{pmatrix}_L, \begin{pmatrix}c\\ s\end{pmatrix}_L, \begin{pmatrix}t\\ b\end{pmatrix}_L \tag{2.8}$$

$$(e)_R, (\mu)_R, (\tau)_R, (\nu_i)_R, (u)_R, (c)_R, (t)_R, (d)_R, (s)_R, (b)_R \tag{2.9}$$

The electroweak part of the SM Lagrangian, omitting for readability all but the first lepton generation, can be written as

$$\begin{aligned}\mathcal{L}_{EW} = {} & i\overline{\begin{pmatrix}\nu_e\\ e\end{pmatrix}}\gamma^\mu D_\mu \begin{pmatrix}\nu_e\\ e\end{pmatrix} + i\overline{\begin{pmatrix}u\\ d\end{pmatrix}}\gamma^\mu D_\mu \begin{pmatrix}u\\ d\end{pmatrix} \\ & + i\overline{(e)_R}\gamma^\mu D_\mu (e)_R + i\overline{(d)_R}\gamma^\mu D_\mu (d)_R + i\overline{(u)_R}\gamma^\mu D_\mu (u)_R + \ldots \\ & - \frac{1}{4}W^a_{\mu\nu}W^{a,\mu\nu} - \frac{1}{4}B_{\mu\nu}B^{\mu\nu}\end{aligned} \tag{2.10}$$

Here $W^a_{\mu\nu}$ is the covariant field strength tensor of the SU(2) weak gauge bosons and $B_{\mu\nu}$ the covariant field strength tensor of the U(1) gauge boson.

We now write the covariant derivative shown in equation (2.2) explicitly in terms of the electroweak gauge fields and their corresponding generators:

$$D^\mu = \partial^\mu + ig_W \sum_{a=1}^{3} T^a W^{\mu,a}(x) + ig_Y Y B^\mu \tag{2.11}$$

Using equations (2.1) to (2.3) we find $W^a_{\mu\nu}$ and $B_{\mu\nu}$ to be:

$$B_{\mu\nu} = \partial_\mu B_\nu - \partial_\mu B_\nu \tag{2.12}$$

$$W^a_{\mu\nu} = \partial_\mu W^a_\nu - \partial_\nu W^a_\mu - g_W f^{abc} W^b_\mu W^c_\nu \tag{2.13}$$

Products of two weak field strength tensors as seen in the Lagrangian $\mathcal{L}_{EW}$ in equation (2.10) will result in products of W^μ fields of different orders. In QFTs products of fields correspond to interaction terms. Hence, terms with products of three and four W^μ fields correspond to the self-interactions of those gauge bosons shown in Figure 2.3.

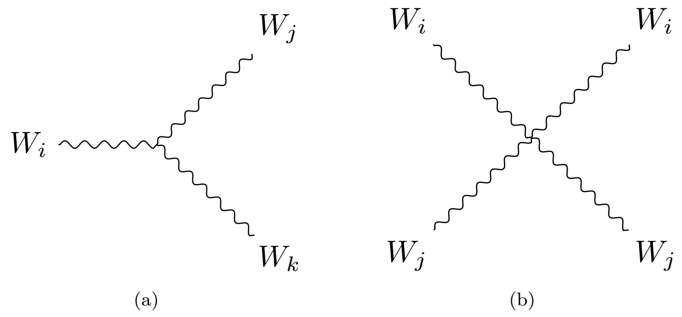

Figure 2.3: Feynman diagrams showing the triple (a) and quartic (b) self-interactions of the SM gauge bosons.

2.1.3 The Higgs Mechanism

All the particles introduced above are as of now massless. In QFTs, mass terms are introduced as terms quadratic in the relevant field,
$\mathcal{L}_{mass,fermion} = m\overline{\Psi}\Psi$ and $\mathcal{L}_{mass,boson} = -\frac{1}{2}m^2 V^\mu V_\mu$.
Such an expression is not yet part of our Lagrangian, see for example the electroweak Lagrangian of equation (2.10). A naive approach would be to simply add those terms to $\mathcal{L}_{SM}$. Only looking at the gauge transformation of the bosonic fields shown in equation (2.3) we see that the product of such two transformed fields will break gauge invariance. We need a mechanism that dynamically induces mass terms into our Lagrangian.

Proposed in 1964/1966 by Higgs, Englert and Brout (and Kibble, Hagen, Guralmik), separately [16],[17], a phase transition mechanism like Spontaneous Symmetry Breaking (SSB) with a gauge invariance violating ground state could generate the mass terms of the bosonic fields.

Before diving into the Higgs mechanism of the SM, we introduce this concept with the example of a U(1) symmetry and a complex scalar field $\Phi = \frac{1}{\sqrt{2}}(\Phi_1 + i\Phi_2)$ in a potential $V(\Phi)$. The Lagrangian constructed for this case is invariant under the transformations shown in equations (2.1) to (2.3):

$$\mathcal{L} = -\frac{1}{4}F_{\mu\nu}F^{\mu\nu} + (D_\mu\Phi)^* (D^\mu\Phi) - V(\Phi) \tag{2.14}$$

$$V(\Phi) = \mu^2\Phi^2 + \lambda\Phi^4 \tag{2.15}$$

$F^{\mu\nu}$ is the field strength tensor of the vector field A^μ and D^μ the covariant derivative $D^\mu = \partial^\mu + igA^\mu$.
The first part of $\mathcal{L}$ corresponds to the kinetic term for A^μ while the term with the covariant derivatives corresponds to the kinetic term for Φ as well as the interaction between Φ and A^μ.

If $\mu^2 > 0$ and $\lambda > 0$, the minimum of the potential, also called vacuum expectation value (vev) is at $\Phi^0 = 0$ and expansions around the minimum will lead to no new information.

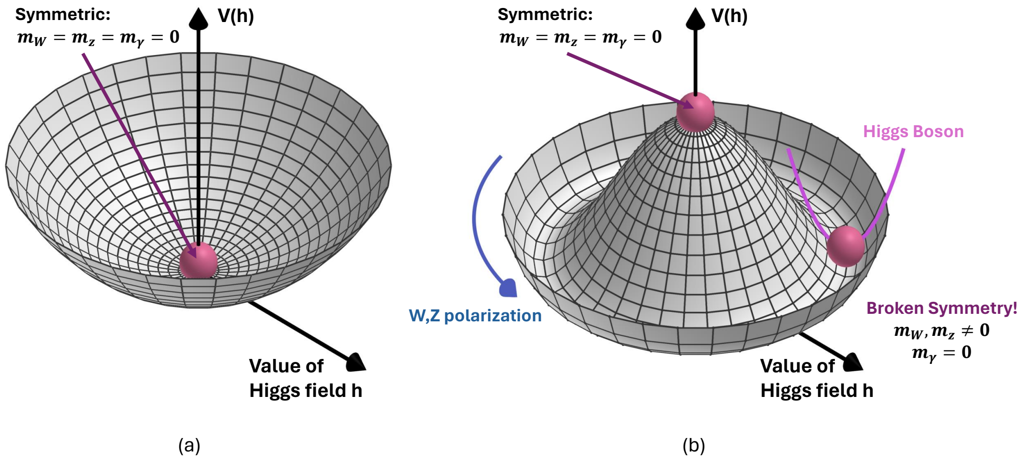

Figure 2.4: For a toy model with a complex scalar field, the Higgs potential can be drawn as shown in the case of $\mu^2 > 0$, $\lambda > 0$ (a) and $\mu^2 < 0$, $\lambda > 0$ (b). In (a), the overall potential shape and ground state are symmetric. Excitations around the minimum lead to no new information. In (b), the overall potential shape is symmetric, but choosing one specific minimum value breaks this symmetry. Excitations in the direction of the potential slope correspond to the Higgs boson. Expanding along the potential well gives mass / longitudinal polarization to the gauge bosons W, Z. Adapted from [18].

If now $\mu^2 < 0$ and $\lambda > 0$, there are multiple possible non-zero values for the minimum (like the circular valley around the bottom of a Mexican hat). We choose the minimum at

$$\Phi^0 = \Phi_1^0 + i\Phi_2^0 = v = \sqrt{\frac{-\mu^2}{\lambda}} \tag{2.16}$$

so that the vev is real.

Expanding around the minimum $\Phi(x) = \frac{1}{\sqrt{2}}(v + \eta(x) + i\chi(x))$ we find the Lagrangian to be

$$\begin{aligned}\mathcal{L}_{Higgs} = &\frac{1}{2}(\partial_\mu \eta)(\partial^\mu \eta) - \lambda v^2 \eta^2 \\ &+ \frac{1}{2}(\partial_\mu \chi)(\partial^\mu \chi) + gvA_\mu(\partial^\mu \chi) \\ &- \frac{1}{4}F_{\mu\nu}F^{\mu\nu} + \frac{1}{2}g^2 v^2 A_\mu A^\mu \\ &- V_{int}\end{aligned} \tag{2.17}$$

We see that the field η, used for the expansion in the direction of the potential's slope, obtained mass, while the field χ, used for the expansion along the minima-valley, remained massless. Also, the gauge boson A^μ obtained mass. These observations can be explained by two theorems. The Nambu-Goldstone Theorem [19],[20] states that every spontaneously broken continuous symmetry creates massless spin 0 Goldstone bosons. In our example, the field χ was the resulting Goldstone boson. The Higgs mechanism now states that if this broken symmetry was actually a local gauge symmetry a massive scalar boson would appear. This is what we denoted η but will from now on call the Higgs boson. It is important to note that $\mathcal{L}_{Higgs}$ is still the same Lagrangian as in (2.14), only in the specific minimum configuration it does not obey the U(1) symmetry any longer.

One problem is left to discuss for this example: the degrees of freedom (dof) of the Lagrangian. Before SSB there were 4 dof, the two components of the complex scalar field Φ and the two polarisation states of A^μ. After SSB there are 5 dof, again the two components of Φ but now three polarisation states of A_μ since it became massive.
If we apply a specific gauge transformation, we can eliminate χ from the Lagrangian. In other words, this field χ decouples from η and A_μ and is thus non-physical. We can reinterpret this gauge transformation as χ becoming the longitudinal polarisation state of A_μ. Thus all of the physical fields became massive and the number of dof stays constant. The massive gauge field A_μ can correspond to the known photon in the theory of superconductivity.

The actual Higgs mechanism in the SM is more involved than this example but shares many of its core concepts. Since the electroweak part of the SM obeys a local $\mathrm{U}(1)_Y \times \mathrm{SU}(2)_L$ symmetry, we need to add a weak doublet with two complex scalar fields to the Lagrangian:

$$\Phi = \begin{pmatrix} \Phi^+ \\ \Phi^0 \end{pmatrix} = \frac{1}{\sqrt{2}} \begin{pmatrix} \Phi_1 + i\Phi_2 \\ \Phi_3 + i\Phi_4 \end{pmatrix} \tag{2.18}$$

The scalar part of the Lagrangian looks similar to (2.14), the complex conjugate is now the adjoint of the derivatives and fields. With this scalar part added, the Lagrangian remains invariant under the local symmetry. If $\mu^2 < 0$ and $\lambda > 0$ the potential will have again degenerate minima, the choice of one specific minimum breaks this symmetry. The vev of the Higgs field is then

$$\Phi_0 = \frac{1}{\sqrt{2}} \begin{pmatrix} 0 \\ v \end{pmatrix}. \tag{2.19}$$

In fact, not all symmetries are broken. The Lagrangian is still invariant under transformations of the shape $\Phi_0 \to e^{-i\theta(x)Q}\Phi_0$. The overall $\mathrm{U}(1)_Y \times \mathrm{SU}(2)_L$ is thus broken to the $\mathrm{U}(1)_{EM}$ gauge symmetry of QED. For this reason, the other gauge bosons gain mass, but the photon remains massless.

Following the same procedure as above, expanding around the minimum with $h(x)$ and focusing on the kinetic terms we find

$$\begin{aligned}(D_\mu\Phi)^\dagger(D^\mu\Phi) = \frac{1}{2}(\partial_\mu h)(\partial^\mu h) + \frac{1}{8}g_w^2(W_{1\mu} + iW_{2\mu})(W^{1\mu} - iW^{2\mu})(v+h)^2 \\ + \frac{1}{8}(g_W W_{3\mu} - g'B_\mu)(g_W W^{3\mu} - g'B^\mu)(v+h)^2\end{aligned}. \tag{2.20}$$

We see that there exist now terms quadratic in $W^\pm = \frac{1}{\sqrt{2}}(W_1 \mp iW_2)$ and $Z = g_W W_{3\mu} - g'B_\mu$. The gauge bosons obtained mass. They also couple directly to the Higgs boson as can be seen from terms like $W_\mu^- W^{+\mu} h$. As already assumed, equation (2.20) shows no terms

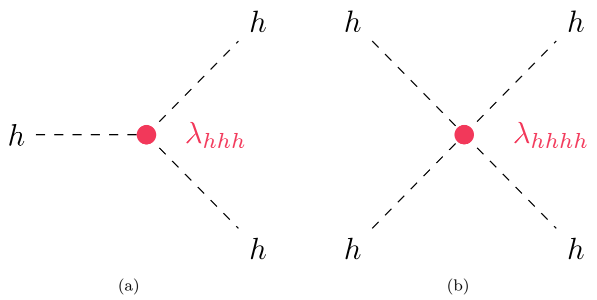

Figure 2.5: Feynman diagrams showing the trilinear (a) and quartic (b) self-interactions of the SM Higgs boson.

proportional to the photon field, which means it stays massless. We conclude that the possibility of coupling to the Higgs field prompts the massiveness of a particle.

When studying the potential part of the Lagrangian expanded around the minimum we find

$$\begin{aligned} V(v+h) &= \frac{\mu^2}{2}(v+h)^2 + \frac{\lambda^4}{4}(v+h)^4 \\ &= \frac{\mu^2}{2}(v^2 + 2vh + h^2) + \frac{\lambda^4}{4}(v^4 + 4v^3h + 6v^2h^2 + 4vh^3 + h^4) \end{aligned} \tag{2.21}$$

The Higgs mass is thus $m_H = 2\lambda v^2 = -2\mu^2$ and the Higgs boson's potential depends on the coupling strengths of its self-coupling

$$V(v+h) \approx \lambda v^2h^2 + \lambda vh^3 + \frac{\lambda^4}{4}h^4 \tag{2.22}$$

To be more explicit, this part of the SM Lagrangian describes the Higgs trilinear and quartic self-interactions, shown in Figure 2.5.

Due to its dependence on v and λ, the Higgs mass is not predicted by the SM. In 2012 a boson with SM-like properties was measured by the ATLAS and CMS collaborations [21],[22] and is assumed to be the SM Higgs boson with a mass of $m_H = 125\,\text{GeV}$.

The fermion masses do not follow directly from the Higgs mechanism. Because of the violating nature of SU(2) a mass term of $\sim m^2\overline{\Psi}\Psi$ does not leave the Lagrangian invariant. The solution to this is to insert manually constructed mass terms into the Lagrangian using Yukawa couplings y_f.

$$\mathcal{L}_m = -y_e[\begin{pmatrix}\overline{\nu_e} & \overline{e}\end{pmatrix}_L \begin{pmatrix}\Phi^+ \\ \Phi^0\end{pmatrix}(e)_R + \overline{e_R}\begin{pmatrix}\Phi^{+*} & \Phi^{0*}\end{pmatrix}\begin{pmatrix}\nu_e \\ e\end{pmatrix}_L] \tag{2.23}$$

This Yukawa coupling leaves the Lagrangian invariant while the vev of Φ still breaks the overall symmetry. The fermion masses are thus not predicted by our theory but can be correctly modeled with the Yukawa parameters y_f which are free parameters of the SM. It is still unclear how Neutrinos acquire their mass - either via a Dirac mass term as above or via a Majorana mass term.

2.2 $W^{\pm}W^{\pm}hjj$ Production via Vector Boson Scattering

According to the SM, not only do fermions interact via the exchange of mediating bosons but bosons themselves are able to interact with each other as shown at the end of section 2.1.2. For example, the SM predicts a quartic vertex of four $W^{\pm}$ bosons, see Figure 2.3, which was first observed in 2017 by the ATLAS and CMS collaborations [23],[24]. The study of such vertices is motivated by the connection of the vector boson's mass to the Higgs mechanism: In regions with high energy, these bosons become more and more similar to the Goldstone bosons as described in the Goldstone-Equivalence Theorem [25]. By determining the relevant parameters (cross-section, coupling strength of Higgs to particles), the Higgs mechanism can be better understood.

But why not study the properties of the Higgs boson directly, to gain direct insights? Equation (2.22) shows that there should exist a trilinear and a quartic coupling of Higgs bosons. Both of these couplings have not been measured yet. We focus in this thesis on the trilinear self-coupling of the Higgs boson. We denote the trilinear coupling strength as λ_{hhh}.

Knowing the exact value of λ_{hhh} will open the door to many new insights. Firstly, since λ_{hhh} is an inherent part of the Higgs potential we will be able to make more accurate predictions of its actual shape. There exist BSM theories of differently shaped Higgs potentials [26] some of which predict states of lower energy than the current vacuum state. Since such a lower minimum of the potential would be more stable than the current one, there would exist a non-zero probability of the Higgs field to transition to that minimum. This process is called vacuum decay of the Higgs field and would result in drastic changes of the particles masses and thus the world surrounding us. With more information on the potential's shape, such considerations could be studied further. Secondly, the value of λ_{hhh} plays an important role in theories trying to explain the matter-antimatter-asymmetry of our universe, such as baryogenesis. In such scenarios, deviations of λ_{hhh} of order $\mathcal{O}(1)$ with respect to the SM prediction are expected [27]. We access deviations on λ_{hhh} by introducing the parameter κ_λ as

$$\kappa_\lambda = \frac{\lambda_{hhh}}{\lambda_{SM}}$$

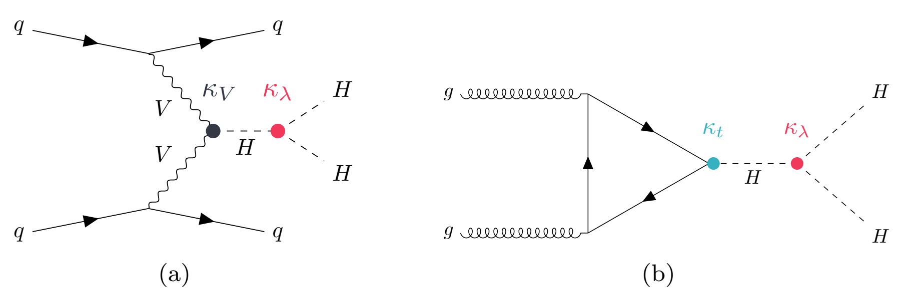

Figure 2.6: Feynman diagram of the gluon-gluon-fusion (a) and vector-boson-fusion(b) Di-Higgs production modes that are sensitive to κ_λ. Graphic taken from [28].

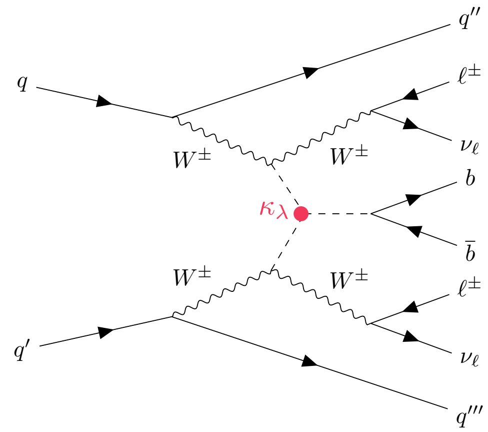

Figure 2.7: Feynman diagram of the signal process VBS ssWWh, which is sensitive to κ_λ.

Currently, the Higgs trilinear coupling is the subject of studies in Di-Higgs production processes, see [29] or [30] as an example, some of which are shown in Figure 2.6.

In this thesis, we explore another approach by embedding the Higgs trilinear coupling into a same-charged W scattering process shown in Figure 2.7. We will abbreviate this process with *VBS ssWWh*.

Specifically, we require the W bosons to decay into a lepton and its corresponding neutrino. We let the Higgs boson decay into a pair of b-quarks, because of this decay's high branching ratio. We explicitly focus on same-charged W scattering since it has a lower irreducible background than opposite-sign W scattering or WZ and ZZ scattering. For example, already opposite-sign W scattering and ZZ scattering can result in the same leptonic final state of 2 opposite-sign leptons and 2 neutrinos while none of the VBS VVH processes produces two same-sign leptons and 2 neutrinos.

A specific signature of this process is the two jets that don't originate from the b-quarks. The incoming quarks radiate off the W bosons and since they don't lose much momentum in this process, their direction of flight does not deviate much from the original one, remaining almost parallel to the beam-pipe. Thus, they end up in opposite forward regions of the detector with a large angular separation between them and a high invariant mass, typically referred to as VBS topology.

Table 2.1 compares the theory-computations of the cross-sections of Di-Higgs production via gluon-gluon fusion [31] and vector boson fusion [32], the measured cross-section of the scattering of two same-sign W bosons [23] to the cross-section of VBS ssWWh, simulated at LO with MadGraph. Although there is only a factor of ten between the cross-section of same-sign W boson scattering and the gluon-gluon fusion Di-Higgs production, the first process has been observed in 2017 while the latter has not been observed so far. In contrast to this, VBS ssWWh is even a factor 50 less probable than the Di-Higgs production mode, which we could explain by the larger amount of required final state objects. That means we

Table 2.1: Cross-section comparison of the theory-computations of the cross-sections of Di-Higgs production via gluon-gluon fusion [31] and vector boson fusion [32], the measured cross-section of the scattering of two same-sign W bosons [23] to the cross-section of VBS ssWWh, simulated at LO with MadGraph.

Process	final state	σ[fb]
ggF HH	$HH \to b\bar{b} + WW \to b\bar{b} + 2l + 2\nu$	0.504
VBF HH	$HH \to b\bar{b} + WW \to b\bar{b} + 2l + 2\nu$	0.028
VBS ssWW	$WW \to 2l + 2\nu$	2.89
VBS ssWWh	$WWh \to b\bar{b} + 2l + 2\nu$	0.011

want to study a very rare process - out of 5000 billion collisions in the ATLAS detector, one collision will produce the VBS ssWWh process. Nevertheless, multiple theory estimations hint at a high sensitivity of VBS ssWWh to κ_λ [7],[8],[9].

2.3 Beyond the Standard Model

Besides the success of the SM describing the data taken at the Large Hadron Collider, observations like the matter and anti-matter asymmetry, among others, cannot be explained within the theory. In the absence of a clear indication of where to look for new physics, the interest of the particle physics community is turning to building extensions of the SM that are as model-independent as possible. With Effective Field Theories (EFTs) we can describe new phenomena in a restricted range of validity, described by the energy bound Λ. S. Todt [33] gives a pedagogical introduction to EFTs and serves as a source for this part. In this EFT approach, we extend the SM Lagrangian by manually adding new field operators as shown in equation (2.24).

$$\mathcal{L}_{EFT} = \mathcal{L}_{SM} + \sum_{n=5}^{\infty} \sum_{i=0}^{N_n} \frac{f_i^{(n)}}{\Lambda^{n-4}} \mathcal{O}_i^{(n)} \tag{2.24}$$

These new operators of dimension n $\mathcal{O}_i^{(n)}$ are constructed from SM fields and obey SM symmetries. $f_i^{(n)}$ are the coefficients of the expansion. Current studies, for example on VBS, include dimension-6 and dimension-8 operators. The low-energy limit of the EFT is the SM, but at higher energies, close to the accessible energy range, new physics might leave traces in the form of small deviations in the tail of some distributions. Since the EFT framework itself is not specific on what kind of physics is responsible for this, it serves as an interface for many BSM theories that can be probed in this way.

We can also introduce new physics by modifying only one or a few interesting parameters and thus changing the Feynman rules of the theory [34]. This approach is referred to as the kappa-framework, but its backend also requires a modeling of the Lagrangian via EFTs [35]. In this thesis, we modify the trilinear coupling of the Higgs by introducing the parameter $\kappa_\lambda = \frac{\lambda_{hhh}}{\lambda_{SM}}$. Since we do not modify the quartic vertex, we set its modifier to the SM value $\kappa_4 = 1$. Equation (2.25) shows the modified scalar potential of $\mathcal{L}_{SM}$.

$$V_{modified}(h) \supset \frac{m_h^2}{2}h^2 + \kappa_\lambda \lambda_{SM} v h^3 + \kappa_4 \frac{\lambda_{SM}}{4} h^4 \tag{2.25}$$

In this thesis we use the implementation of the kappa-framework proposed by Bishara et al. [36].

Different theoretical calculations set a validity range of the kappa-framework. Especially perturbative calculations on single-Higgs production constrain the value of κ_λ if one wants to have reliable higher order corrections. The coupling modifiers value has to be $|\kappa_\lambda| \lesssim 20$ [37],[34] for a full validity of the kappa-framework.

3 Experiment and Simulation

Performing measurements of theory parameters is the only way for us to decide whether we want to accept or reject a theory. In section 3.1 we present the experimental infrastructure at the European Organization for Nuclear Research (CERN) laboratory in Geneva. To understand the data we measure at our experiment, we need to understand the specifics of the theory we want to compare the data to. Therefore, we simulate how we would expect the data to look like according to the Standard Model with the help of Monte Carlo Simulation, which we introduce in section 3.2. A measurement is not worth much, without the interpretation of its results, hence we introduce the statistical tools for data analysis in section 3.3.

3.1 Experimental Setup at CERN

The CERN laboratory is located on the border of France and Switzerland, close to Geneva. It provides facilities for multiple different experiments, that, for example, investigate atoms made of anti-hydrogen [38], try to build nuclear clocks [39] and of course the large high energy collider experiments that led to the discovery of the Higgs boson in 2012 [21].

3.1.1 The Large Hadron Collider

The centerpiece of CERN is the Large Hadron Collider (LHC), which accelerates and collides hadrons. This overview of the LHC is based on [41]. The LHC machine is installed in a 26.7 km long tunnel which was originally constructed for its predecessor, the Large Electron-Positron Collider (LEP). This tunnel lies about 45 m to 170 m below the surface on a slightly inclined plane. The LHC accelerates hadrons, mainly protons but occasionally also heavy ions, to very high velocities close to the speed of light.

Such high speeds cannot be achieved with only the use of one accelerator, but a whole chain of pre-accelerators shown in Figure 3.1. This so-called injection chain consists of the Linac2, Proton Synchrotron Booster (PBS), Proton Synchrotron (PS) and the Super Proton Synchrotron (SPS). After completing this preparation, the protons get injected into the two separate rings of the LHC, where they counter-rotate while they are accelerated further. Typically, 10^{11} protons are grouped together in one bunch, two of which are brought to collision every 25 ns. The LHC holds up to 2808 bunches of protons, which we refer to as beams. The beams are aligned and guided around the rings via superconducting magnets operated at temperatures below 2 K producing magnetic fields with strengths above 8 T. The collisions take place at the four interaction points, where the large experiments are

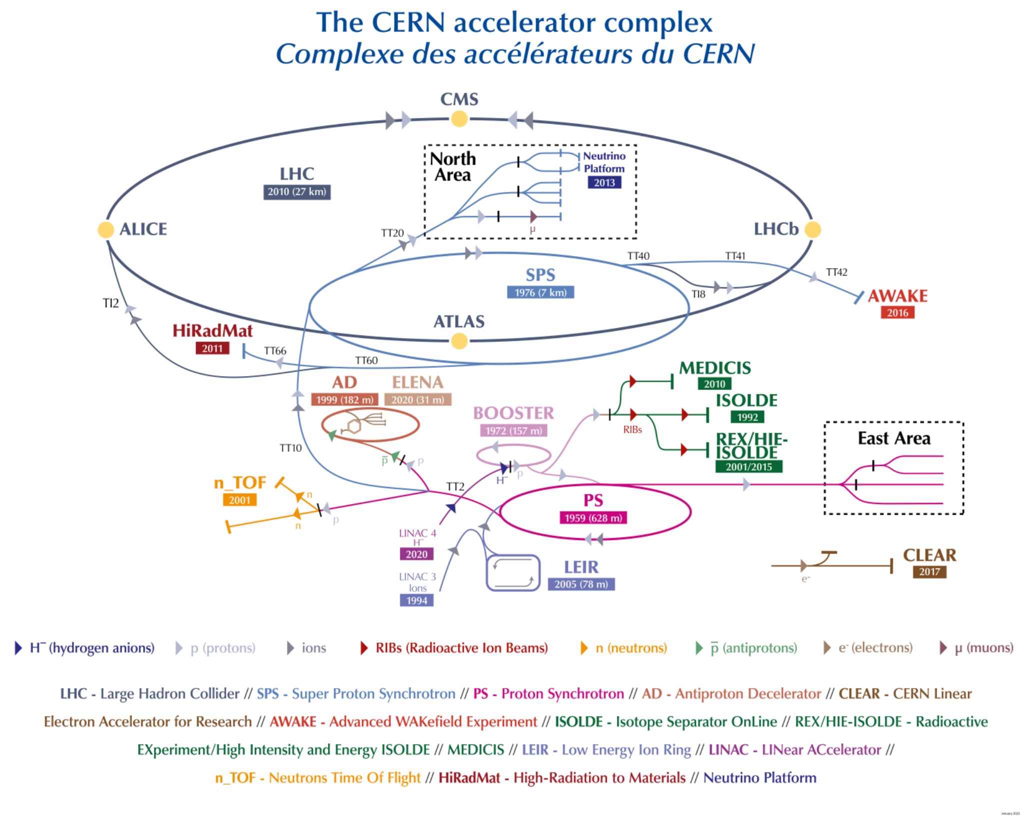

Figure 3.1: Overview of the CERN accelerator and experiment complex [40].

located: the general purpose detectors ATLAS [6] and CMS [42], as well as the ALICE [43] detector and the LHCb [44] detector.

We call the physical interaction process of particles during a collision an event. The probability of one proton-proton collision producing particles X and Y is given by the cross-section $\sigma(XY)$ which is measured in units of *barn*, with $1\,\text{b} = 10^{-24}\,\text{cm}^2$. The expected number of such events per second is given by

$$\dot{N} = L \cdot \sigma \tag{3.1}$$

L is the machine luminosity, a measure for the number of protons that pass through a square centimeter per second, depending on the beam properties. If integrated over the whole time of the measurement, the integrated luminosity serves as a measure of how many events have taken place. The LHC was designed to deliver a luminosity of $L = 10 \times 10^{34}\,\text{cm}^{-2}\,\text{s}^{-1}$ with a center of mass energy $\sqrt{s} = 14\,\text{TeV}$. In the first round of data taking between 2009 and 2013, called Run 1, the peak luminosity delivered by the LHC was $L = 7.7 \times 10^{33}\,\text{cm}^{-2}\,\text{s}^{-1}$ at $\sqrt{s} = 7\,\text{TeV}$ and $\sqrt{s} = 8\,\text{TeV}$ [45].

After a long shutdown with multiple updates of the accelerator and detector infrastructure, the Run 2 data-taking period between 2015 and 2018 delivered a total integrated luminosity of $\mathcal{L} = 139\,\text{fb}^{-1}$ and $\sqrt{s} = 13.0\,\text{TeV}$. In 2023, the Run 3 data-taking period started at $\sqrt{s} = 13.6\,\text{TeV}$. On average, 38 protons of a bunch actually interacted with each other during Run 2. A detector has to deal with all of these collisions at the same time since they result in overlapping detector signals captured at the same time. We call this effect pile-up. Up until 2029, the LHC will be undergoing big updates to equip it for its High-Luminostiy (HL-LHC) era, during which about 10 times as much data as for Run 1+2+3 combined is supposed to be taken, with a targeted integrated luminosity of $\mathcal{L} = 3000\,\text{fb}^{-1}$.

3.1.2 The ATLAS Detector

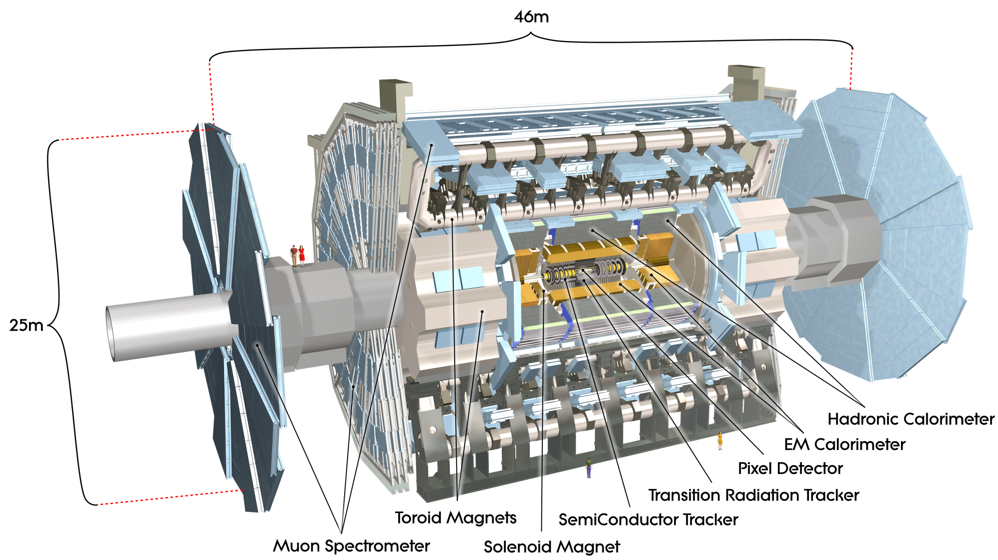

Figure 3.2: "Cut-away view of the ATLAS detector. The dimensions of the detector are 25 m in height and 44 m in length. The overall weight of the detector is approximately 7000 t." [6]

The ATLAS[1] detector, shown in Figure 3.2, is a general purpose detector installed at the LHC. Together with its sister-experiment CMS[2], it takes proton-proton (and heavy ion) collision data at high center of mass energies and high luminosities in order to make precision measurements of SM parameters and to perform searches for beyond SM physics. To be equipped for the challenging data-taking environment at the LHC, the ATLAS detector is designed to cover the region around the beam pipe as tightly as possible. Once the collisions happened, the detector has to quickly process all the signals that particles left in the detector with the help of a trigger system. In general, we call the sum of all particles that get reconstructed for one collision the detector signature of this type of event. This overview summarizes the main features of the ATLAS detector based on its design report [6].

[1] A Toroidal LHC ApparatuS
[2] Compact Muon Solenoid

Coordinate System

The origin of the right-handed coordinate system used within ATLAS is set to the nominal interaction point. The z-axis is defined as the beam direction, the x-axis points to the center of the LHC ring and the positive y-axis points upwards. Accordingly, the x-y plane is transverse to the beam pipe. The azimuthal angle ϕ is measured around the beam axis in the transverse plane while the polar angle θ is measured from the beam axis. We define the pseudorapidity as $\eta = -\ln\tan\left(\frac{\theta}{2}\right)$, which is zero at $\theta = 90°$ and approaches infinity the closer θ gets to the beam axis. Typically, the pseudorapidity η is used instead of the polar angle θ. The distance in pseudorapidity-azimuthal space is then $\Delta R = \sqrt{\Delta\eta^2 + \Delta\phi^2}$.

We refer to the projection of a particle's momentum onto the transverse plane as transverse momentum. The transverse energy is then defined as $E_T = \sqrt{m^2 + p_T^2}$. Before a collision, the two partons of the proton that will interact have approximately no transverse momentum. After the collision, all the transverse momenta of the detected particles thus have to add up to zero according to momentum conservation, which is often not the case. This is what we model for with the missing transverse momentum, generally referred to as missing transverse energy E_T^{miss}, defined as the negative sum of the transverse momenta of all detected particles. It can be used, for example, to account for particles that the detector cannot measure, like neutrinos.

In order to describe the trajectory of charged particles in a magnetic field, we introduce the longitudinal (z_0) and transverse (d_0) impact parameters. The transverse impact parameter d_0 denotes the closest distance of a track in the transverse plane to the point of collision. Similarly, the longitudinal impact parameter z_0 is defined as the value of the z-axis of the point of the aforementioned track that determines d_0.

Tracking System

The detector system closest to the beam pipe is the Inner Detector. Its main tasks are measuring the tracks and thus the momentum and charge of charged particles and enabling the reconstruction of the interaction vertices. It is therefore embedded in a 2 T solenoidal magnetic field. To deal with the large track density after each collision every 25 ns the detector has to have a fine granularity. The innermost layers consist of the insertable B-Layer (IBL) followed by Pixel and silicon microstrip trackers (SCT) which cover a region of $|\eta| < 2.5$. Additionally, there is the Transition Radiation Tracker (TRT) made of gaseous straw tubes covering only a region of up to $|\eta| < 2.0$ but giving complementary information to the silicon-based detector parts. The Inner Detector sub-systems are laid out in concentric cylinders around the beam pipe in the barrel region and arranged on disks in the transverse plane in the end-cap regions. Combined, a track crosses typically 12 layers in the IBL, Pixel and SCT detectors and 36 layers in the TRT.

Calorimeter System

The main task of the Calorimeter System is the precise measurement of the particle's energies. When particles like electrons and photons or hadrons enter these detectors, they

will deposit all of their energy in them through electromagnetic and hadronic showers. The thickness of the calorimeters together with the large coverage of up to $|\eta| < 4.9$ ensures a good measurement of E_T^{miss}.
The electromagnetic calorimeter is the inner calorimeter and consists of lead absorber plates interfaced with accordion-shaped kapton electrodes of Liquid Argon. Its purpose is the precise energy measurement of photons and electrons. The barrel part of this calorimeter covers $|\eta| < 1.475$ and the two calorimeter wheels in the end-cap region cover up to $1.375 < |\eta| < 3.2$. The hadronic calorimeter encloses the electromagnetic calorimeter and is responsible for stopping and thus measuring hadronic particles. It consists of three sampling detector sub-parts. The Tile Calorimeter consists of steel, acting as the absorber, and scintillating tiles taking care of the energy measurement. The LAr hadronic end-cap calorimeter consists of copper plates, while the LAr forward calorimeter consists of copper-based and tungsten-based components, both using liquid argon as the active medium. The sub-parts of the hadronic calorimeter have an overlap to ensure almost full coverage of the interaction point.

Muon System

Muons usually do not get stopped in the Inner Detector as well as the electromagnetic and hadronic calorimeters. Therefore, the outermost layer of the ATLAS detector is specialized in the measurement of muon momentum and energy. The muon detection system is embedded in large superconducting air-core toroid magnets located in the barrel and end-cap regions, allowing again for charge and momentum measurements. The muon tracks are measured in the barrel region with Monitored Drift Tubes (MDTs) arranged around the beam pipe in cylindrical layers. In the end-cap regions, planes of these chambers are arranged perpendicular to the beam axis. In the forward region $2.0 < |\eta| < 2.7$ they are complemented with Cathode Strip Chambers (CSCs). Thus, the muon system covers regions up to $|\eta| < 2.7$. Due to the longer tracks we obtain with the muon measurement, the muon's charge is usually better known than the electrons'. Since usually muons are the only particles to arrive at the muon system, we can identify them with high accuracy.

Forward Detectors

There are three additional detectors placed close to the beam pipe in the forward regions of the ATLAS detector. The LUCID and ALFA detectors are responsible for measurements of the luminosity delivered to ATLAS. The ZDC detector provides information on the centrality of heavy-ion collisions.

Triggers

The data taking at ATLAS is limited by the time it takes the detector components to read out the relevant information before the next collision takes place since the proton-proton interaction rate is 1 GHz while data recording is limited to about 200 Hz. Additionally, not every collision produces physics that is interesting to the current analysis. A two-level-trigger system [46] takes charge of filtering all events and saving only the relevant ones. The Level-1 trigger is hardware-based and makes a first decision on whether to continue data processing based on a subset of the total detector information. The high-level trigger is software-based and further rejects unwanted events. It is composed of the Level-2 trigger and event filter. Overall, the whole data-taking chain results in about 1 MB per recorded event.

3.2 Monte Carlo Simulation

In this section, we first explain the inner workings of a Monte Carlo simulation in collider physics. Afterward, we introduce the technical details of the Monte Carlo software used in this study.

Physics of event generation

The collision of two protons with the resulting final state particles is depicted schematically in Figure 3.3. It is easy to see that this is a complex process with inherently random properties that we model using *Monte Carlo (MC)* methods. The software packages performing simulations using these MC methods are called Monte Carlo *event generators*, whose outputs we refer to as *samples*. The generation of one such sample of a collision consists of multiple steps that we broadly introduce here. For a more thorough introduction, we refer to [47], [48]. At first, the matrix-element of the *hard process*[3] gets calculated at fixed perturbation order. Then, QCD and QED radiation are modeled with *parton shower* algorithms. Finally, hadronization models are applied to obtain the final state particles. Typically, different MC generators are interfaced with each other to perform these simulation steps.

The MC generator extracts the matrix-element from the possible interaction rules. The matrix-element describes the transition between the initial and final state of a process and is thus the part of the cross-section calculation where all the possible interactions of the particles are included. Its integral is then approximated by *Monte Carlo integration methods* [49, p. 170]. This step corresponds to the red blobs in Figure 3.3. At the LHC, not the protons as a whole participate in an interaction, but the quarks it consists of do. We refer to them as *partons*. *Parton distribution functions (PDFs)* are used in MC generators to account for the probability of having a parton of a specific flavor with a specific fraction of the total proton momentum being the one participating in the hard interaction.
In general, the MC generator is able to compute the matrix-element by extracting the interaction rules from different Lagrangians, like the SM Lagrangian or Lagrangians of theories beyond the SM. To provide an accessible implementation that is not specific to one event generator, the *Universal FeynRules Output (UFO)* format was introduced [50]. Using this UFO format, it is easy to study EFT extensions of the SM as introduced in section 2.3.
In the next step, QCD effects on the evolution of the partons from the hard process are described by parton showers. Such effects include initial and final state radiation of the

[3] The hard process is the partonic interaction with the highest invariant mass.

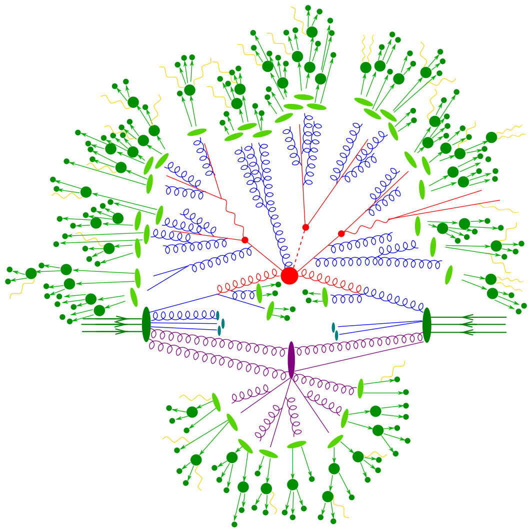

Figure 3.3: Schematic representation of a $pp \rightarrow t\bar{t}h$ event as produced by an event generator. The hard interaction (big red circle in the center) is followed by the decay of the top quarks and the Higgs boson (small red circles). Additional hard QCD radiation is produced (red) and a secondary interaction takes place (purple circle) before the final-state partons hadronize (light green blobs) and hadrons decay (dark green circle). Photon radiation occurs at any stage (yellow). Caption paraphrased and Image taken from [48].

particles through QCD Bremsstrahlung. This step is illustrated with the red curly lines in Figure 3.3.
After the parton shower is completed, hadronization models account for the confinement of these particles into hadrons and their respective decays. Figure 3.3 shows this for the hadronization with the green-colored elements.
Additional interactions of proton remnants "polluting" the hard process are modeled as well, we refer to this step as the simulation of the underlying event, illustrated by the purple lines in Figure 3.3.
Samples produced up until here are referred to as *truth-level*.

For an accurate simulation of the detector, every part of the material in the detector, i.e. every screw and cable, needs to be accounted for. The detector simulation takes over after the truth-level and models the interaction of particles with the detector and the resulting energy deposits (hits) in specific parts. In the digitization step, the output of the detector's readout channels is modeled from these hits. This step also accounts for pile-up. These samples are now at *detector-level*[4].

The complete simulation chain provides us with MC samples at detector-level that mimic real data taken at the ATLAS detector to a very good degree thus letting us compare different theoretical predictions with the actual data. An overview of the ATLAS Simulation Infrastructure from matrix-element generation, parton shower and hadronization models to the complex detector simulation is given in [51].

[4] This is often also referred to as reconstruction-level.

Generators

This work uses *MadGraph5_ aMC@NLO (MadGraph)* [52], a fully automated matrix-element generator, combined with *Pythia 8* [53], responsible for the rest of the simulation chain excluding detector simulation. In ATLAS, detector effects are simulated via the *Geant4* particle simulation toolkit [54],[55].

MadGraph provides a so-called gridpack which is a precompiled version of the event generation process with fixed parameters except for the number of events and random seed, from which the events can then be generated on independent computing nodes. With MadGraphs decay-chain syntax [52, p. 118], final state particles of a production process can be subsequently decayed into specific decay products while taking spin correlations and off-shell effects into account. This is implemented by having a loose on-shell requirement of particle x: $|m_x^* - m_x| \leq \text{bwcutoff} \cdot \Gamma_x$. Here m_x is the particle's mass, Γ_x its width and bwcutoff a user defined parameter, whose default value of bwcutoff = 15 is used in this work.

Pythia provides the option to overwrite the different decay channels, compactly written as a decay table, from the SM, to only allow specific decay modes. For example, a Higgs decaying into two b quarks, thus suppressing the other decay channels. The probabilities of the different decay channels of a particle are called *Branching Ratio* (BR).

These generators can be used standalone or within the *Athena Software Framework* of ATLAS [56, section 3.3]. Athena provides a convenient way to specify the process and parameters for the event simulation in the form of a steering script. This script requires as input a pseudo-python configuration file, called *Job Option (JO)* or jobConfig, the number of events and the random seed for the sampling of the phase space as well as the center of mass energy. Within Athena, a process gets assigned a *dataset identifier (DSID)*, which is a 6-digit code. The JO and possibly gridpack have to be placed in a directory named after the DSID, whose location is then given as input to the script. DSIDs of the range 100000-199999 are reserved for private testing.

In the JO file, we specify the processes to be generated in the specific MC generator syntax. It is possible to also import UFO models, modify the parameters of the particles, like their decay width or mass, and restrict the phase space by applying selections on kinematic variables.

3.3 Basics of Statistical Data Analysis

Consider having any sample of n independent observations of $x = (x_1, ..., x_n)$ on which we want to make meaningful statements regarding the compatibility of this measurement with a given theory. To do so, we need to use the tools of statistical data analysis that we briefly introduce here based on the lecture series by G. Cowan [57].

We want to make a statement on how probable it is that the data we have taken does agree with our theory. To do this, we find a rule assigning a probability to every possible data outcome under the assumption that the theory holds true. We call the theory we test (null) hypothesis. With the help of p-values, we find a critical region of the measurement space in which it would be very improbable to find the observed data while assuming that the hypothesis is true. If we still observe the data in this critical region we reject the hypothesis, i.e. state that the data sample is incompatible with this assumption. For excluding a signal hypothesis, typically a p-value of 0.05 is used which corresponds to a 95% confidence level (CL). In particle physics, the p-value is often converted into a significance Z, defined as the difference between the measured value and mean of the distribution, measured in standard deviations. The 95% CL then corresponds to a significance of $Z = 1.64$.

To deal with multiple hypotheses, we define the likelihood-function $L\left(\vec{\theta}\right)$. It is constructed from the joint probability density functions f for the whole data sample x, where the data points x_i are treated as constant and the free parameters are included in $\vec{\theta}$.

$$L(\vec{\theta}) = \prod_{i=1}^{n} f(x_i; \vec{\theta}) \tag{3.2}$$

When having only one data point, i.e. one bin, of a counting experiment, we can write the likelihood-function with the use of the probability density function of a Poissonian distribution:

$$L(\mu, \theta) = \frac{(\mu s + b)^n}{n!} e^{-(\mu s + b)} \tag{3.3}$$

where s and b are the expected number of signal and background events, respectively and n is the number of observed events. The parameters $\vec{\theta}$ are part of the signal and background estimation. Additionally, we introduce the signal strength μ as an estimation of the ratio of observed signal cross-section to expected signal cross-section, in our case $\mu = \frac{\sigma}{\sigma_{SM}}$. This way, $\mu = 0$ corresponds to the background-only hypothesis and $\mu > 0$ to an additional signal contribution.

To test a different hypothesis we define a test statistic t_μ that separates two hypotheses from each other, which is then used to compute the p-value and subsequently the significance.

$$t_\mu = -2 \ln \left(\frac{L(\mu, \hat{\hat{\theta}})}{L(\hat{\mu}, \hat{\theta})} \right) \tag{3.4}$$

$\hat{\hat{\theta}}$ is the parameter maximizing L in the nominator for the given μ, while $\hat{\mu}$ and $\hat{\theta}$ maximizes L of the denominator for the assumed alternative hypothesis.

We can now calculate the significance Z via the asymptotic formula for likelihood-based tests by [58] as the square root of the test statistic.

$$Z = \sqrt{t_\mu} = \sqrt{-2(n \ln \left(\frac{\mu s + b}{\hat{\mu} s + b} \right) + s(\hat{\mu} - \mu))} \tag{3.5}$$

We can further simplify this expression to [59, p. 82].

$$Z \approx \frac{s}{\sqrt{s + b}} \tag{3.6}$$

We want to set limits on the cross-section of our signal process, therefore we assume the additional signal exists. The null hypothesis tests the case of measuring signal plus background $\mu > 0$, while the alternative hypothesis is that there is background-only, $\hat{\mu} = 0$. In this preliminary study, we don't take any systematic uncertainties into account that could be modeled via $\vec{\theta}$, therefore we omit these parameters from now on. Additionally, since we only take MC samples as entries of our analyzed distributions, the number of observed events n is equal to the expected signal $\mu \cdot s$ plus background. Such samples are referred to as Asimov data. We use equation 3.5 for the statistical analysis of our MC samples, while the expression in equation 3.6 will serve as a quick estimate of the significance when optimizing the specific signal selections.

4 Study of the Signal Process

This chapter focuses on the explicit study of the signal process which we introduced in section 2.2. We perform these first studies that involve testing lots of different settings with a truth-level analysis in order to save computing resources. The Software tools and workflow for this study are presented in section 4.1. We explain the process, called *Event Selection*, by which we filter the interesting events in section 4.2. We motivate the decisions on specific MadGraph and Pythia settings used in the event generation in section 4.3 and present the two UFO models[1] we considered for simulating effects of physics beyond the SM in section 4.4. In section 4.5 we validate the VBS signatures of our signal. Since we are also interested in deviations from the SM regarding κ_λ, we introduce a parametrization of the cross-section via specific κ_λ samples in section 4.6, which enables us to reduce the number of needed MC samples, allowing us to save on computational resources. We conclude this chapter with an overview of the sensitivity of kinematic variables to κ_λ in section 4.7.

4.1 Technical Setup for Truth Level Studies

For VBS ssWWh truth-level studies, we generated MC samples within the ATLAS software framework Athena [56, section 3.3]. During the initial phases, various settings and MC generator versions were explored, which is why the samples used in this chapter are generated with different Athena versions. Samples in

- Section 4.3 are generated with Athena version 23.6.6, providing MadGraph 3.1.1 interfaced with Pythia 8.308 at $\sqrt{s} = 13.6\,\text{TeV}$. Only W^+W^+hjj production is studied.
- Section 4.4 where the H6_UFO model is used are generated with Athena version 22.6.23, providing MadGraph 3.1.1 interfaced with Pythia 8.308 at $\sqrt{s} = 13.6\,\text{TeV}$.
- Section 4.5 and following chapters are generated with Athena version 21.6.105, providing MadGraph 2.9.9 interfaced with Pythia 8.307 at $\sqrt{s} = 13.0\,\text{TeV}$.

The decision to downgrade to an older release was made in order to use the same release as used for the background sample generation of the detector-level analysis in chapter 5. In total 10000 events of VBS ssWWh are produced for each test presented in this chapter. For section 4.5 events of different κ_λ values $\kappa_\lambda \in (-2, 0, 1, 2, 5, 10, 15)$ have been generated. The direct output of the MC generators cannot be used as analysis input, however, a derived format called TRUTH1 is produced with AthDerivation version 24.0.5.

[1]Models of the UFO format using a beyond Standard Model Lagrangian

We perform these truth-level studies with a two-piece analysis setup. First, we produce ntuples[2] via a C++ analysis algorithm that follows [60] and uses AnalysisBase version 22.2.110. The second step also consists of a C++ analysis loop, where we apply process specific selections, introduced in section 4.2. We plot the resulting histograms with ROOT [61]. We provide the code to reproduce this study in [62].

4.2 Event Selection

Table 4.1: Table showing the selection stages used for studying the VBS ssWWh signal.

	Cut	value
Basic selection	$p_T(lep)$	$> 20\,\text{GeV}$
	$p_T(jet)$	$> 20\,\text{GeV}$
	N_{ss_lep}	≥ 2
	N_{jet}	≥ 4
	N_{bjets}	≥ 2
	$N_{vbsjets}$	≥ 2
VBS-like selection	MET	$\geq 30\,\text{GeV}$
	m_{jj}	$> 300\,\text{GeV}$

Although MC samples at truth-level don't account for detector effects, the different kinematic observables already acquired some smearing through the parton shower. Additionally, the MC generators include more diagrams than just the one shown in Figure 2.7. Two such additional diagrams are shown in Figure 4.1. In order to filter events that closely match the VBS ssWWh signature, we perform event selections. These selections are also referred to as cuts.

As a basic selection, we require the leptons and jets to have a transverse momentum larger than 20 GeV. There need to be at least two same-charged leptons and four jets, with two jets having to originate from a b-quark. We label those two jets that do not come from b-quarks and have the highest invariant mass as Vector Boson Scattering (VBS) jets. The lepton with the highest- and second-highest momentum are referred to as leading and subleading lepton, respectively. We apply the same nomenclature to jets. At a second selection stage, we ask additionally for some missing transverse energy $MET > 30\,\text{GeV}$ and the invariant mass of the two VBS-jets to be $m_{jj} > 300\,\text{GeV}$. We refer to this second stage as VBS-like. These selections are shown in Table 4.1. The events are scaled with the sum of MC weights and to a luminosity of $L = 139\,\text{fb}^{-1}$, corresponding to LHC Run-2 data taking.

4.3 $W^{\pm}W^{\pm}hjj$ Production in Event Generators

When extracting the matrix-element for the production of $W^{\pm}W^{\pm}hjj$ and its decays of $W^{\pm} \to l^{\pm}\nu_l$, generally all Feynman diagrams that lead to this final state need to be included to preserve gauge invariance. In other words, the process shown in Figure 2.7 is only a subset

[2] Ntuples are a subclass of ROOT's TTrees, which represent columnar datasets.

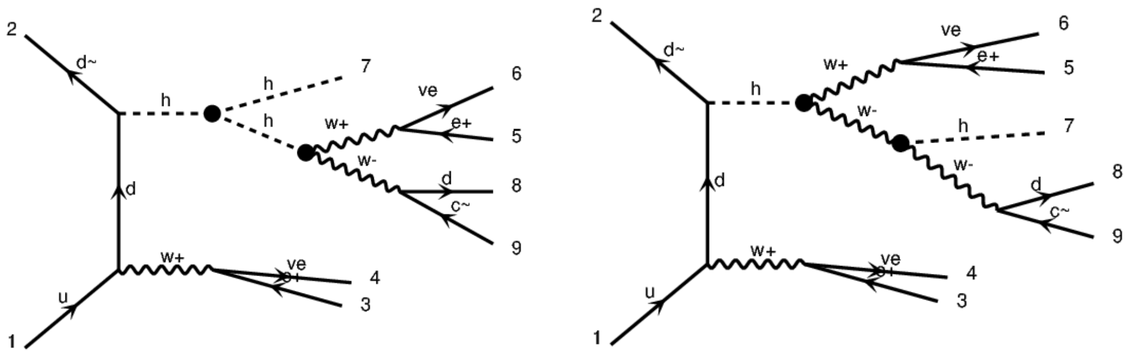

(a) (b)

Figure 4.1: Possible Feynman diagrams of the Di-Higgs (a) and triboson (b) responsible for the non-VBS contaminations of the MC signal sample. The diagrams are taken from the MadGraph output of the VBS ssWWh signal generation.

of all the $W^{\pm}W^{\pm}hjj$ production processes which have to be considered by MadGraph. Many of these processes do not have a VBS-specific signature, see for example Figure 2.7. In total, MadGraph takes 2880 diagrams into account. Nevertheless, we refer to a MC sample of $W^{\pm}W^{\pm}hjj$ production processes, i.e. including all possible Feynman diagrams leading to this final state, as the VBS ssWWh signal process. In the following section, we discuss the important decisions on the design of the JO file, shown in appendix A.2. The samples in this chapter are generated only for $W^{+}W^{+}hjj$, in order to save computing resources while testing.

Four vs Five Flavor Scheme Although the proton consists of up and down quarks bound together by gluons it is possible that at the time of the collision a heavier quark flavor, like the b quark, is produced by a gluon decay and participates as the main parton in the collision. To include this effect in the MC simulations, the parton density function (PDF) of the proton has to include b quarks which then need to be approximately massless [63], which is called the 5 flavor scheme. Massive quarks are then produced during the parton shower. The latest Di-Higgs analyses have switched from the 4 flavor scheme, which uses the proton PDF excluding the b quark, to the 5 flavor scheme [64], while many other SM analyses have been using this scheme for a long time already. For VBS ssWWh, the adoption of the 5 flavor scheme does not seem to make a big difference compared to the adoption of the 4 flavor scheme, as shown in Figure 4.2. For more compatibility with the Di-Higgs analyses, we choose to use the 5 flavor scheme.

Decaying the W Boson With both, MadGraph and Pythia being able to handle the bosonic decays, we test if they produce the same kinematic distributions. In our validation, shown in Figure 4.3, there are slight differences between the two generators handling the W decay. Since there are studies that validated the spin correlations in W boson decays in MadGraph as they are studying angular distributions of the W boson's decay products [65],[66], we choose to decay the W bosons in MadGraph via the decay-chain syntax.

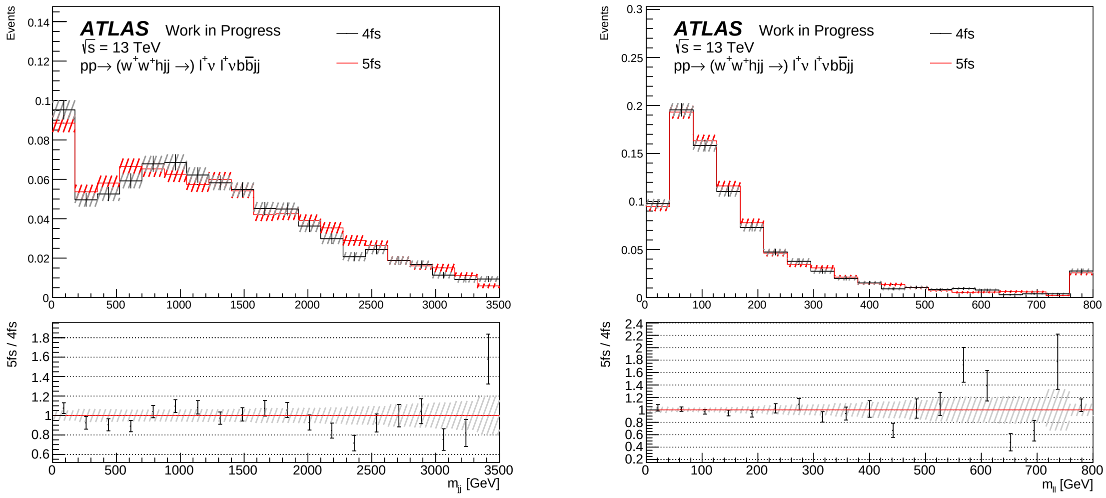

(a) **(b)**

Figure 4.2: Distributions of VBS ssWWh, here exemplarily shown for the VBS di-jet mass (a) and the di-lepton mass (b) showing the difference in choosing the 4 or 5 flavor scheme for the parton density function.

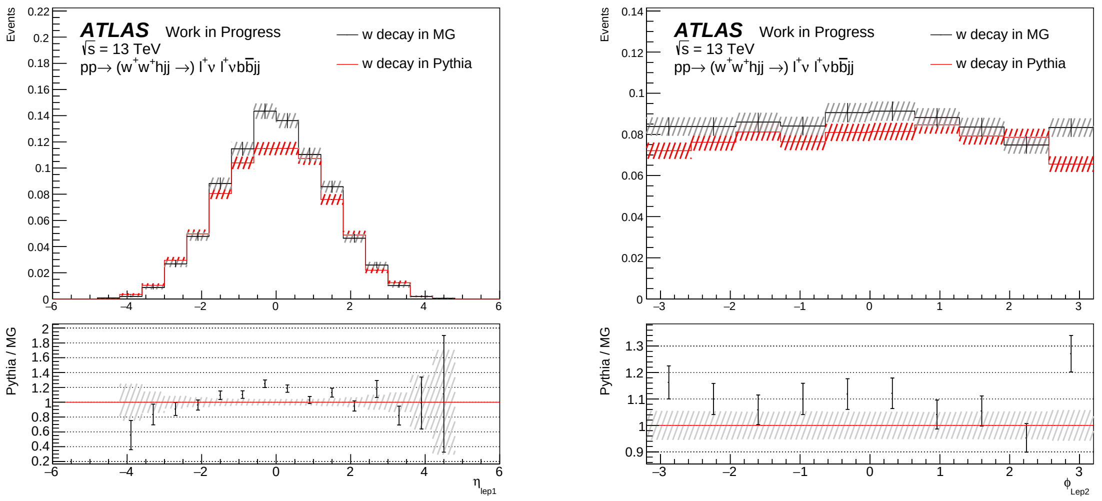

(a) **(b)**

Figure 4.3: Comparison of the effect of letting MadGraph or Pythia handle the decay of the W bosons in the pseudorapidity of the leading lepton (a) and the azimuthal angle of the subleading lepton (b).

Decaying the Higgs Boson Samples where we let the Higgs boson decay in MadGraph show an offset to samples where we let the Higgs Boson decay in Pythia and correct for the Branching Fraction, see Table 4.2.

Table 4.2: Difference in cross-section of VBS ssWWh, depending on whether MadGraph or Pythia handles the decay. In the case where Pythia handles the Higgs boson decay, the resulting cross-section is multiplied with $BR(h \to b\bar{b}) = 58.24\%$.

Processes handled by each MC generator	σ[fb]
MadGraph: $W^+W^+hjj \to W^+ > l^+\nu_l, h > b\bar{b}$ Pythia: -	0.01950 ± 0.00014
MadGraph: $W^+W^+hjj \to W^+ > l^+\nu_l$ Pythia: $h > b\bar{b}$	0.00883 ± 0.00006

In general, we would expect both decay options to produce the same result. MadGraph provides the option to evaluate the Branching Fraction of a decay, given the implemented parameters. We could not retrieve the correct SM Branching Fraction of $BR(h \to b\bar{b}) = 58.24\%$, which explains the difference in cross-section between the Generators. This seems to be expected by the MadGraph authors [67].

One way to manually set the correct Branching Ratio is to modify the Yukawa coupling parameter of the b-quark. The caveat with this treatment is that it changes a physical parameter we are not interested in probing and might also lead to other MadGraph internal interferences with other parameters. Therefore, we decide to not use MadGraph for the Higgs boson decay. Thus, we let MadGraph handle the Higgs boson production and let Pythia handle its decay, by manipulating Pythia's decay tables to only allow decays of the Higgs to $b\bar{b}$. We need to account for this by manually multiplying the resulting cross-section with the $BR(h \to b\bar{b})$.

4.4 Probing Event Generation for Deviations from the SM

The simplest way to modify κ_λ is via the use of beyond SM effective field theories, where their Lagrangians are extracted into UFO models. For this study, we have two models at our disposal.

The theory paper of Henning et al [8] shows very promising results for the competitiveness of VBS ssWWh with current Di-Higgs studies. Since that paper is the motivation for this project, we want to validate their results. The UFO model, so-called H6_UFO, used in [8] is not publicly available but was sent to us upon request. Unfortunately, no instructions for the usage of the model have been included, especially no explanation of the parameters we can modify. The samples in this chapter are generated only for W^+W^+hjj, in order to save computing resources while testing.

This H6_UFO model would have offered the possibility to generate different contributions of the EFT matrix-element separately, which is known as EFT decomposition [33, p. 195]. In short, when computing the square of the matrix-element, we can write this as a quadratic term with only SM operators, a quadratic term with only EFT operators and a linear term with products of SM and EFT operators. In general, we can use this decomposition to study how different (new) operators impact the pure EFT contribution of the process. After reading the source code of the H6_UFO model and applying techniques used in other big UFO models, like SMEFTsim [68], we are still not able to validate this decomposition mode as shown in Figure 4.4. Because of this, we decided to switch to another model, although it would have been more coherent to choose the same UFO model as used in the theory paper.

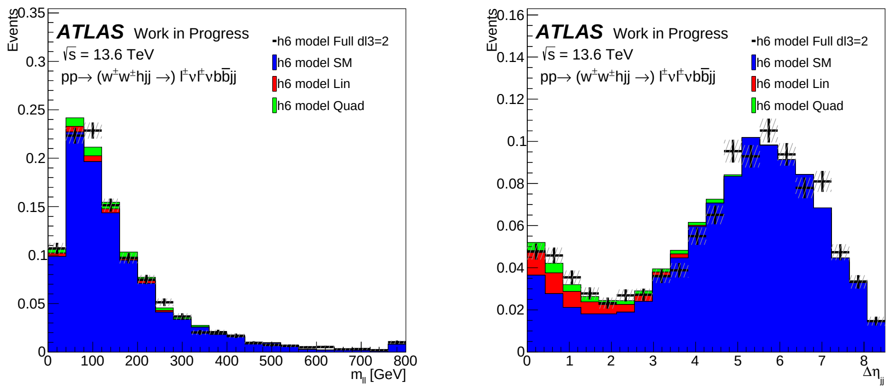

(a) **(b)**

Figure 4.4: Di-Lepton invariant mass (a) and the angular separation in pseudorapidity of the two jets (b). When using EFT decomposition, the quadratic, linear and SM samples should add up to the inclusively generated sample (full). The distributions are shown for $\kappa_\lambda = 2$.

The HHVBF_UFO model [36],[69] has the advantage that it is widely used in Di-Higgs analyses, which makes this project and future studies more comparable, especially in setting and combining limits on κ_λ. The HHVBF_UFO model was specifically designed for Di-Higgs production studies on Higgs (self-)couplings by Bishara et al [36]. The parameter modifying κ_λ is called C3. The model also offers to directly alter the coupling of two vector bosons with two Higgs bosons, κ_{2V} via C2V, and the coupling of two vector bosons to one Higgs boson, κ_V via CV. Feynman diagrams which depend on these parameters are included in the signal generation, one of them depicted in Figure 4.5. As such, studying the whole parameter space of these three coupling modifiers would make sense. However, given the time constraints of this project and the feasibility of a study in a 2- or 3-dimensional parameter space, we focus just on the effects arising from a modified C3 parameter and leave sensitivity studies of VBS ssWWh to κ_{2V} and κ_V for future work.

Since VBS ssWWh has never been studied before with the use of the HHVB_UFO, we first convince ourselves that the model's SM limit, setting $C3 = 1, CV = 1, C2V = 1$, matches MadGraph's internal SM implementation. For the event generation, it is important to note that both models have a different implementation of the Higgs boson's decay width. In the MadGraph internal SM, it is set to its next-to-leading order (NLO)[3] value of $6.382\,339 \times$

[3] Leading order refers to the lowest order of perturbative expansion of the matrix-element, next-to-leading order accordingly to the second to lowest order.

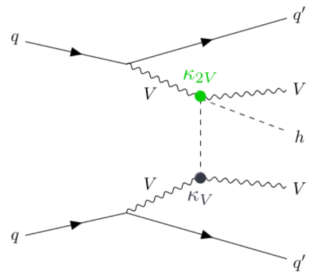

Figure 4.5: Feynman diagram that is part of the signal MC sample showing sensitivity to κ_{2V} and κ_V.

10^{-3} fb, while the HHVBF_UFO model uses the leading order (LO) decay width of 4.0700×10^{-3} fb. Since the HHVBF_UFO model is only capable of LO calculations, we choose to compare its SM limit to the MadGraph internal SM while using the LO Higgs width. Figure 4.6 shows the good agreement between both SM implementations.

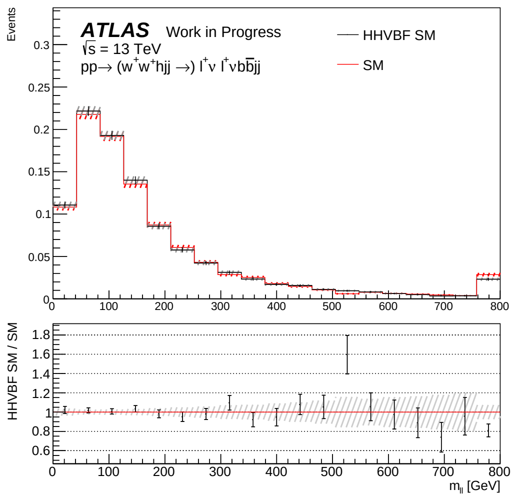

(a)

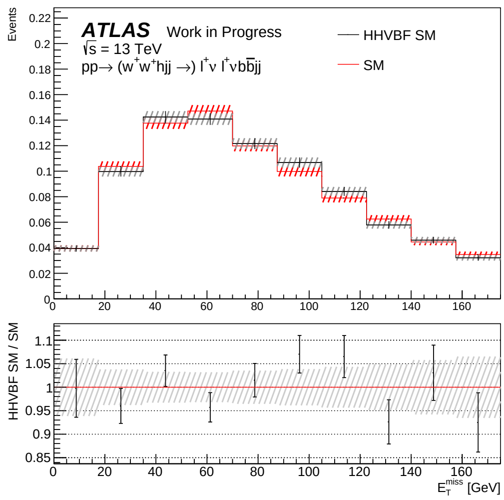

(b)

Figure 4.6: Invariant Di-Lepton mass (a) and E_T^{miss} (b) for a comparison between the SM limit of the HHVBF_UFO model and the MadGraph internal SM implementation.

4.5 Testing the VBS Topology of $W^{\pm}W^{\pm}hjj$ Production

Due to the partons radiating off the W bosons, they don't lose much of their momentum and continue propagating almost in the same direction of motion as before. This is why we expect the angle between the two VBS-jets $\Delta\eta_{jj}$ to be large and the invariant mass of the two VBS-jets to also be rather large. In contrast to this expectation, Figure 4.7(a) shows that the shape of the distribution of $\Delta\eta_{jj}$ changes for small angles when varying κ_λ. Studies at truth level give the option to directly access the partons that come from the hard scatter

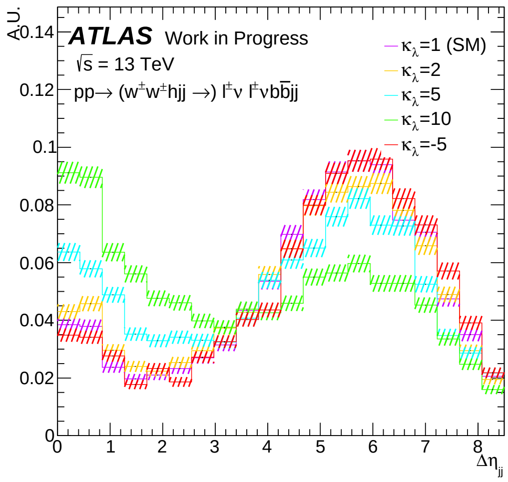

(a)

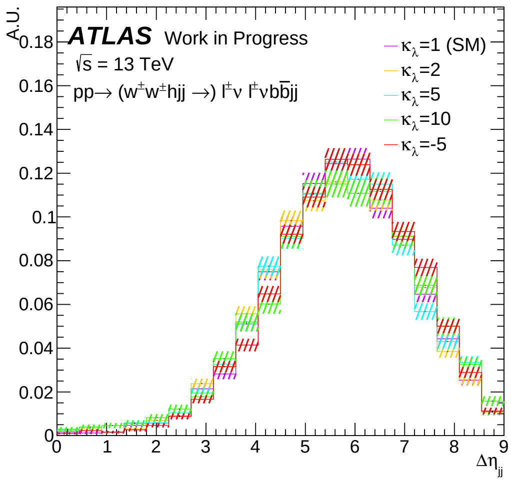

(b)

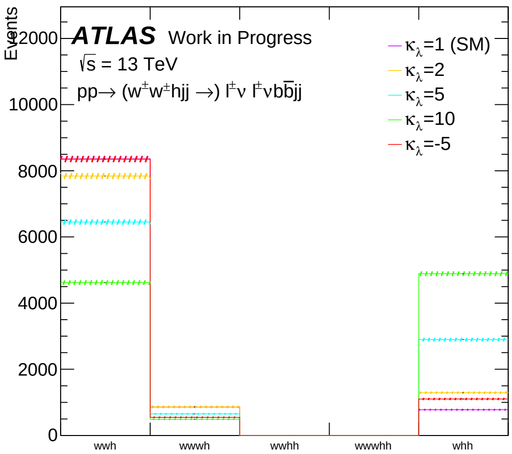

(c)

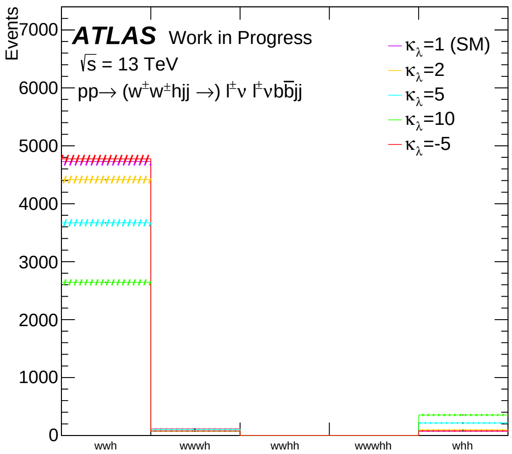

(d)

Figure 4.7: Pseudorapidity separation between the two VBS jets after a basic selection (a) and after VBS-like selection (b) and the number of truth W and Higgs bosons of the hard process after a basic selection (c) and after VBS-like selection (d).

process, to which all the particles from the matrix element get assigned to.[4] When we apply a cut on E_T^{miss} and m_{jj} we see the expected shape of $\Delta\eta_{jj}$ as shown in Figure 4.7(b).

To further study this behavior we label each event with the number of W and Higgs bosons that are part of the hard process in the truth record. We see, that there is a significant contribution of triboson and Di-Higgs processes, the latter increasing for larger κ_λ values, shown in Figure 4.7(c). Feynman diagrams of these processes are depicted in Figure 4.1. When we apply the m_{jj} cut, the triboson contribution decreases vastly. This is because one of the W bosons is responsible for the required production of two jets, whose invariant mass accordingly has a resonance at $m_{jj} \approx 80\,\text{GeV}$. The $m_{jj} > 300\,\text{GeV}$ cut removes this resonance. At NLO the triboson contaminations cannot be removed this easily, as additional jets with large momentum can occur, requiring more evolved studies [71]. As the Di-Higgs contributions are non-VBS-like, they also get removed by the cut. The boson content of the VBS-like phase space region is shown in Figure 4.7(d).

In general, such contaminations are to be expected and need to be accounted for in the analysis. For the $\kappa_\lambda = 10$ signal sample, the signal production is very inefficient, as we lose about 70% of the produced events after the m_{jj} cut.

4.6 Cross-Section Parametrization on κ_λ

For a sensitivity study on a specific parameter like κ_λ it is important to understand how kinematic distributions change with different values of κ_λ. This requires samples of different κ_λ values. Since it takes very long to produce a gridpack, about 30 CPU days, and events from it, about 10 CPUh/10k events, we should be as economical as possible with the computing resources we have. Hence, we should look at other ways to produce distributions of different κ_λ values. Current VBF Di-Higgs studies work with an analytical parametrization derived from the three types of contributing Feynman diagrams to their signal process [72, p. 24ff]. This, however, is not a feasible path for VBS ssWWh due to the complex final state, as MadGraph takes hundreds of diagrams into account when generating the signal sample.

Figure 4.8 shows that in general, the effect of κ_λ on the cross-section is relatively small. We propose to model the dependence of the cross-section of VBS ssWWh on κ_λ via a quadratic function. To enable us to parametrize not only cross-sections but also kinematic distribution with this formula, we express the quadratic formula in terms of three base samples of VBS ssWWh, chosen to be $\kappa_\lambda \in (1, 10, -5)$. We chose these three κ_λ values in a way that includes the SM value in the parametrization and that has a negative and positive κ_λ dependency close to the current limits included as well. Since $\kappa_\lambda = 5, -5$ show very similar shapes, we chose $\kappa_\lambda = 10$ as third sample. Solving the resulting system of linear equations we find

[4] In more recent releases of Athena (R22 and newer) Truth Derivations no longer contain the container with the correct hard scatter particles anymore. Since this is undoubtedly an important tool in analyses with VBS-like signatures, discussions between MadGraph and Pythia authors, the ATLAS Physics Modeling Group and data analysts are ongoing on how to solve this problem. It will be followed up on here: [70]. It is important to keep in mind, that distributions of the parton's kinematics before any shower will not relate 1-on-1 to the actual physics process. Still, they are a good cross-check if properties are qualitatively modeled correctly during different stages of MC event generation.

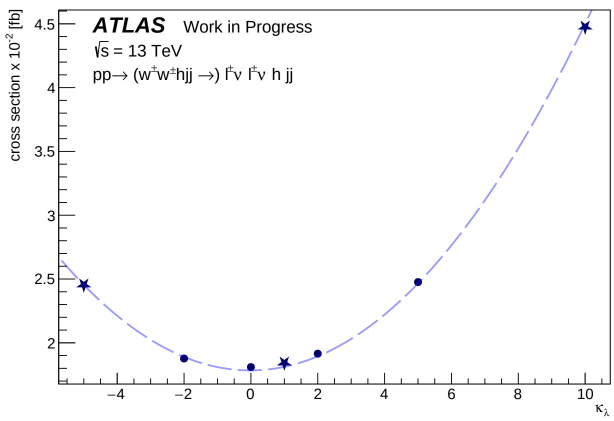

Figure 4.8: Figure showing the dependency of the cross-section on different values of κ_λ and the quadratic parametrization presented in equation 4.1.

the parametrization of the cross-section given in Equation (4.1). Using these parameters we obtain any kinematic distribution by scaling and stacking the histograms of this kinematic distribution of the base samples.

$$\begin{aligned}\sigma(\kappa_\lambda) = &\left(\frac{1}{90}\kappa_\lambda^2 - \frac{33}{270}\kappa_\lambda + \frac{1}{9}\right)\sigma(\kappa_\lambda = -5) \\ &+ \left(\frac{1}{135}\kappa_\lambda^2 + \frac{8}{270}\kappa_\lambda - \frac{1}{27}\right)\sigma(\kappa_\lambda = 10) \\ &+ \left(-\frac{1}{54}\kappa_\lambda^2 + \frac{25}{270}\kappa_\lambda + \frac{250}{270}\right)\sigma(\kappa_\lambda = 1)\end{aligned} \tag{4.1}$$

Figure 4.9 shows a good agreement between the parametrization of an observable and the distribution from the directly generated sample for the invariant di-jet mass for $\kappa_\lambda \in (-2, 0, 2, 5)$. The closure for other observables and κ_λ values is shown in A.5.

4.7 Observables Sensitive to Changes in κ_λ

To make meaningful statements on the sensitivity of VBS ssWWh to κ_λ it is important to find an observable that shows shape differences when varying κ_λ, making it possible to discriminate between the different κ_λ hypotheses.

Studies on polarized[5] boson production through VBS [73] found observables that are sensitive to different polarization states. As discussed in section 2.2, at high energies polarized

[5] Polarization is defined as the projection of a particle's spin onto its momentum; transverse polarization is $\vec{s} \parallel \vec{p}$, longitudinal polarization is $\vec{s} \perp \vec{p}$. After EWSB the W and Z bosons became massive, which means they acquired a longitudinal polarization state. Because of this relation to EWSB, the study of polarized bosons is an important test of the Higgs mechanism.

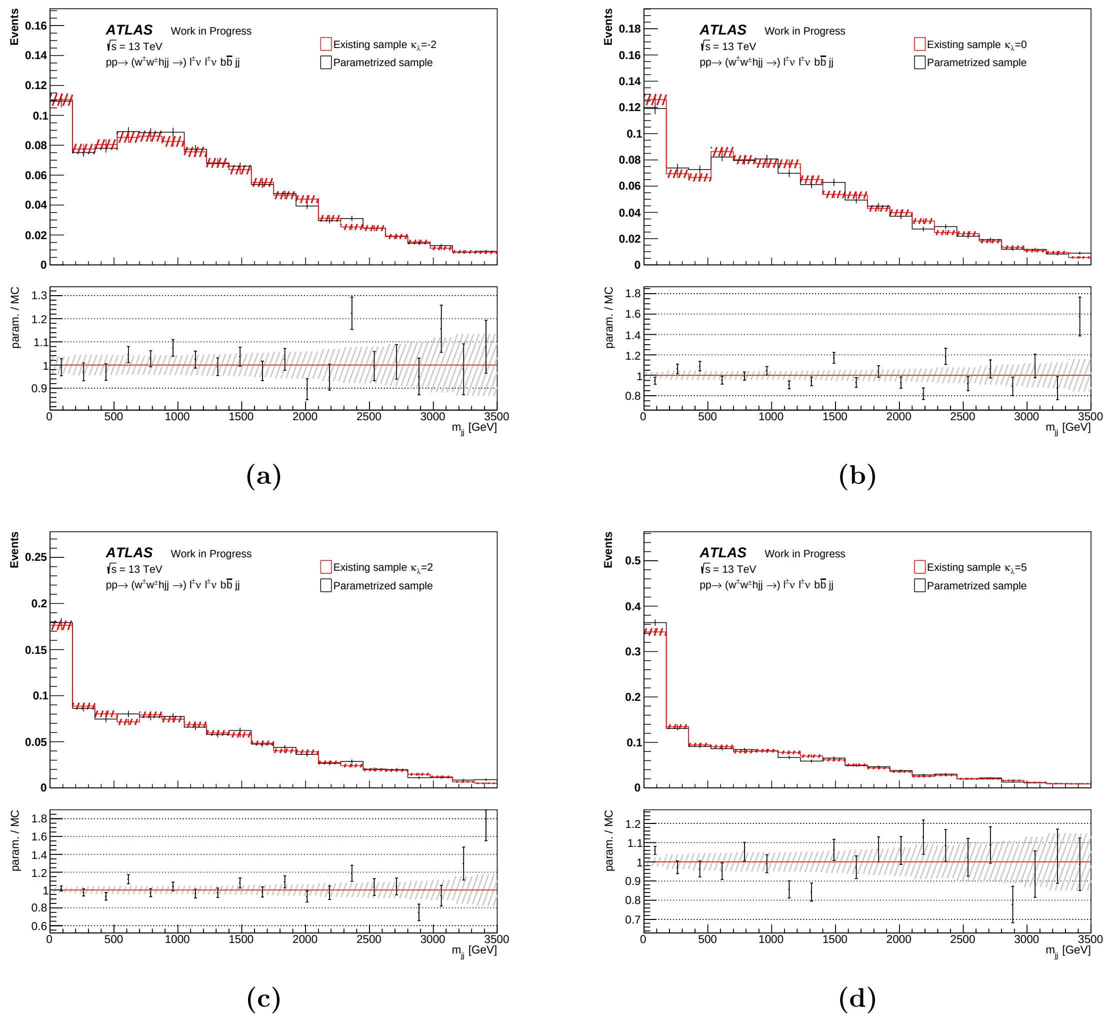

Figure 4.9: Invariant di-jet mass of $\kappa_\lambda = -2$ (a), $\kappa_\lambda = 0$ (b), $\kappa_\lambda = 2$ (c) and $\kappa_\lambda = 5$ (d) in comparison to the respective κ_λ sample obtained with the parametrization shown in equation 4.1.

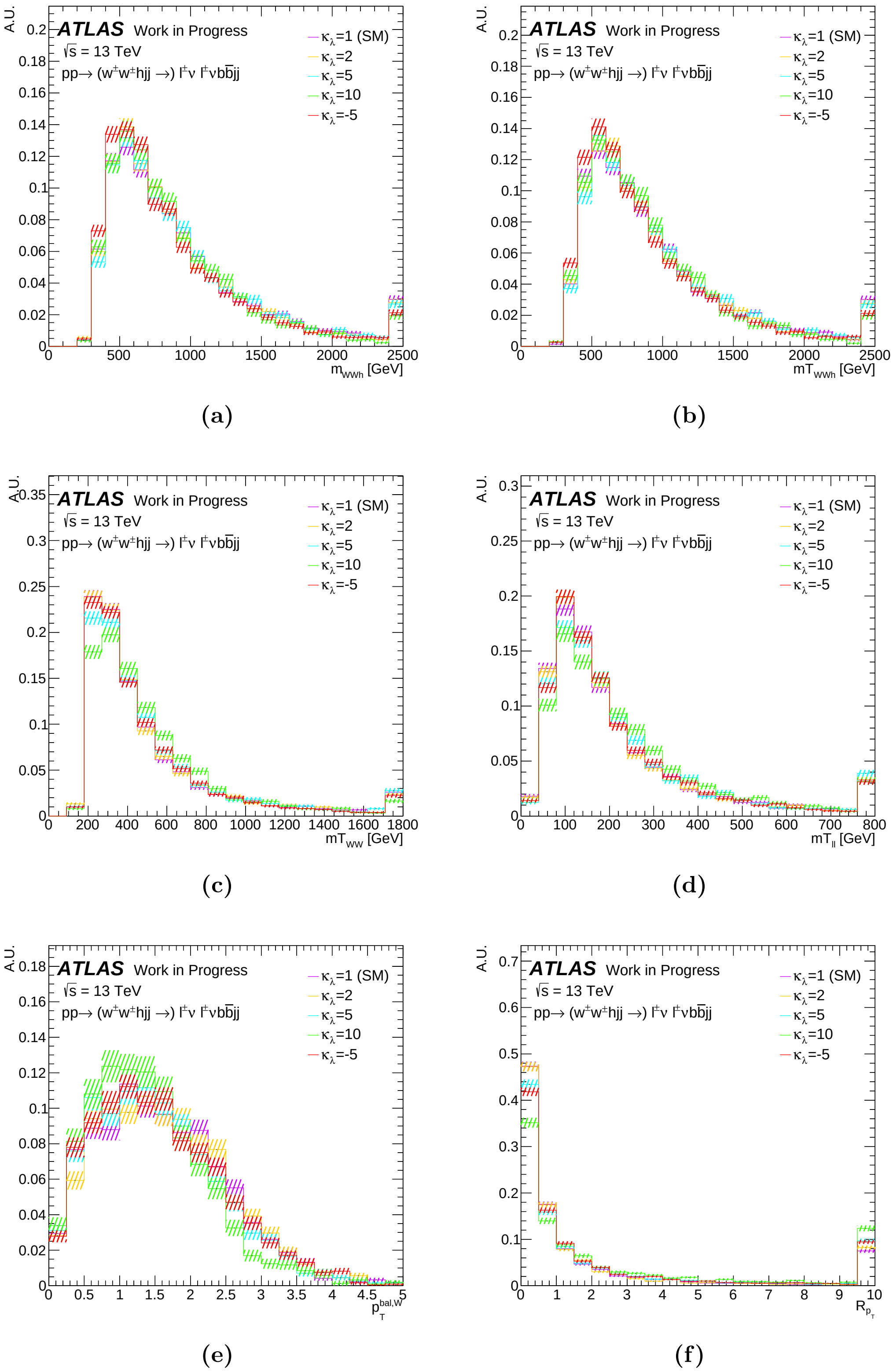

Figure 4.10: Distributions of the invariant mass (a) and transverse mass (b) of the WWh system, the transverse mass of the WW (c) and di-lepton (d) system, the momentum balance of the WW system (e) and R_{p_T} of the two leptons and jets with $\kappa_\lambda \in (-5, 1, 2, 5, 10)$.

bosons behave like Goldstone bosons, which makes these observables also interesting for VBS ssWWh. Therefore, we also test the transverse momentum balance of the two W bosons $p_T^{bal}(W_1, W_2)$ defined in equation 4.2 and the ratio of the transverse momenta of the leptons and jets R_{p_T} defined in equation 4.3 on their sensitivity on varying κ_λ. A particularly strong separation of different polarizations of the W bosons gives the cosine of the angle between the lepton's momentum and the W boson's momentum in the rest frame of the W boson $cos\theta^*$ [74]. However, due to technical difficulties, we were not able to test this observable in this work.

$$p_T^{bal}(W_1, W_2) = \frac{\sqrt{p_{x,W_1} + p_{x,W_2} + p_{y,W_1} + p_{y,W_2}}}{p_{T,W_1} + p_{T,W_2}} \tag{4.2}$$

$$R_{p_T} = \frac{p_T^{l1} \cdot p_T^{l2}}{p_T^{j1} \cdot p_T^{j2}} \tag{4.3}$$

As last observable type we test is the transverse mass of one or multiple particles defined in equation 4.4.

$$m_T(W) = \sqrt{2 \cdot \vec{p_T}(\nu) \cdot \vec{p_T}(\ell)(1 - \cos\Delta\phi(\ell, \nu))} \tag{4.4}$$

$$m_T(WW) = \sqrt{2 \cdot \vec{p_T}(\nu) \cdot \sum_\ell \vec{p_T}(\ell) \left((1 - \cos\Delta\phi(\sum_\ell \vec{p_T}(\ell), \nu)) \right)} \tag{4.5}$$

Figure 4.10 shows the possibly interesting observables. In general, we do not see any striking differences in the distributions when varying κ_λ. The invariant mass of the triboson system and the transverse mass of the two W bosons seem to have a slight ability to differentiate different κ_λ values. This is not as much visible anymore when looking at the transverse mass of the di-lepton system, which means that the influence of the Neutrinos is non-negligible. To make conclusive statements on the transverse mass of the triboson system, R_{p_T} and the momentum balance more statistics is needed. Nevertheless, in the distribution of the momentum balance we suspect some shape differences as well.

To conclude, we did not find a particularly sensitive variable to changes in κ_λ yet. This has to be subject of follow-up studies.

5 Detector Level Analysis

To compare the theoretical predictions on a specific process to data recorded at the ATLAS detector, we also need to include possible background sources, in order to be able to make any meaningful statistical statements. In general, configuring an analysis framework that takes care of triggers, multiple selections, and histogram booking is more tedious than the simple analysis used in the previous section. We take the analysis setup of [29], introduced in section 5.1, as well as their selection on MC backgrounds, presented in section 5.2 as baseline for this work. The definition of physics objects is given in section 5.3, where again, this is mainly influenced by decisions made in [29]. In section 5.4 we describe the phase space regions that we use to study the background modeling, section 5.5. We conclude this detector-level analysis with statistical statements on the production cross-section and sensitivity of VBS ssWWh to $\kappa_\lambda$in section 3.3.

5.1 Analysis Software

The data recorded at the ATLAS detector is a combination of the actual physics processes that occurred with the detector's efficiency and the reconstruction efficiency. In order to compare the reconstructed data of ATLAS directly with the theory predictions these predictions need to include all the detector and reconstruction effects. We use the Geant4 toolkit [54],[55] for the simulation of the detector response of the ATLAS detector. We requested in total 2,320,000 events of MC of different κ_λ values [75] corresponding to ATLAS data taken in Run-2. To account for different detector and data-taking conditions the generation of MC samples is split into three campaigns, mc16a, mc16d and mc16e, corresponding to data taken in 2015-2016, 2017 and 2018 respectively. Table A.1 summarizes the signal MC samples used.

After the detector simulation and reconstruction chain, the resulting output files of type xAOD contain all the events and are thus very large. In order to use them as analysis input we perform two pre-processing steps. At first, a so-called derivation algorithm applies a very loose event selection and saves only a subset of the available information relevant to analyses. The MC samples we use in this work are of the DAOD_SUSY2 format [76], [77], which requires single and multi-lepton triggers to fire. The second step produces light-weight files of the CxAOD format with the CxAOD-Framework [78], by performing the overlap removal as well as a basic pre-selection of the DAOD_SUSY2 files, further elaborated in section 5.3. The technical details on the creation of CxAODs can be found in appendix A.2 of [79].

With the Common Analysis Framework (CAF) [80] of [29] we process the CxAODs, perform the event selection and produce histograms and ntuples. We use the CAF and CxAOD-Framework with AnalysisBase,21.2.222.

5.2 Background MC Samples

Data taken at the ATLAS detector cannot be labeled signal or background events as it is possible for MC samples. For this reason, we have to include all possible processes in the analysis that can end up mimicking the detector signature of the signal we are looking for. If the detector were to be perfect, we would be able to resolve every track and energy deposit with the correct particle hypothesis. Then there would be no background processes arising from misidentified leptons, but only from processes that actually provide two prompt leptons (the exact same signature as VBS ssWWh). We call such background irreducible and backgrounds arising due to misidentified leptons reducible backgrounds.

Table A.2 of the appendix summarizes all included background MC samples and in section A.7 of the appendix, all included samples are listed.

5.2.1 Misidentification of Leptons

Since the detector is not perfect, misidentification of leptons happens: leptons can get assigned to the wrong origin, their charge can get measured incorrectly and objects that are not leptons can leave signatures similar to leptonic ones.

In general, the leptons originating from the hard interaction are called prompt leptons. In the case of VBS ssWWh they would be the decay products of the W bosons. leptons that don't originate from the hard process but for example from hadronic decays are called non-prompt leptons. Due to their different origins, non-prompt leptons and prompt leptons have different kinematic properties, which is vital for their separation during event selection.

When performing the reconstruction of particles from tracks and energy deposits left in the detector ambiguities between different particle hypotheses can arise; objects that are no leptons can get identified as such. Especially jets can leave a signature that can be misinterpreted as the one of a lepton, which we refer to as fake leptons.

In the detector, it can also happen that the charge of a particle is not reconstructed correctly. This can occur for high-momentum electrons since their tracks have almost no detectable curvature [81]. While traversing the detector material, electrons as well as positrons are likely to radiate off photons via Bremsstrahlung. There are two options with which the photon continues propagating: it either passes through the tracking detector without leaving any tracks or it produces a positron-electron pair. In case the photon has a high transverse momentum, there is a possibility that only the produced positron gets detected while the original electron gets lost in the detector due to its by-then low momentum. The same is valid for electrons. Such processes are called charge-conversion or charge-flip processes. Due to their higher mass, muons are less likely to be influenced by Bremsstrahlung and travel until the outermost layer of the detector being influenced by magnetic fields. In this way, we have more space points in the detector measuring the muons track leading to less ambiguity on the charge determination. Studies on Run 1 ATLAS data did not observe any charge-flips of muons [82, p. 38].

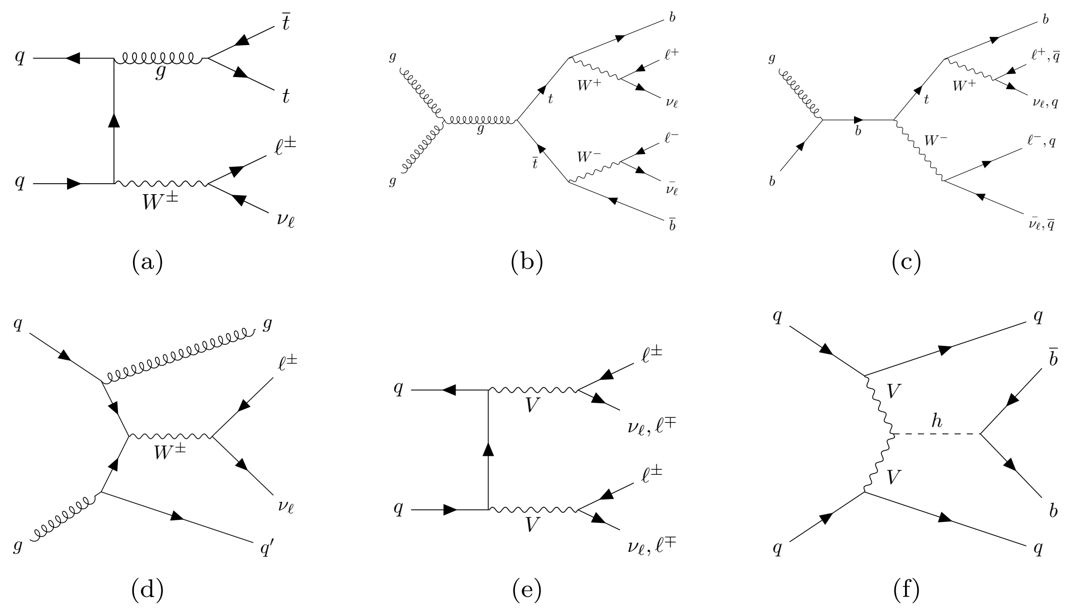

Figure 5.1: Feynman diagrams of the dominant background processes included in this analysis. The irreducible background only consists of $t\bar{t}V$ production (a). The reducible background enters via $t\bar{t}$ production (b), Wt production (c), V+jets(d), diboson production (e) and single Higgs production (f) and $t\bar{t}V$ production, not shown separately. Additional jets are omitted for better visibility.

5.2.2 Reducible Backgrounds

Studies of $W^{\pm}W^{\pm}$ scattering [23, p. 5] showed that non-prompt leptons and charge conversion can make up over 25 % of the overall background. Due to the similar detector signature we assume that this also holds true for VBS ssWWh.

The reducible background included in this work consists of:

- $t\bar{t}$: This process is included at next-to-next-to-leading order with additional jets being simulated. It can mimic the signal via charge-flips of one of the leptons originating from the W bosons or via fake leptons. The required pair of b-jets is already part of the regular structure of $t\bar{t}$. Shown in Figure 5.1 (a).
- **Wt**: This process enters the signal selection if additional jets are included. We can obtain the two leptons when the W bosons decay leptonically, one of those leptons having to undergo a charge conversion. Another possibility is that both W bosons decay hadronically, producing fake leptons and additional jets. Shown in Figure 5.1 (b).

- **V+jets**: The production of vector bosons (V = W or Z) associated with additional jets enters via one prompt lepton and one fake lepton or charge-flip lepton. The b-jets as well as VBS-jets arise through the additional QCD activity and the imperfect b-jet identification. A simple Feynman diagram is shown in Figure 5.1 (c).
- **Diboson (VV)**: Processes, where two bosons are produced are an important electroweak background. Here, the leptonic decays of the Z and $W^{\pm}$ with additional jets are considered. Depending on the actual configuration, the two same-sign leptons are obtained via fakes or charge conversion and one prompt lepton. The scattering of two bosons is not yet included, since the MC samples contain only matrix elements with four electroweak vertices. Shown in Figure 5.1 (d).
- **Single-Higgs**: Single Higgs production via gluon-gluon fusion, vector boson fusion and two top quarks are included as background. For the first two production modes, Higgs decays to $\tau\tau, WW, ZZ$ and bb are considered while for the latter mode, no restriction on the Higgs decay mode is applied. The production of a Higgs boson associated with a vector boson (Higgs-Strahlung) is included as well. As above, depending on the Higgs decay mode one prompt lepton can be part of the signature, while in most of the processes, leptons will enter via fakes and charge-conversion. As an example of a background with purely fake or non-prompt leptons, the vector boson fusion production mode is shown in Figure 5.1 (e).
- $t\bar{t} + V$: As soon as all W bosons decay hadronically, or a Z boson is the produced boson, $t\bar{t} + V$ can only enter the signal selection via fake leptons in the former or charge-flips in the latter case.

5.2.3 Irreducible Backgrounds

The only background with two prompt leptons we expect to have comes from $t\bar{t} + W$ production, shown in Figure 5.1. Here, one of the W bosons stemming from the top-quark decays hadronically, while the other two W bosons decay leptonically. With the b-jets from the top decay and additional jets from QCD radiation, this process has the same detector signature as VBS ssWWh.

5.3 Object Selection

After the simulation of detector effects the physical objects, e.g. leptons or jets, need to be reconstructed from the simulated detector read-out in the MC samples. Since we use the analysis framework of [29], we keep most of the object selections similar to the pre-defined options. We give an overview of the object selection of this analysis, while we leave details on the technical implementations to [29].

First, we need to specify which kinds of detector signatures will be recorded by defining the applied triggers. All events that are of interest to this work have to pass at least one of the triggers shown in Table 5.1. The offline p_T thresholds correspond to the p_T

threshold of the trigger scaled by some factor. For electrons, they are defined in ATLAS to be $p_T^{offline} \geq p_T^{trigger} + 1\,\text{GeV}$ and for muons $p_T^{offline} \geq 1.05 \cdot p_T^{trigger}$.

Table 5.1: List of triggers and offline p_T thresholds used in the CAF and CxAOD-Framework implementation of [29], which was used in this work.

Type	Year	Trigger	p_T^0[GeV]	p_T^1[GeV]
single electron	2015	HLT_e24_lhmedium_L1EM20VH, HLT_e60_lhmedium, HLT_e120_lhloose	25	–
	2016-2018	HLT_e26_lhtight_nod0_ivarloose, HLT_e60_lhmedium_nod0, HLT_e140_lhloose_nod0	27	–
single muon	2015	HLT_mu20_iloose_L1MU15, HLT_ mu50	21	–
	2016-2018	HLT_mu26_ivarmedium, HLT_mu50	28	–
di-electron	2015	HLT_2e12_lhloose_L12EM10VH	13	13
	2016	HLT_2e17_lhvloose_nod0	18	18
	2017	HLT_2e24_lhvloose_nod0 (only for period B5-B8)	25	25
	2017/2018	HLT_2e17_lhvloose_nod0_L12EM15VHI, HLT_2e24_lhvloose_nod0 (not for period 2017 B5-B8)	18	18
di-muon	2015	HLT_mu18_mu8noL1	19	10
	2016-2018	HLT_mu22_mu8noL1	24	10
electron-muon	2015	HLT_e17_lhloose_mu14	18	15
	2016-2018	HLT_e17_lhloose_nod0_mu14	18	15
	2016	HLT_e26_lhmedium_nod0_L1EM22VHI_mu8noL1 ($e\mu$ only)	27	9
	2017-2018	HLT_e26_lhmedium_nod0_mu8noL1 ($e\mu$ only)	27	9
	2015	HLT_e7_lhmedium_mu24 (μe only)	26	9
	2016-2018	HLT_e7_lhmedium_nod0_mu24 (μe only)	26	9

In ATLAS, we reconstruct the physical objects via their tracks and energy deposits in the detector. By clustering tracks close to each other and mapping them to the energy deposits, we can make hypotheses on which particle they belong to. In this process, ambiguities arise, that are taken care of by an Overlap Removal algorithm (OLR). We use the default OLR procedure of ATLAS, further elaborated in [29],[83].

Leptons

Two levels of selection are performed for leptons: the first selection serves as a baseline for the OLR procedure, while the second selection marks the objects used for the event selection. The baseline and signal lepton object definitions are shown in Table 5.2 and Table 5.3 for electrons and muons respectively.

Table 5.2: Electron object selection used in this analysis.

Selection	Baseline Electrons	Signal Electrons
$p_T > 9\,\text{GeV}$	✓	✓
identification working point (ID WP): LooseLH	✓	✓
$1.37 < \eta^{cluster}$ or $1.52 < \eta^{cluster} < 2.47$	✓	✓
$p_T > 25\,\text{GeV}$		✓
identification working point (ID WP): TightTH		✓
isolation working point (ISO WP): Tight_VarRad		✓
$\lvert d_0/\sigma(d_0)\rvert < 5$		✓
$\lvert \Delta z_0 \sin\theta \rvert < 0.5\,\text{mm}$		✓

We implement these selections based on the recommendations of the Electron-Photon-Expert and Muon-Expert group of ATLAS [84],[85]. The baseline selection requires the electron candidates to be within $\lvert\eta^{cluster}\rvert < 2.47$, excluding the transition region from the

Table 5.3: Muon object selection used in this analysis.

Selection	Baseline Muons	Signal Muons
$p_T > 9\,\mathrm{GeV}$	✓	✓
identification working point (ID WP): MediumLH	✓	✓
$\eta^{cluster} < 2.7$	✓	✓
$p_T > 25\,\mathrm{GeV}$		✓
$\lvert\eta\rvert < 2.5$		✓
identification working point (ID WP): MediumLH		✓
isolation working point (ISO WP): Tight_VarRad		✓
$\lvert d_0/\sigma(d_0)\rvert < 5$		✓
$\lvert\Delta z_0 \sin\theta\rvert < 0.5\,\mathrm{mm}$		✓

barrel to end cap region of the detector $1.37 < |\eta^{cluster}| < 1.52$. This is less restrictive for muons, due to the large span of the muon system they are required to be within $|\eta^{cluster}| < 2.7$. Electrons need to pass the LooseLH and Muons the MediumLH identification working point (ID WP) criterion, which corresponds to the probability of a selected track originating from an actual lepton. With a tighter selection, we can reduce the amount of fake leptons while the efficiency in selecting real leptons decreases.

For a lepton to be labeled as a signal lepton, it needs to be within $|\Delta z_0 \sin\theta| < 0.5\,\mathrm{mm}$ of the longitudinal z_0 and within $|d_0/\sigma(d_0)| < 5$ of the transversal d_0 impact parameters. Additionally, we require the leptons to have a transverse momentum of $p_T > 25\mathrm{GeV}$, in order to further reduce misidentification. We want to apply a requirement on the amount of hadronic activity in a cone around the particle's track that we call isolation of the particle. Similar to identification working points, there exist different isolation working points (ISO WP). In section 5.2 we estimated that most of our expected background will be part of our selection due to misidentification of the leptons, so we want to have our lepton selection as tight as possible to reduce these backgrounds. Since [29] saw a decline in signal selection efficiency when using a tighter ID WP and isolation, we study different WPs after a basic selection requiring 2 signal leptons, 2 b-jets, 2 VBS-jets and MET. Table 5.4 shows that choosing the tightest possible ID and ISO WPs[1] does not significantly reduce the signal, but reduces the background by almost a factor of 2 compared to the loosest WP selection studied. Therefore, signal electrons need to pass a Tight ID WP and a Tight ISO WP, while muons need to pass a Medium ID WP and a Tight ISO WP.

Jets

Jets are reconstructed with the anti-kt algorithm with $R = 0.4$ [86] using the pflow jet clustering and requiring a minimum transverse momentum of $p_T > 20\,\mathrm{GeV}$ as well as $|\eta| < 4.5$. In order to reject pile-up jets, selected jets need to pass a tight pile-up suppression requirement [87]. The VBS ssWWh detector signature requires two types of signal jets: jets

[1] In the CxAODs of background MC and data of [29] the Muon ID WP is possible to set to LooseLH and MediumLH, follow up studies will need to check if a TightLH WP for Muons will increase the background rejection.

Table 5.4: Impact of different ID and ISO WP for electrons and muons after a simple selection requiring signal leptons, 2 VBS-jets, 2 b-tagged jets and met. This study was only performed for a subset of $\mathcal{L} = 36\,\text{fb}^{-1}$.

WP Selection				
electron ID	electron ISO	muon ISO	signal yield	bkg yield
TightLH	Tight_VarRad	Tight_VarRad	0.0347 ± 0.0004	640 ± 7
TightLH	Tight_VarRad	Loose_VarRad	0.0363 ± 0.0004	741 ± 8
TightLH	Loose_VarRad	Tight_VarRad	0.0358 ± 0.0004	750 ± 8
TightLH	Loose_VarRad	Loose_VarRad	0.0375 ± 0.0004	855 ± 8
MediumLH	Tight_VarRad	Tight_VarRad	0.0364 ± 0.0004	892 ± 8
MediumLH	Tight_VarRad	Loose_VarRad	0.0381 ± 0.0004	1004 ± 9
MediumLH	Loose_VarRad	Tight_VarRad	0.0379 ± 0.0004	1081 ± 9
MediumLH	Loose_VarRad	Loose_VarRad	0.0396 ± 0.0004	1199 ± 10

that originate from b-quarks (b-tagged jets or b-jets) and the VBS-jets. The b-jets that get b-tagged by a neural-network based algorithm DL1R [88] have to be within $|\eta| < 2.5$. The selected b-jets have to pass the 77% efficiency working point of the flavor-tagging algorithm. In general, VBS jets fulfill $|\eta| > 2.5$. We don't impose any classification on VBS-jets on the object selection level.

Missing Transverse Energy

Missing Transverse Energy (E_T^{miss}) is built using the above introduced physics objects, additionally taking into account tracks and energy deposits not associated to objects.

5.4 Event Selection Optimization

As the purpose of this work is to study the sensitivity of VBS ssWWh to κ_λ, we construct a signal region (SR) tailored towards the specific detector signatures we expect while trying to suppress background events. A baseline selection (base cut) coming from the CxAODs requires already 2 leptons, additionally, candidate events need to pass the trigger requirements presented in section 5.3. The first selection stage picks only those events that have the VBS ssWWh detector signature: 2 same-charged leptons, 2 b-jets, 2 non-b-jets and E_T^{miss}. As mentioned in section 5.3, the signal leptons and jets are supposed to have a minimum $p_T > 25\,\text{GeV}$.

In the CAF, the two non-b-tagged jets with the highest transverse momentum are called VBS-jets. However, for the kinematic distributions, we choose the pair of jets that, respectively, gives the maximum value of invariant mass $max(m_{jj})$ and separation in pseudorapidity $max(\Delta\eta_{jj})$. In order to place a cut on $max(m_{jj})$ and $max(\Delta\eta_{jj})$, we need to make sure that its value does not decrease the overall significance of the signal selection. We model the significance with the approximated formula given in equation 3.6 for the cut optimization.

To compare different cut windows we compute Z for every bin of our histograms and then sum over all bins that lie above the selected threshold 1 and below threshold 2 corresponding to the y-axis and x-axis of Figure 5.2(b),(d) respectively. Figure 5.2(d) shows that for

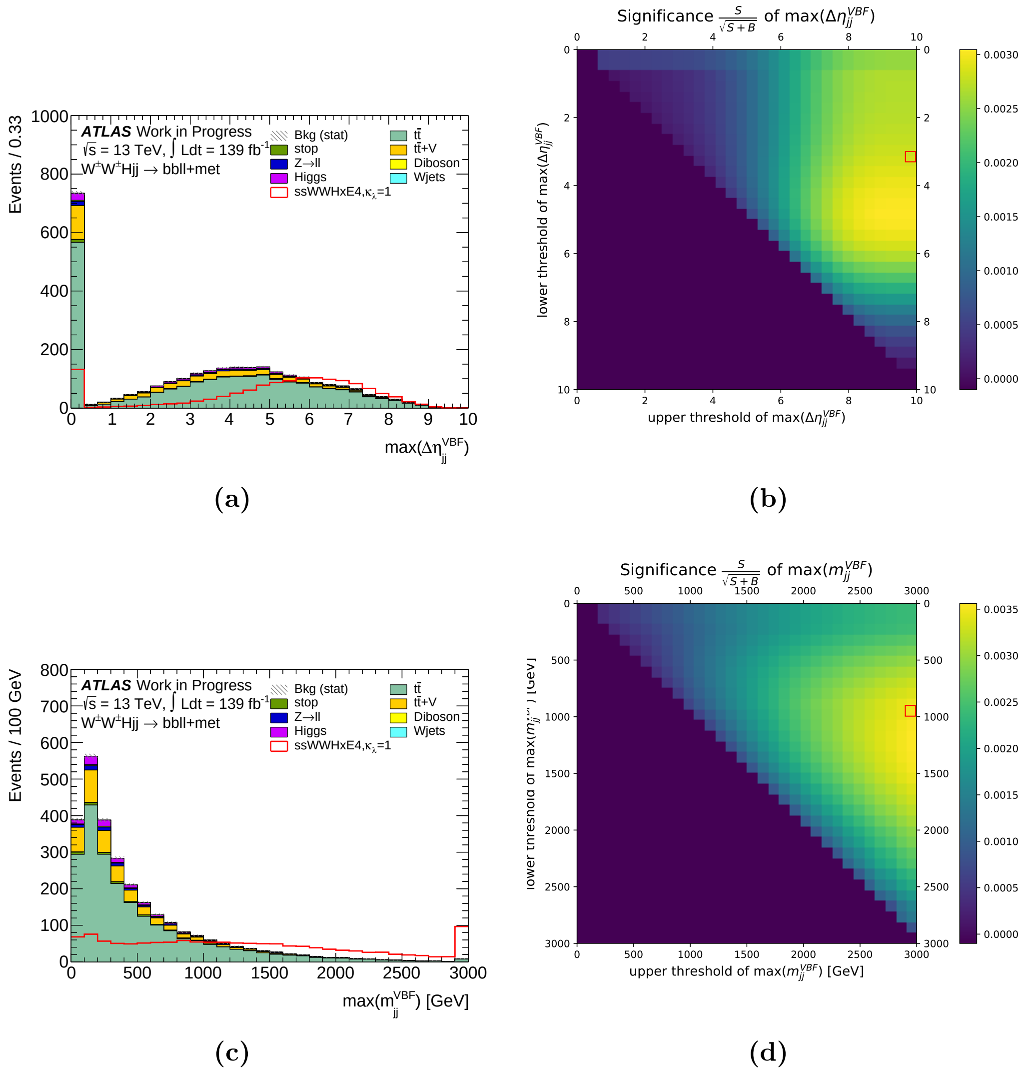

Figure 5.2: Maximum pseudorapidity separation between the two VBS-jets (a) and maximum invariant mass of the two VBS-jets (c). (b) and (d) show the cut-optimization scan with respect to significance for each observable. The chosen cut values are marked with a red rectangle.

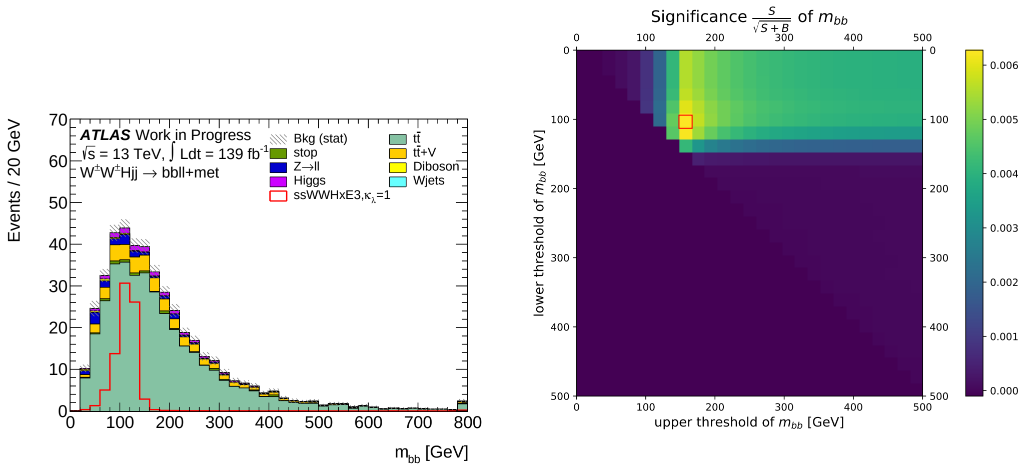

(a) **(b)**

Figure 5.3: Invariant Di-BJet mass (a) with the cut-optimization scan (b) with respect to significance for the distribution shown in (a). The chosen cut values are marked with a red rectangle.

$max(m_{jj})$ the significance is largest when imposing no upper threshold. We gain more significance when increasing the lower threshold until it reaches the high energy region dominated by fewer statistics hence more uncertainties and thus less significance. For $max(\Delta\eta_{jj})$ we see a similar behavior but with a much less rapid change. Since this is just the first study on VBS ssWWh, meaning no extensive studies on background normalization and binning optimization have been performed yet, we don't want to make the selection for this SR too tight. We therefore decide on placing a cut at $max(\Delta\eta_{jj}) > 3$ and $max(m_{jj}) > 900\,\text{GeV}$.

The specific signature of VBS ssWWh requires the production of an on-shell Higgs that can be reconstructed via its decay products: the two, already selected b-jets. Figure 5.3 shows the Di-BJet mass before any cuts and the cut optimization scan for this observable. Although this selection is limited on the resolution of the invariant mass of the two b-jets, the best cut window of $100\,\text{GeV} < m_{bb} < 160\,\text{GeV}$ seems sensible, given the width of the peak.

We perform a last cut on the angular separation of the two b-jets $\Delta R_{b\bar{b}} = \sqrt{\Delta\eta(b\bar{b})^2 + \Delta\Phi(b\bar{b})^2}$ in order to reduce $t\bar{t}$ contributions, which we motivate by the physical processes. While the b-jets in VBS ssWWh originate from the same Higgs Boson, they are boosted into its direction of motion and will have no specific large angular separation. In contrast to this, the gluon propagator of $t\bar{t}$ production shown in Figure 5.1(a) has no transversal momentum which results in the two top-quarks being produced back-to-back in the transverse plane. Therefore, the resulting b-jets will also have a large angular separation, shown in Figure 5.4. When performing the scan on an optimal cut-window, we find that it would be best to include all events below $\Delta R < 1.6$. We decide on placing the cut at $\Delta R < 2$ in order to not have the region too tight yet. The top-quark has some very delicate correlations in its angular variables, which might serve as good discriminators against top-related backgrounds, however, exploiting these constraints for the event selection is beyond the scope

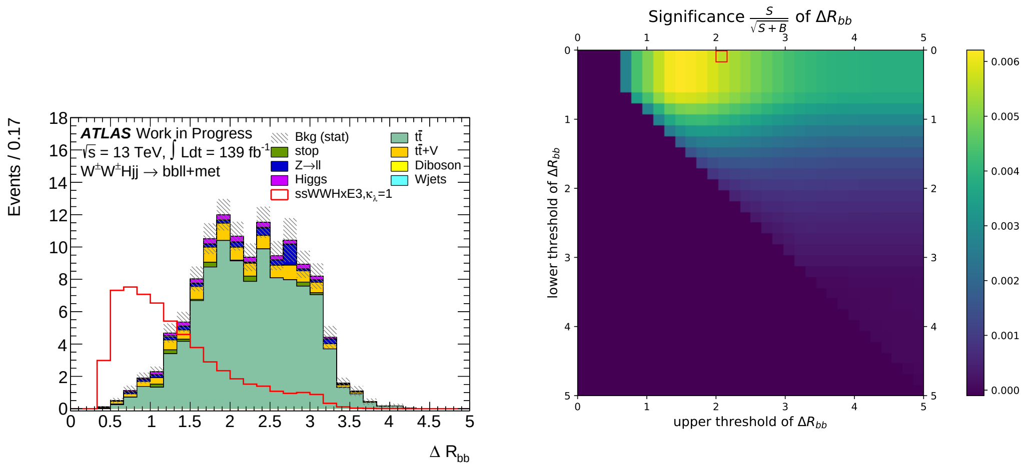

(a) (b)

Figure 5.4: Angular separation of the two b-jets $\Delta R_{b\bar{b}}$ (a) with the cut-optimization scan (b) with respect to significance for the distribution shown in (a). The chosen cut values are marked with a red rectangle.

of this work. Additionally, the Electron Charge ID Selector (ECIDs) [89] is a promising tool, since although it comes with big uncertainties it could remove a lot of $t\bar{t}$ production processes entering the signal region via charge flips and will be studied in future work.

Table 5.5 summarizes the event selection of our signal region. In order to also study the backgrounds more closely, we build a loose control region (CR) and a validation region (VR) orthogonal to the SR, where the signal is suppressed. The loose CR has the same basic selections with respect to transverse momentum and particle content but requires the inverted pseudorapidity cut of the SR $max(\Delta\eta_{jj}) < 3$. For the VR we apply in addition to the basic selection and the VBS cuts a b-mass rejection window around the Higgs mass with $m_{bb} < 60\,\text{GeV}$ or $160\,\text{GeV} < m_{bb}$. For the check on the MC modeling in section 5.5 this means, that all events close to the signal region will be disregarded.

Without any selections, we would expect 1.5 VBS ssWWh events at $139\,\text{fb}^{-1}$. Due to the many non-VBS processes considered in the event generation, our SR selection efficiency of 9% is quite low. Table 5.6 shows the total number of events for the SR, CR and VR. Overall, we can see that the signal contribution is diminishing small. Nevertheless, within the SR we are able to reduce the background-to-signal ratio from 13600000 at base-cut level to 921. The full cutflow, split into single processes is shown in Table A.3 in the appendix. Figure 5.5 shows the contributions of the different background processes to the signal region, control region and validation region. The events are split into channels where the two leading leptons are both muons (mm), both electrons (ee) or muon and electron (em/me). We see that $t\bar{t}$ is the most dominant background, while its amount varies significantly between the different channels. In the mm-channel $t\bar{t}+V$ processes have the largest contribution, while the overall $t\bar{t}+V$ yield stays approximately the same in all channels. In general, the ee-channel yields the most events while the mm-channel has a factor of 4 to 6 less events. This effect occurs mainly because electrons are much more probably to undergo charge-flips and

Table 5.5: Phase space definitions used in this study of VBS ssWWh.

Selection	Signal Region	loose Control Region	Validation Region
$N_{SS-leptons} = 2$	✓	✓	✓
$N_{b-jets} \geq 2$	✓	✓	✓
$N_{VBS-jets} \geq 2$	✓	✓	✓
$MET \geq 30\,\text{GeV}$	✓	✓	✓
$p_T^{Lep} > 25\,\text{GeV}$	✓	✓	✓
$p_T^{Jet} > 25\,\text{GeV}$	✓	✓	✓
$max(\Delta\eta_{jj} > 3)$	✓		✓
$max(m_{jj}) > 900\,\text{GeV}$	✓		✓
$100\,\text{GeV} < m_{bb} < 160\,\text{GeV}$	✓		
$\Delta R_{bb} < 2$	✓		
$max(\Delta\eta_{jj} < 3)$		✓	
$m_{bb} < 60\,\text{GeV}$or $m_{bb} > 160\,\text{GeV}$			✓

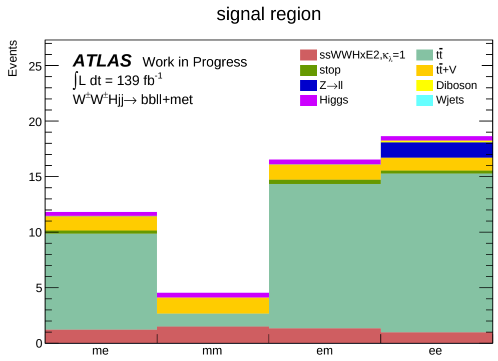

(a)

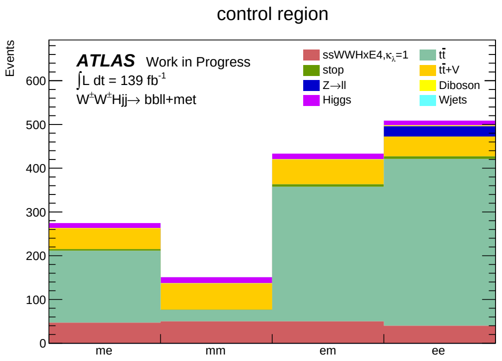

(b)

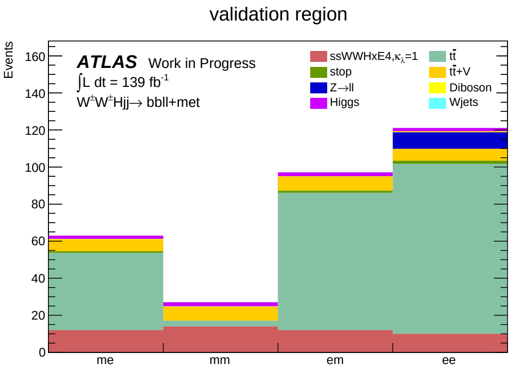

(c)

Figure 5.5: Contributions of different background processes to the signal region (a), control region (b) and validation region (c) split into lepton flavor. These phase space regions are defined in Table 5.5. The signal yield was scaled by a factor of 100 (a) and 10000 (b),(c) in order to make the VBS ssWWh contribution per channel visible.

to get misidentified in general. Since $t\bar{t}$ is part of the reducible background, it only enters the selections via misidentified leptons thus explaining the different yields per channel. The same argument holds true for Z+jets processes. We also considered the impact of W+jets processes as background, but their yield in all phase space regions is negligible. Overall we can conclude, that due to the different background to signal ratios in the mm-, ee-, em- and me-channel a splitting into these channels in the SR might increase the sensitivity of a more elaborate analysis of VBS ssWWh.

Table 5.6: Signal and background yields in different cut stages for the studied Run 2 luminosity and for the HL-LHC projection. Because of the multiple background processes, no initial number of background events based on the cross-sections is given.

Selection	Run 2 ($\mathcal{L} = 139\,\mathrm{fb}^{-1}$)			HL-LHC projection($\mathcal{L} = 3000\,\mathrm{fb}^{-1}$)		
	Signal	Bkg	B/S	Signal	Bkg	B/S
Initial number of events ($\mathcal{L} \times \sigma \times B$)	1.5	-	-	33.0	-	-
$N_{ss-leptons} = 2$, pass trigger requirement	0.5499 ± 0.0015	7470000 ± 5000	13600000	11.87 ± 0.03	161200000 ± 110000	15000000
SR	0.0505 ± 0.0004	46.5 ± 1.9	921	$1.09 \pm 0.01X$	1004 ± 41	921
CR	0.0201 ± 0.0003	1168 ± 9	60000	0.433 ± 0.006	25200 ± 200	60000
VR	0.0049 ± 0.0001	260 ± 5	50000	0.106 ± 0.002	5600 ± 100	50000

We conclude this section with a comparison between the background estimation of Henning et al. [8] and the yields in our signal region. Henning et al. modeled the signal's cross-section and took the background as x-times the signal. The maximum value of background they included was $B = 10 \cdot S$ while we have in our SR a background of about $B = 921 \cdot S$. This means that [8] underestimated the background to signal ratio by a factor of 90. This is partially due to the large backgrounds arising from $t\bar{t}$ and $t\bar{t} + V$ but also due to the relatively low signal selection efficiency. The latter can be explained by the challenges that arose during the signal simulation, with many non-VBS contributing diagrams such as di-higgs and triboson production. We assume, that the contamination of non-VBS diagrams to the signal generation as discussed in section 4.3 was not taken into account by Henning et al.

5.5 Validation of MC Modeling

To avoid any bias[2] on the signal region selection it is customary within ATLAS to blind the data in the signal region(s), i.e. to not look at the actual data while building the analysis. Once all possible tests have been performed to a satisfactory level, analysis teams are allowed to unblind, i.e. look at, the data. Nevertheless, checks to see how good data and MC samples agree with each other need to be performed beforehand. There could be a modeling issue of the MC samples, meaning for example the normalization of a process is not correct or there is a systematic bias in the modelling of the MC samples. We would see the former by finding an (almost) constant factor as ratio of data/background. The latter problem would be a visible trend appearing in the data/background ratio, for example when the left half of the Data/Background ratio is below one and the upper half above one, showing a systematic

[2]Such a bias would be the tuning of the selection to make some statistical excess appear more prominent.

mismodeling in kinematic distributions. The main goal of this section is to get an overview of the MC modeling properties and to make recommendations for future studies.

Data

For the validation in this section, we use the full Run 2 dataset of the ATLAS detector, which was recorded between 2015 and 2018 at a center of mass energy of 13 TeV. Datasets taken under nominal working conditions of the ATLAS detector were used. These datasets are summarized via good runs lists (GRL). The GRLs of the different data-taking periods used in this work are shown in Table 5.7. The integrated luminosity of the Run 2 dataset included in the GRLs is $139\,\mathrm{fb}^{-1}$. The datasets undergo the same pre-processing steps as the MC samples, described in section 5.1.

Table 5.7: The 2015, 2016, 2017, and 2018 good-runs-list (GRLs) used in the analysis. Taken from [29].

Year	Good-Runs-List	$\int \mathcal{L}\, dt [\mathrm{fb}^{-1}]$
2015	data15_13TeV.periodAllYear_DetStatus-v89-pro21-02- Unknown_PHYS_StandardGRL_All_Good_25ns	3.22
2016	data16_13TeV.periodAllYear_DetStatus-v89-pro21-01 DQDefects-00-02-04PHYS_StandardGRL_All_Good_25ns_	33.02
2017	data17_13TeV.periodAllYear_DetStatus-v99-pro22-01 Unknown_PHYS_StandardGRL_All_Good_25ns_Triggerno17e33prim_	44.31
2018	data18_13TeV.periodAllYear_DetStatus-v102-pro22-04 Unknown_PHYS_StandardGRL_All_Good_25ns_Triggerno17e33prim	58.45

Validation of MC Modeling in the Control Region

The control region, defined in Table 5.5, gives us important insights into the general shapes of the data and MC distributions of kinematic variables. Figure 5.6 depicts the invariant di-lepton mass, the pseudorapidity of the leading lepton and the transverse momentum of the leptons for the electron-electron and muon-muon channel. As already discussed in section 5.4, $t\bar{t}$ is dominating the distribution in the ee-channel, while $t\bar{t} + V$ dominates the mm-channel. As $t\bar{t}$ can only enter our selection via misidentified leptons, different misidentification processes seem to dominate in the different channels. Since electrons have a much higher chance to perform a charge flip in the detector, we are able to see lots of events associated with $t\bar{t}$ in the ee channel. Muons however are much less prone to charge-flips, which means that the $t\bar{t}$ contribution in the mm channel has to arise from fake leptons. Since Z+jets processes only enter the ee channel, we assume that these processes also enter predominantly via charge-flips. In the case of single Higgs production, it is not as simple to draw conclusions on the lepton origin as for the other processes. The single Higgs contributions seem to be the same for the ee and mm channels.

Overall, the agreement between data and MC samples is unsurprisingly not good. But since there have not yet been any studies on background normalization and fake leptons, we could have found worse. There does not seem to be a systematic drag of the data/background ratio to one side, but we rather see an almost constant offset in data/background in the ee channel in the distributions in Figure 5.6 and Figure 5.7 of the Di-lepton mass, the pseudorapidity of the leading lepton and the missing transverse energy. The data/background ratio in the mm channel suggests less clear conclusions. In general, the yield of the background processes seems to be underestimated.

In conclusion, after comparing the MC estimated background with data we see that the integrated numbers agree in the order of magnitude. This points to a large underestimation of the background by the theorists. By looking at the different lepton channels, we can see that two main sources of background contribute, charge-flip in channels with electrons and fake muons. The modeling of the MC for each of these backgrounds does not seem to be good enough as we see clear under/over estimations therefore future work should be directed at developing the needed data-driven techniques to estimate these backgrounds more precisely.

Validation of MC Modeling in the Validation Region

The ATLAS VBS VVH analysis started in autumn 2023, so just a few months before this thesis was finished. There is not yet any official blinding strategy proposed. The purpose of the validation of the MC modeling in the VR is to approximate the agreement of the data/background ratio in the SR because the SR is used for statistical statements in the next section. The better the agreement, the more we can trust these statements even though this is just a first explorative study of the sensitivity of VBS ssWWh to κ_λ. We only focus on the invariant di-b-jet mass, to avoid any bias in one of the distributions that might get used for more in-depth background studies.

Figure 5.8 shows the invariant di-b-jet mass, with the blinded area around the Higgs boson's mass. The ratio of data to MC estimated backgrounds follows the same trend observed in the control region, i.e. the sum of the MC background expectation overestimates the total background. By inspecting the data/background ratio a constant offset between the data and simulation can be seen. This constant offset could be corrected by applying a normalization factor of about 0.8 to the MC background. When assuming the same correction factor can be applied to the blinded signal region, we can conclude that our current background estimation is close to what will be obtained from data. This also means that the amount of background is much larger than what was considered by Henning et al. in their preliminary studies.

5.6 Statistical Analysis

Using the optimized signal region with a first data-driven approximation of the background, we perform the statistical analysis of our samples. As explained in section 3.3, we use the asymptotic formula [58] given in equation 3.5 for the significance estimation while varying

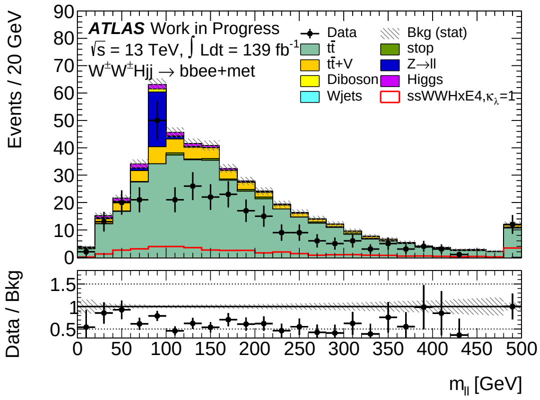

(a)

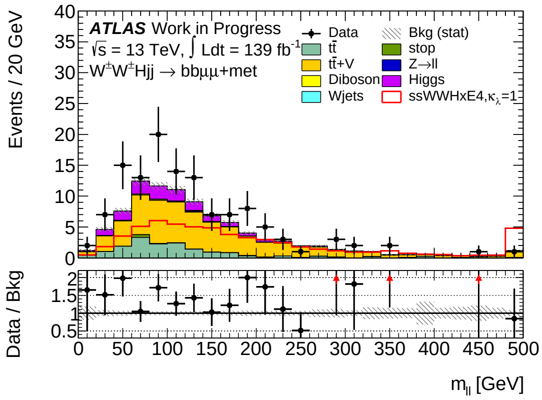

(b)

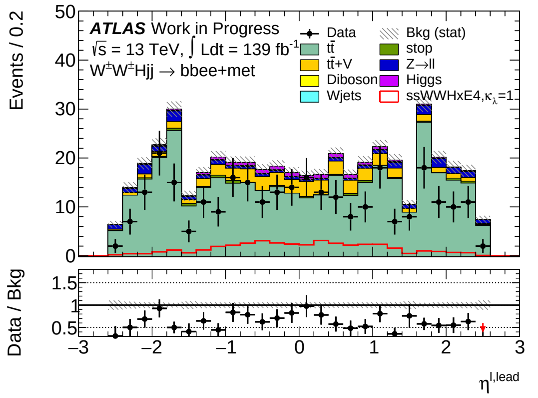

(c)

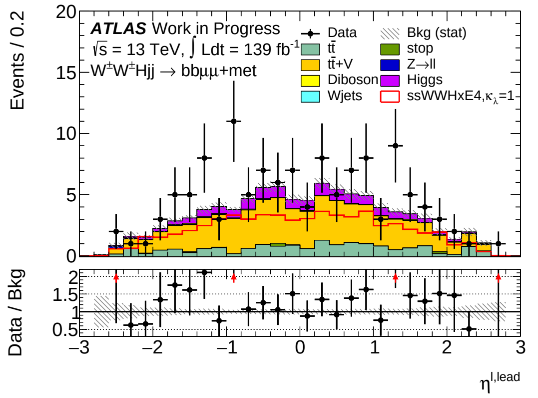

(d)

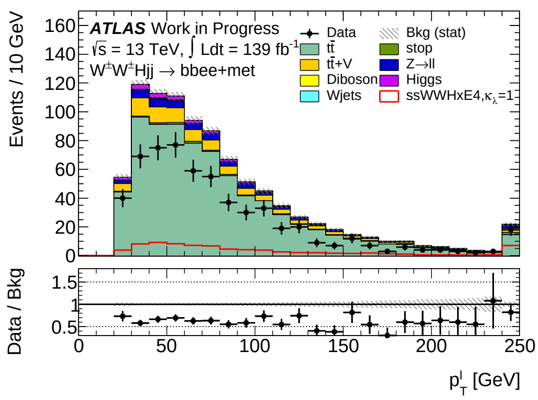

(e)

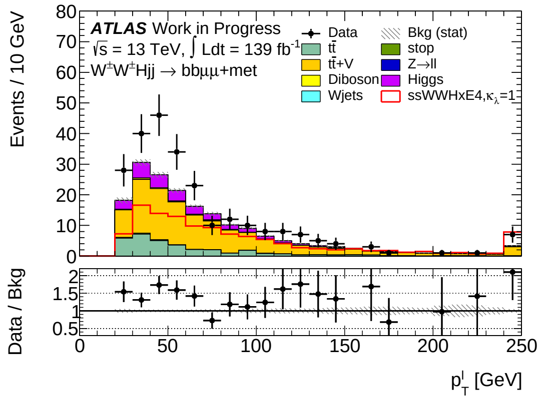

(f)

Figure 5.6: Di-lepton invariant mass for the electron-electron channel (a) and muon-muon channel (b), pseudorapidity of the leading lepton for the electron-electron channel (c) and muon-muon channel (d) and transverse momentum of leptons for the electron-electron channel (e) and muon-muon channel (f). The kinematic distributions are obtained after the control region selection of Table 5.5.

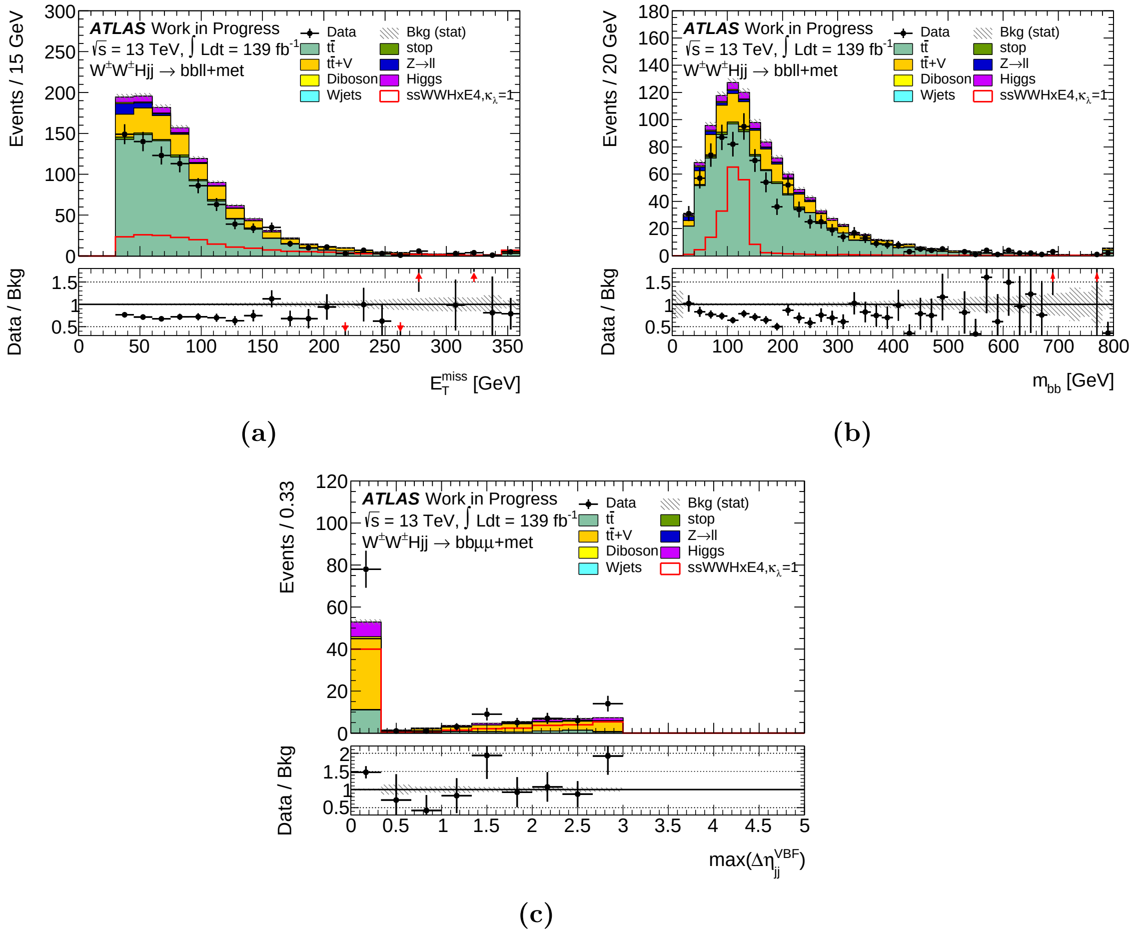

Figure 5.7: Missing transverse energy (a) and invariant di-b-jet mass (b) of all lepton channels and maximum separation in pseudorapidity of the VBS-jets for the muon-muon channel (c). The kinematic distributions are obtained after the control region selection of Table 5.5.

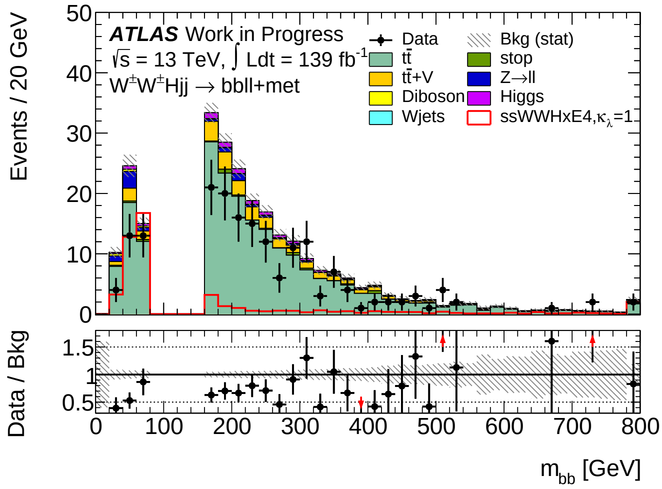

Figure 5.8: Invariant di-b-jet mass obtained after the validation region selection of Table 5.5.

the signal strength μ. We try to find a significance of $Z = 1.64$ which lets us exclude the signal hypothesis for larger values of μ within a 95% confidence level.

The number of expected events is taken from the yield, which is a one-bin histogram. We extract the signal yield to be 0.0505 ± 0.0004 and the background yield to be 46.5 ± 1.9. When applying the normalization factor found in section 4.5, we obtain a data-driven estimate of the background yield of 37.2 ± 1.5.

We find for $Z \geq 1.64$ a signal strength of $\mu_{Run2} \leq 218$. Given the SM prediction of the production cross-section of VBS ssWWh

$$\sigma_{SM}(\text{VBS ssWWh}) = 0.01\,\text{fb}$$

we can expect within our selection to exclude cross-sections of

$$\sigma(\text{VBS ssWWh}) > 218 \cdot \sigma_{SM}(\text{VBS ssWWh})$$

if we were to do a complete analysis of Run-2 ATLAS data.

The theory parameter we want to restrict within this work is κ_λ. In order to set limits on κ_λ we interface the cross-section parametrization on $\sigma(\kappa_\lambda)$ from equation 4.1 with the significance measure, by taking the signal strength dependence on the cross-section to be

$$\mu = \frac{\sigma(\kappa_\lambda)}{\sigma_{SM}(\kappa_\lambda = 1)}$$

In this way we obtain expected limits of κ_λ for $\mathcal{L} = 139\,\text{fb}^{-1}$ and $\mu_{Run2} \leq 218$ with a signal yield of 0.0505 and a background to signal ratio of 737 to be

$$\kappa_{\lambda,Run2} \in [-121, 121]$$

In order to compare these results to the estimate of Henning et al. [8], we scale the signal and background yields to the luminosity of HL-LHC $\mathcal{L} = 3000\,\text{fb}^{-1}$. For a signal of 1.09 events and a $B/S = 737$ at HL-LHC luminosity we find $\mu_{HL-LHC} \leq 44$ and expect to exclude κ_λ outside

$$\kappa_{\lambda,HL-LHC} \in [-54, 54]$$

Additionally, we scan different background to signal ratios, while keeping the signal yield constant. Figure 5.9 shows this scan, with the purple points being the theorists' estimate and the red dots being the limits obtained in this study. We were not able to reproduce the results by Henning et al.; the limits we obtain when sampling with our signal yield at $B/S = 10$ are almost a factor of two larger. As mentioned in section 5.4, this is possibly due to them not accounting for the relatively small signal selection efficiency due to too many contributing Feynman diagrams in the event generation.

This sensitivity study places the expected κ_λ limits above $|\kappa_\lambda| > 20$ for both Run-2 and HL-LHC. According to [37],[34], the validity of the kappa framework is in the region of $|\kappa_\lambda| \lesssim 20$. Moving forward to address the question of the validity of the kappa framework the analysis will need to work on improving the sensitivity to κ_λ and/or looking for an alternative theoretical framework like effective field theories or other BSM models to present

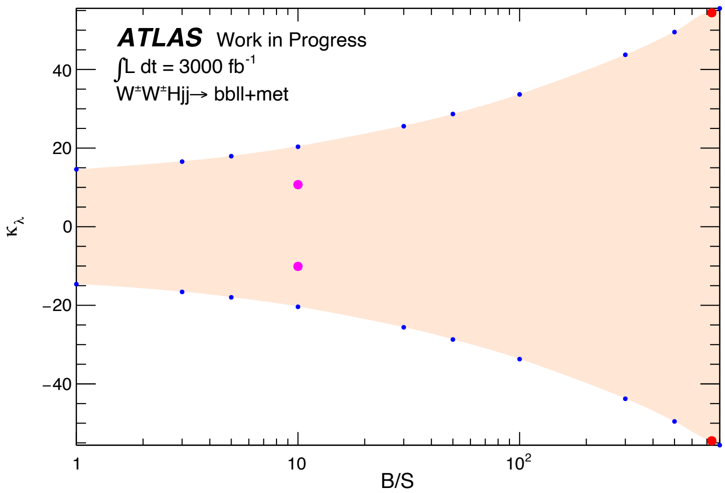

Figure 5.9: The red dots correspond to the expected limits on κ_λ from the VBS ssWWh process at HL-LHC $\mathcal{L} = 3000\,\text{fb}^{-1}$ obtained via the asymptotic formula [58]. The estimate on limits on κ_λ of [8] is shown with the violet dots. In order to compare these two estimates, different B/S values were sampled for a constant signal yield.

the results. Further caveats of this statistical analysis are, that no systematic uncertainties were considered at all, detailed background studies have not been performed yet, and that shape effects of kinematic distributions to changes in κ_λ are not included in the one-bin histogram used for the significance computation. Nevertheless, these results show that the estimate of Henning et al. is not reproducible with simple means. This means, that the current sensitivity of VBS ssWWh on κ_λ in the HL-LHC projection is not competitive to current Di-Higgs analyses, which are constraining κ_λ in $\kappa_{\lambda,Di-HiggsRun2} \in [-1.5, 6.7]$ [30]. With the use of complex analysis strategies involving multivariate algorithms that will be studied in future work the sensitivity of VBS ssWWh to κ_λ will improve vastly, possibly opening up competitive and thus complementary results to current Di-Higgs studies.

6 Conclusion and Outlook

In this work, we studied the sensitivity of Higgs boson production associated with the scattering of two same-charged W bosons (VBS ssWWh) to the Higgs boson's trilinear coupling strength κ_λ. The aim of studying this signature is to provide complementary results to current analyses on Di-Higgs production. We produced and validated Monte Carlo (MC) samples of VBS ssWWh and proposed a parametrization of its cross-section on κ_λ. This parametrization also enabled us to reweight kinematic distributions of three base samples to other values of κ_λ.

During truth studies of the signal process, we noticed the large contamination of non-VBS-like Feynman diagrams, such as Di-Higgs and triboson production, in the VBS ssWWh MC signal sample. These contaminations have to be taken into account when performing the event selection.

The main part of this work was the detector-level analysis of the VBS ssWWh signal. We identified multiple background processes that contribute to our signal selection through misidentified leptons. The most dominant background process is $t\bar{t}$ production, followed by $t\bar{t} + W$ and Z+jets as well as single Higgs production.

In the control and validation regions, built for validating the modeling of the MC backgrounds, we found a constant offset of a factor of 0.8 between data and MC. This indicates that the MC samples overestimate the actual amount of background in these regions. For a first data-driven estimate of the background processes contributing to the signal region, we assumed that the same correction factor could be applied to the signal region as well.

Overall, the work developed during this thesis aimed to have a more precise determination of the background processes in the VBS ssWWh signal region by including detector simulation effects. We compared our event yields to the estimates of [8], and we could conclude that the theory community either underestimated the background or overestimated the signal. After the first data-driven treatments, we see an underestimation of the background by the theorist, as the presence of fake and charge-flip backgrounds is difficult to model. Moreover, in studying the signal at detector level we have identified a sizeable portion of the events that do not originate from VBS ssWWh but rather from VHH and VVVHH signals. These signal contaminations get rejected by the analysis selection, reducing the signal selection efficiency by a large factor. We assume that the theorists did not take this factor into account.

When performing a statistical data analysis, we used a one-bin histogram without including systematic uncertainties to compute significances, in order to obtain expected limits on the production cross-section of VBS ssWWh and κ_λ. In a HL-LHC projection we expect to constrain κ_λ within $\kappa_{\lambda,HL-LHC} \in [-54, 54]$. This result is not competitive with current limits set by Di-Higgs analyses [30] and lies outside the validity region of the employed kappa framework.

In future studies on VBS ssWWh, innovative analysis techniques employing machine learning methods will need to be considered to improve the sensitivity of the Higgs boson's trilinear coupling vastly. Therefore, it is essential to investigate observables sensitive to varying κ_λ. The transverse momentum as well as the momentum balance of the two W bosons hint at such a behavior. Additionally, the polarization of the W bosons might have useful discrimination power motivated by the Goldstone-Equivalence theorem. The VBS ssWWh process seems to be more sensitive to κ_{2V} , the coupling of two vector bosons to two Higgs bosons, which has to be the subject of future studies.

Regarding the event selection, further measures can be included to increase the background suppression. The top quark-related background could be reduced with the use of the ECIDs tool, trained to suppress backgrounds arising from fake and charge-flip leptons. Additionally, the top quark offers many interesting angular properties, that should influence the signal region selection as well. In this study, we did not include the VBS WZh and VBS ZZh processes as backgrounds. However, in analyses on the production of a W boson pair via VBS the VBS WZ process is by far the largest background, which lets us assume that this will be similarly the case for VBS ssWWh.

Although we could not confirm the estimated sensitivity of VBS ssWWh on κ_λ of [8] at detector-level, this work should not be taken as a setback but rather as groundwork for future analyses. In October 2023, an ATLAS analysis team was formed to tackle the analysis challenge of this exciting channel together. In the next decade, the precise measurement of the Higgs boson's trilinear coupling strength modifier κ_λ, whether performed in Di-Higgs production, VBS ssWWh production, or another new channel, will lead to a variety of conclusions on the validity of beyond Standard Model theories. Who knows, in the far future the VBS VVh process might even be used to study the Higgs boson's quartic selfcoupling, then of course via VBS VVhh production.
This is just the beginning.

Appendix

A.1 Mathematical definitions

$$\gamma_0 = \begin{pmatrix} 1 & 0 & 0 & 0 \\ 0 & 1 & 0 & 0 \\ 0 & 0 & -1 & 0 \\ 0 & 0 & 0 & -1 \end{pmatrix} \qquad \gamma_1 = \begin{pmatrix} 0 & 0 & 0 & 1 \\ 0 & 0 & 1 & 0 \\ 0 & -1 & 0 & 0 \\ -1 & 0 & 0 & 0 \end{pmatrix} \tag{A.1}$$

$$\gamma_2 = \begin{pmatrix} 0 & 0 & 0 & -i \\ 0 & 0 & i & 0 \\ 0 & i & 0 & 0 \\ -i & 0 & 0 & 0 \end{pmatrix} \qquad \gamma_3 = \begin{pmatrix} 0 & 0 & 1 & 0 \\ 0 & 0 & 0 & -1 \\ -1 & 0 & 0 & 0 \\ 0 & 1 & 0 & 0 \end{pmatrix} \tag{A.2}$$

$$\gamma_5 = \begin{pmatrix} 0 & 0 & 1 & 0 \\ 0 & 0 & 0 & 1 \\ 1 & 0 & 0 & 0 \\ 0 & 1 & 0 & 0 \end{pmatrix} \tag{A.3}$$

A.2 Monte Carlo Generation Configuration File

For this work the HHVBF_UFO model [36],[69] is used. The parameter modifying κ_λ is called C3. The model also offers to directly alter the coupling of two vector bosons with two Higgs Bosons, κ_{2V} via C2V, and the coupling of two vector bosons to one Higgs Boson, κ_V via CV. Athena provides a python steering script for the event simulation.

```
Gen_tf.py --ecmEnergy=13000. --maxEvents=-1 --randomSeed=1005 --
    outputEVNTFile=EVNT.root --jobConfig=100002
```

Setting the number of events to -1 lets the script fall back to the number specified in the JO. When generating a gridpack, one should add the flag `--outputFileValidation=False` since there will be no valid EVNT file produced.

The JO (configuration file) of the official production request as well as some guidelines on how to use MadGraph in Athena can be found in [90] with the relevant parts shown below. A specific setting we want to point that out that is used in this JO is Pythias "SpaceShower: dipoleRecoil" option. This is specifically introduced to better model the scattering process of vector bosons [53].

```
# MadGraph
import string
from MadGraphControl.MadGraphUtils import *
import MadGraphControl.MadGraph_NNPDF30NLO_Base_Fragment
MadGraphControl.MadGraphUtils.MADGRAPH_PDFSETTING["alternative_dynamic_scales"] = [1,2,3,4]
# Define physics process to be simulated
mgproc = '
import model HHVBF_UFO-5FSwithYukawa
define p = g u c d s u~ c~ d~ s~ b b~
define j = g u c d s u~ c~ d~ s~ b b~
define l+ = e+ mu+
define l- = e- mu-
define vl = ve vm
define vl~ = ve~ vm~
generate p p > w+ w+ h j j QCD=0, w+ > l+ vl QCD=0  @0
add process p p > w- w- h j j QCD=0, w- > l- vl~ QCD=0 @0
'
# Setting parameters for param_card.dat; CX=1 are the SM parameters
parameters = {}
parameters['NEW'] = {'CV':  '1.0000000',  # CV
                     'C2V': '1.0000000',  # C2V
                     'C3':  int(physShort[physShort.find("_kl")+3:].translate(string.maketrans('pm','+-')))}  # C3, a.k.a kl
parameters['MASS']={'25':'1.250000e+02'} #MH
# Setting some parameters for run_card.dat
extras = { 'lhe_version':'3.0',
            'ptl': 4.0,
            'ptj': 10.0,
            'drll': 0.2,
            'drjl': 0.2,
            'drjj': 0.4,
            'etaj': 5.5,
            'etal': 4.0,
            'auto_ptj_mjj':False,
            'cut_decays': True,
            'systematics_program': 'systematics',
         }
# Pythia8 showering
include("Pythia8_i/Pythia8_A14_NNPDF23LO_EvtGen_Common.py")
include("Pythia8_i/Pythia8_MadGraph.py")
include("Pythia8_i/Pythia8_ShowerWeights.py")
genSeq.Pythia8.Commands += ["25:onMode = off",
                            "25:oneChannel = 1 1 100 5 -5 "]  # bb decay
# Dipole option
genSeq.Pythia8.Commands += [ "SpaceShower:dipoleRecoil = on" ]
```

A.3 Comparison of 4 and 5 Flavor Scheme

In the following further kinematic distributions are shown for the comparison between the 4 flavor scheme and 5 flavor scheme. Overall, there is no difference to be seen between the two schemes.

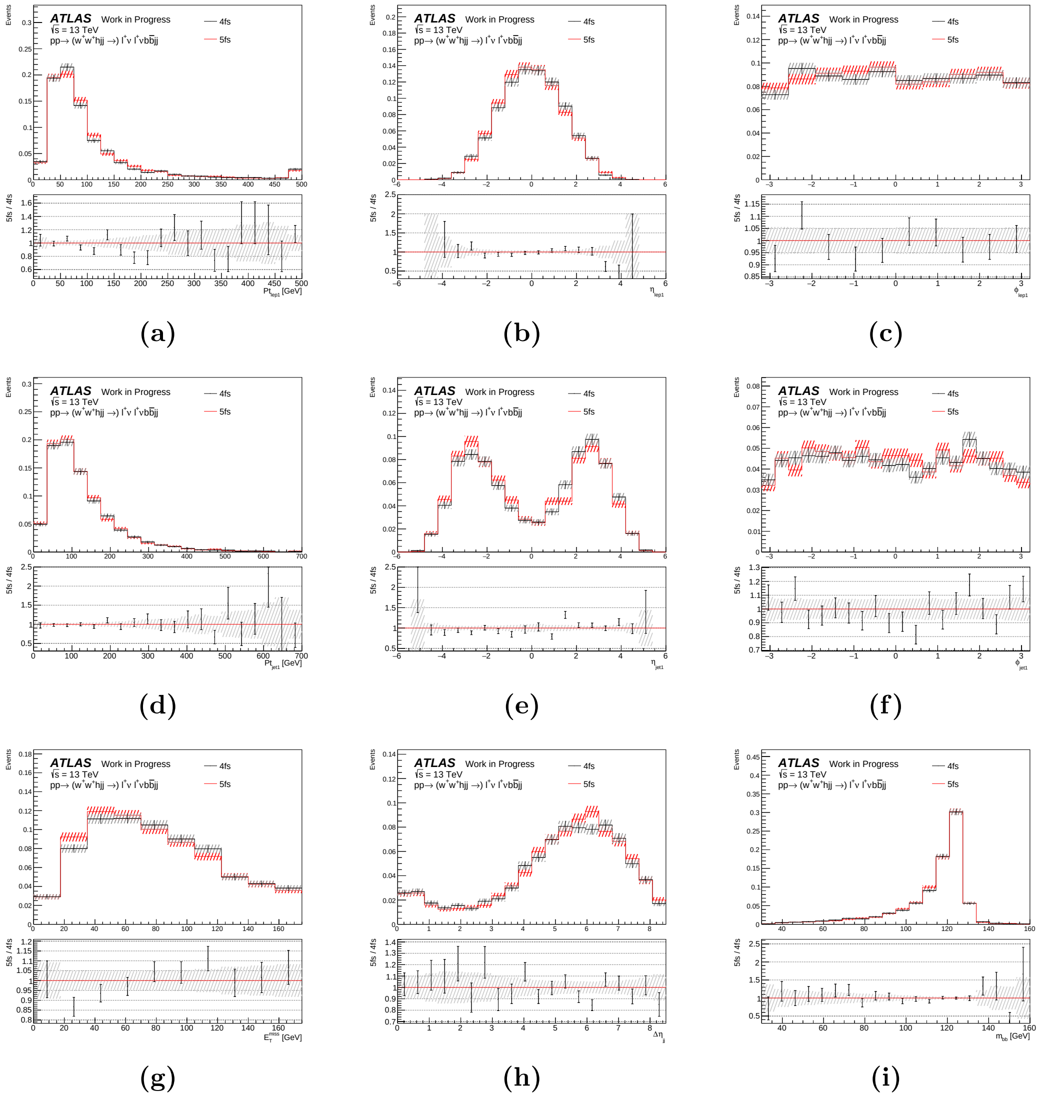

Figure A.1: Comparison between the 4 flavor scheme and 5 flavor scheme. The Figure displays the transverse momentum (a), pseudorapidity (b) and azimuthal angle (c) of the leading lepton, transverse momentum (d), pseudorapidity (e) and azimuthal angle (f) of the leading jet and the missing transverse energy (g), the pseudorapidity difference between the two VBS-jets (h) and the invariant mass of the two b-jets.

A.4 Comparison of Internal SM and SM Limit of HHVBF_UFO

In the following further kinematic distributions are shown for the comparison between the SM limit of the HHVBF_UFO model and the MadGraph internal SM implementation. Overall, there is a good agreement between both models.

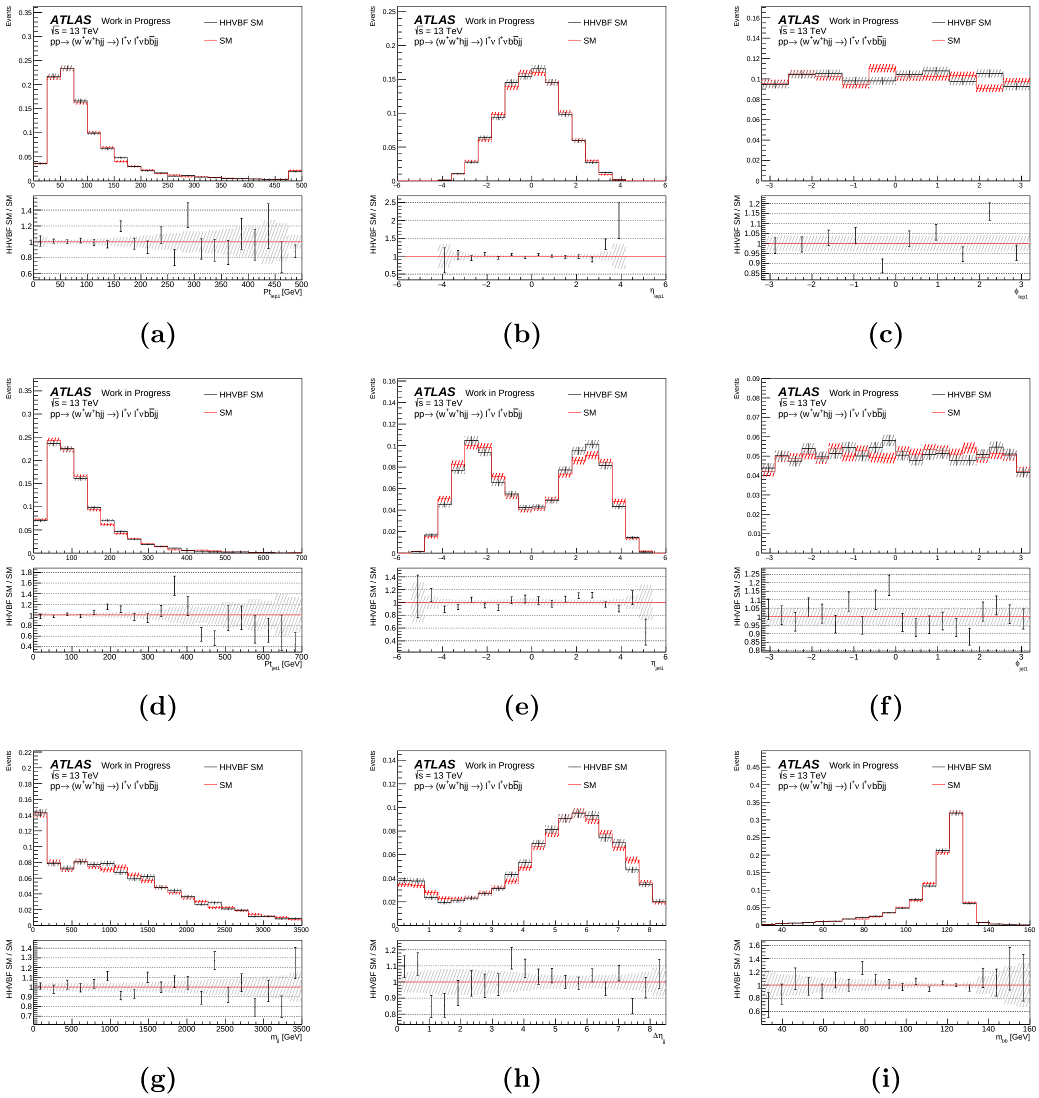

Figure A.2: Comparison between the SM limit of the HHVBF_UFO model and the MadGraph internal SM implementation. The Figure displays the transverse momentum (a), pseudorapidity (b) and azimuthal angle (c) of the leading lepton, transverse momentum (d), pseudorapidity (e) and azimuthal angle (f) of the leading jet and the invariant mass of the two VBS-jets (g), the pseudorapidity difference between the two VBS-jets (h) and the invariant mass of the two b-jets.

A.5 Validation of Cross-Section Parametrization on κ_λ

We show further validation plots of the proposed parametrization shown in equation 4.1 of $\kappa_\lambda \in (0, 2, 5, -2, 15)$. The basic selection is applied.

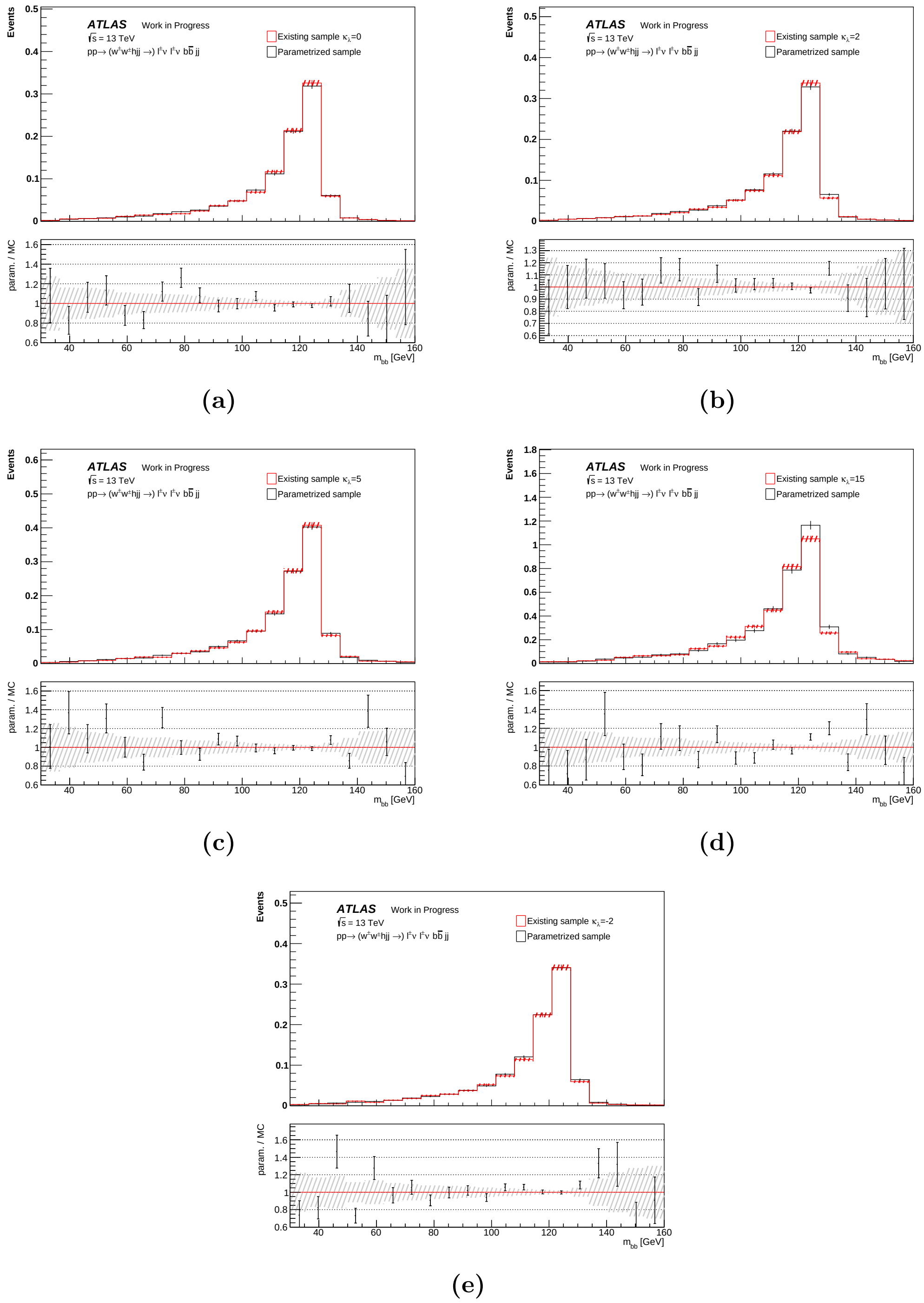

Figure A.3: Invariant mass of the di-b-jets of $\kappa_\lambda = 0$ (a), $\kappa_\lambda = 2$ (b), $\kappa_\lambda = 5$ (c), $\kappa_\lambda = 15$ (d) and $\kappa_\lambda = -2$ (e) in comparison to the respective κ_λ sample obtained with the parametrization shown in equation 4.1.

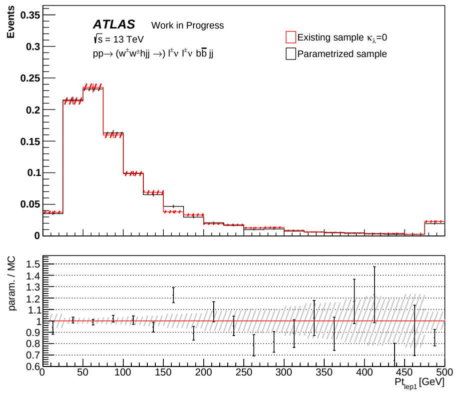

(a)

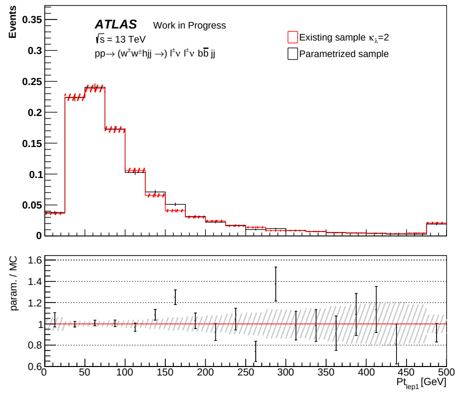

(b)

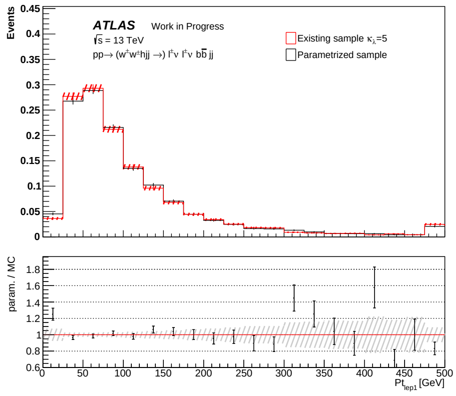

(c)

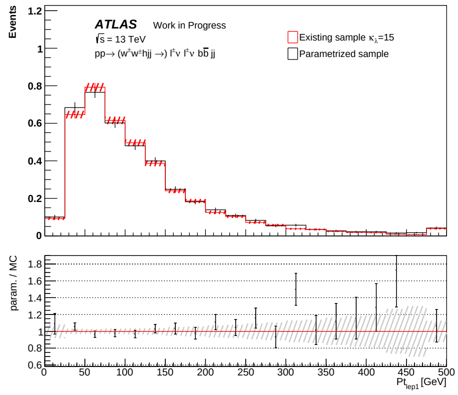

(d)

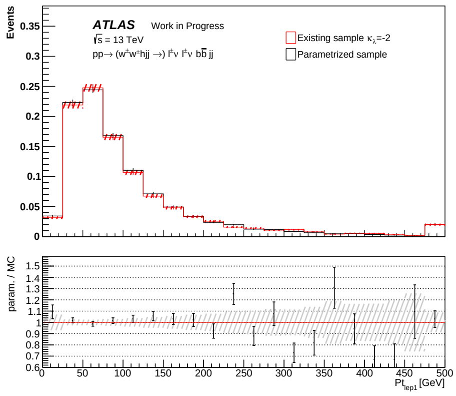

(e)

Figure A.4: Transverse momentum of the leading lepton of $\kappa_\lambda = 0$ (a), $\kappa_\lambda = 2$ (b), $\kappa_\lambda = 5$ (c), $\kappa_\lambda = 15$ (d) and $\kappa_\lambda = -2$ (e) in comparison to the respective κ_λ sample obtained with the parametrization shown in equation 4.1.

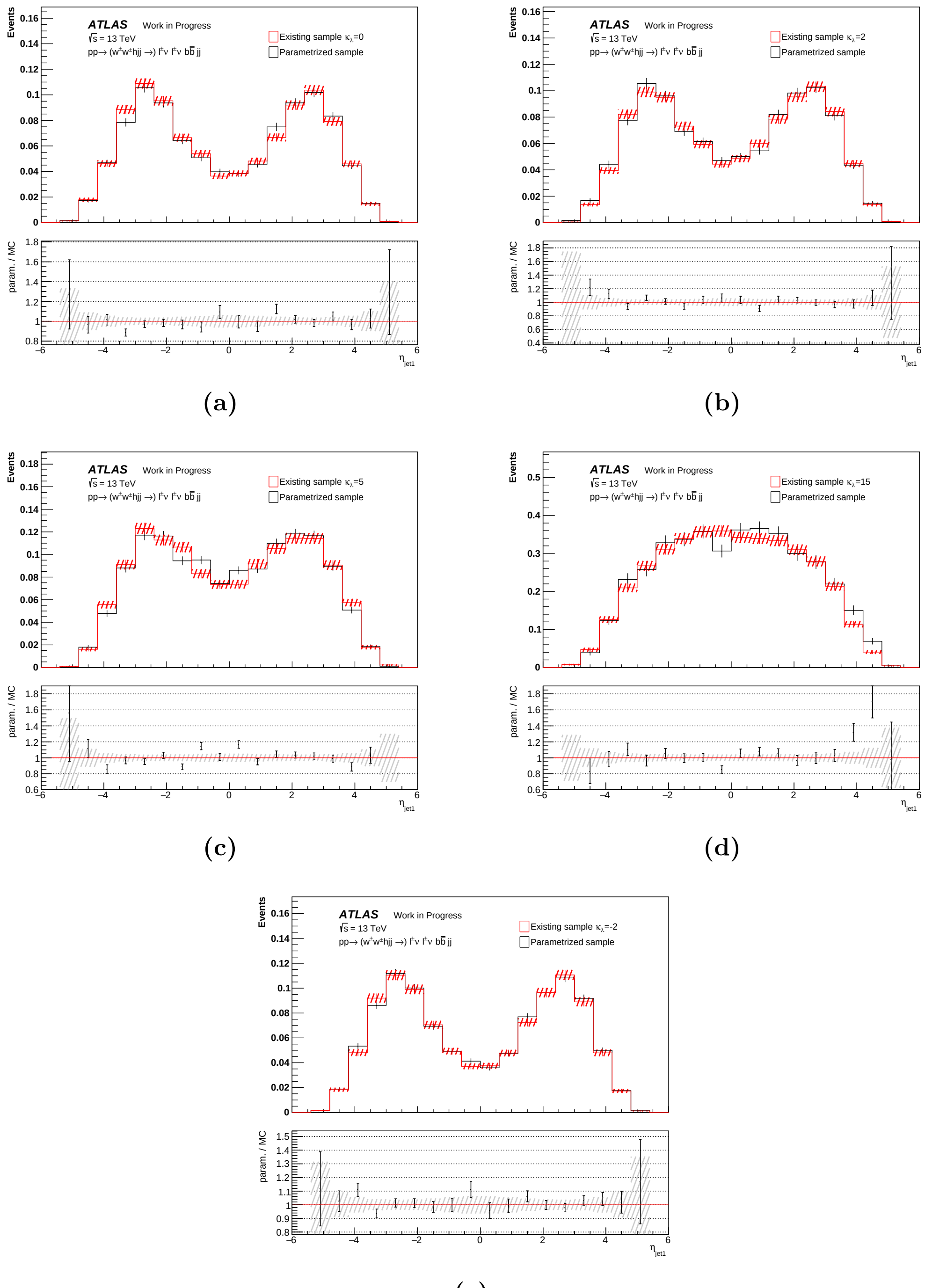

(e)

Figure A.5: Pseudorapidity of the leading jet of $\kappa_\lambda = 0$ (a), $\kappa_\lambda = 2$ (b), $\kappa_\lambda = 5$ (c), $\kappa_\lambda = 15$ (d) and $\kappa_\lambda = -2$ (e) in comparison to the respective κ_λ sample obtained with the parametrization shown in equation 4.1.

A.6 Overview of Detector-Level Monte Carlo Samples

Table A.1: VBS ssWWh signal samples used in the analysis, with information on their generation and cross-section, which already takes the decay of the W Bosons to Electrons and Muons and the Higgs Boson to two b-quarks into account. These MC samples were generated with MadGraph5_aMC@NLO + Pythia8.

Value of κ_λ	σ[fb]	k-factor	ϵ_{filter}	N_events generated	DSID
1	0.0105	1.0	1.0	400,000	525362
2	0.0110	1.0	1.0	190,000	525363
5	0.0143	1.0	1.0	190,000	525364
10	0.0260	1.0	1.0	190,000	525365
-5	0.01423	1.0	1.0	190,000	525366

Table A.2: "Summary of nominal SM background processes considered in the analysis along with a description of the event generators used and the associated dataset identifier number."Taken from [29].

Process	Generator	DSID
	Top	
$t\bar{t}$	Powheg+Pythia8	410470-410472
$t\bar{t}+W$	MadGraph5_aMC@NLO + Pythia8	410155
$t\bar{t}+Z(\rightarrow\nu\nu,\rightarrow qq)$	MadGraph5_aMC@NLO + Pythia8	410156, 410157
$t\bar{t}+Z(\rightarrow ee,\rightarrow\mu\mu,\rightarrow\tau\tau)$	MadGraph5_aMC@NLO + Pythia8	410218-410220
single-top s-channel, lept	Powheg+Pythia8	410644, 410645
single-top t-channel, lept	Powheg+Pythia8	410658, 410659
single-top Wt, dilepton (Diagram Removal)	Powheg+Pythia8	410648, 410649
	V+jets	
$Z(\rightarrow\mu\mu)$ +jets	Sherpa 2.2.1	364100-364113
$Z(\rightarrow ee)$ +jets	Sherpa 2.2.1	364114-364127
$Z(\rightarrow\tau\tau)$ +jets	Sherpa 2.2.1	364128-364141
$Z(\rightarrow\mu\mu)$ +jets, lowmass	Sherpa 2.2.1	364198-364203
$Z(\rightarrow ee)$ +jets, lowmass	Sherpa 2.2.1	364204-364209
$Z(\rightarrow\tau\tau)$ +jets, lowmass	Sherpa 2.2.1	364210-364215
Z +jets, very lowmass	Sherpa 2.2.1	364358-364363
Z +jets, EW	Sherpa 2.2.1	308092-308094
$W(\rightarrow\mu\nu)$ +jets	Sherpa 2.2.1	364156-364169
$W(\rightarrow e\nu)$ +jets	Sherpa 2.2.1	364170-364183
$W(\rightarrow\tau\nu)$ +jets	Sherpa 2.2.1	364184-364197
W +jets, EW	Sherpa 2.2.1	308096-308098
	VV	
$ZZ(\rightarrow qq,\rightarrow\nu\nu)$	Sherpa 2.2.1	363355
$ZZ(\rightarrow qq,\rightarrow\ell\ell)$	Sherpa 2.2.1	363356
$WZ(\rightarrow qq,\rightarrow\nu\nu)$	Sherpa 2.2.1	363357
$WZ(\rightarrow qq,\rightarrow\ell\ell)$	Sherpa 2.2.1	363358
$WW(\rightarrow qq,\rightarrow\ell\nu)$	Sherpa 2.2.1	363359-363360
$WZ(\rightarrow\ell\nu,\rightarrow qq)$	Sherpa 2.2.1	363489
$4\ell, 3\ell1\nu, 2\ell2\nu, 1\ell3\nu$	Sherpa 2.2.2	364250, 364253-364255
$4\ell, 2\ell2\nu$ (low-m_{ll})	Sherpa 2.2.2	364288-364290
$4\ell+jj, 3\ell1\nu+jj, 2\ell2\nu+jj$ (EW6)	Sherpa 2.2.2	366086, 366087, 366088-366089
$gg\rightarrow VV(\rightarrow 4\ell)$	Sherpa 2.2.2	345708-345709
$gg\rightarrow VV(\rightarrow 2\ell2\nu)$, inclusive	Sherpa 2.2.2	345714
$gg\rightarrow VV(\rightarrow 2\ell2\nu)$, w/ Higgs	Sherpa 2.2.2	345715, 345718, 345723
$gg\rightarrow VV(\rightarrow 2\ell2\nu)$, w/o Higgs	Sherpa 2.2.2	345716, 345720, 345725
$gg\rightarrow VV$, semilep	Sherpa 2.2.2	364302-364305
	Single Higgs	
$ggH, H(\rightarrow\tau\tau,\rightarrow WW,\rightarrow bb)$	Powheg+Pythia8	345120-345123, 345324, 345057
$VBF, H(\rightarrow\tau\tau,\rightarrow WW,\rightarrow bb)$	Powheg+Pythia8	346190-346193, 345948, 345949
$WH, H(\rightarrow\tau\tau,\rightarrow WW)$	Powheg MINLO+Pythia8	345211-345212; 345325, 346561, 345433, 346560, 345054, 345053
$ZH, H(\rightarrow\tau\tau,\rightarrow WW,\rightarrow bb)$	Powheg MINLO+Pythia8	345217, 345336, 346524, 345055
ttH	Powheg+Pythia8	346343-346345

A.7 List of Monte Carlo Samples

To facilitate reproducibility we provide this list of all used MC samples. For readability reasons, we only list samples corresponding to the campaign mc16a (R-tag of r9364). These samples also exist for mc16d (R-tag of r10201) and mc16e (R-tag of r10724).

The sample names are constructed in the following manner:

$$\underbrace{mc16\_13TeV}_{\text{MC campaing and center of mass energy}} . \underbrace{525362}_{\text{DSID}} . \underbrace{MGPy8EG\_ssWWhjj\_llvvbbjj\_EW8\_LO\_klp1}_{\text{Short description of the physics process}}$$

$$\underbrace{deriv.DAOD\_SUSY2}_{\text{file format}} . \underbrace{e8545}_{\text{generation tag}} \_ \underbrace{s3126}_{\text{simulation tag}} \_ \underbrace{r9364}_{\text{reconstruction tag}} \_ \underbrace{p3990}_{\text{version of derivation}}$$

VBS ssWWh
mc16_13TeV.525362.MGPy8EG_ssWWhjj_llvvbbjj_EW8_LO_klp1.deriv.DAOD_SUSY2.e8545_s3126_r9364_p3990
mc16_13TeV.525363.MGPy8EG_ssWWhjj_llvvbbjj_EW8_LO_klp2.deriv.DAOD_SUSY2.e8545_s3126_r9364_p3990
mc16_13TeV.525364.MGPy8EG_ssWWhjj_llvvbbjj_EW8_LO_klp5.deriv.DAOD_SUSY2.e8545_s3126_r9364_p3990
mc16_13TeV.525365.MGPy8EG_ssWWhjj_llvvbbjj_EW8_LO_klp10.deriv.DAOD_SUSY2.e8545_s3126_r9364_p3990
mc16_13TeV.525366.MGPy8EG_ssWWhjj_llvvbbjj_EW8_LO_klm5.deriv.DAOD_SUSY2.e8545_s3126_r9364_p3990

$t\bar{t}$
mc16_13TeV.410470.PhPy8EG_A14_ttbar_hdamp258p75_nonallhad.DAOD_SUSY2.e6337_a875_r9364_p4458
mc16_13TeV.410470.PhPy8EG_A14_ttbar_hdamp258p75_nonallhad.DAOD_SUSY2.e6337_s3126_r9364_p4189
mc16_13TeV.410471.PhPy8EG_A14_ttbar_hdamp258p75_allhad.DAOD_SUSY2.e6337_a875_r9364_p4458
mc16_13TeV.410471.PhPy8EG_A14_ttbar_hdamp258p75_allhad.DAOD_SUSY2.e6337_s3126_r9364_p4189
mc16_13TeV.410472.PhPy8EG_A14_ttbar_hdamp258p75_dil.DAOD_SUSY2.e6348_a875_r9364_p4458
mc16_13TeV.410472.PhPy8EG_A14_ttbar_hdamp258p75_dil.DAOD_SUSY2.e6348_s3126_r9364_p4189

$t\bar{t} + V$
mc16_13TeV.410155.aMcAtNloPythia8EvtGen_MEN30NLO_A14N23LO_ttW.DAOD_SUSY2.e5070_s3126_r9364_p4189
mc16_13TeV.410156.aMcAtNloPythia8EvtGen_MEN30NLO_A14N23LO_ttZnunu.DAOD_SUSY2.e5070_s3126_r9364_p4189
mc16_13TeV.410157.aMcAtNloPythia8EvtGen_MEN30NLO_A14N23LO_ttZqq.DAOD_SUSY2.e5070_s3126_r9364_p4189
mc16_13TeV.410218.aMcAtNloPythia8EvtGen_MEN30NLO_A14N23LO_ttee.DAOD_SUSY2.e5070_s3126_r9364_p4189
mc16_13TeV.410219.aMcAtNloPythia8EvtGen_MEN30NLO_A14N23LO_ttmumu.DAOD_SUSY2.e5070_s3126_r9364_p4189
mc16_13TeV.410220.aMcAtNloPythia8EvtGen_MEN30NLO_A14N23LO_tttautau.DAOD_SUSY2.e5070_s3126_r9364_p4189

Single top
mc16_13TeV.410644.PowhegPythia8EvtGen_A14_singletop_schan_lept_top.DAOD_SUSY2.e6527_s3126_r9364_p4189
mc16_13TeV.410645.PowhegPythia8EvtGen_A14_singletop_schan_lept_antitop.DAOD_SUSY2.e6527_s3126_r9364_p4189
mc16_13TeV.410648.PowhegPythia8EvtGen_A14_Wt_DR_dilepton_top.DAOD_SUSY2.e6615_a875_r9364_p4189
mc16_13TeV.410648.PowhegPythia8EvtGen_A14_Wt_DR_dilepton_top.DAOD_SUSY2.e6615_s3126_r9364_p4189
mc16_13TeV.410649.PowhegPythia8EvtGen_A14_Wt_DR_dilepton_antitop.DAOD_SUSY2.e6615_a875_r9364_p4189
mc16_13TeV.410649.PowhegPythia8EvtGen_A14_Wt_DR_dilepton_antitop.DAOD_SUSY2.e6615_s3126_r9364_p4189
mc16_13TeV.410658.PhPy8EG_A14_tchan_BW50_lept_top.DAOD_SUSY2.e6671_s3126_r9364_p4189
mc16_13TeV.410659.PhPy8EG_A14_tchan_BW50_lept_antitop.DAOD_SUSY2.e6671_s3126_r9364_p4189

Z+jets

mc16_13TeV.308092.Sherpa_221_NNPDF30NNLO_Zee2jets_Min_N_TChannel.DAOD_SUSY2.e5767_s3126_r9364_p4189
mc16_13TeV.308093.Sherpa_221_NNPDF30NNLO_Zmm2jets_Min_N_TChannel.DAOD_SUSY2.e5767_s3126_r9364_p4189
mc16_13TeV.308094.Sherpa_221_NNPDF30NNLO_Ztautau2jets_Min_N_TChannel.DAOD_SUSY2.e5767_s3126_r9364_p4189
mc16_13TeV.364100.Sherpa_221_NNPDF30NNLO_Zmumu_MAXHTPTV0_70_CVetoBVeto.DAOD_SUSY2.e5271_s3126_r9364_p4189
mc16_13TeV.364101.Sherpa_221_NNPDF30NNLO_Zmumu_MAXHTPTV0_70_CFilterBVeto.DAOD_SUSY2.e5271_s3126_r9364_p4189
mc16_13TeV.364102.Sherpa_221_NNPDF30NNLO_Zmumu_MAXHTPTV0_70_BFilter.DAOD_SUSY2.e5271_s3126_r9364_p4189
mc16_13TeV.364103.Sherpa_221_NNPDF30NNLO_Zmumu_MAXHTPTV70_140_CVetoBVeto.DAOD_SUSY2.e5271_s3126_r9364_p4189
mc16_13TeV.364104.Sherpa_221_NNPDF30NNLO_Zmumu_MAXHTPTV70_140_CFilterBVeto.DAOD_SUSY2.e5271_s3126_r9364_p4189
mc16_13TeV.364105.Sherpa_221_NNPDF30NNLO_Zmumu_MAXHTPTV70_140_BFilter.DAOD_SUSY2.e5271_s3126_r9364_p4189
mc16_13TeV.364106.Sherpa_221_NNPDF30NNLO_Zmumu_MAXHTPTV140_280_CVetoBVeto.DAOD_SUSY2.e5271_s3126_r9364_p4189
mc16_13TeV.364107.Sherpa_221_NNPDF30NNLO_Zmumu_MAXHTPTV140_280_CFilterBVeto.DAOD_SUSY2.e5271_s3126_r9364_p4189
mc16_13TeV.364108.Sherpa_221_NNPDF30NNLO_Zmumu_MAXHTPTV140_280_BFilter.DAOD_SUSY2.e5271_s3126_r9364_p4189
mc16_13TeV.364109.Sherpa_221_NNPDF30NNLO_Zmumu_MAXHTPTV280_500_CVetoBVeto.DAOD_SUSY2.e5271_s3126_r9364_p4189
mc16_13TeV.364110.Sherpa_221_NNPDF30NNLO_Zmumu_MAXHTPTV280_500_CFilterBVeto.DAOD_SUSY2.e5271_s3126_r9364_p4189
mc16_13TeV.364111.Sherpa_221_NNPDF30NNLO_Zmumu_MAXHTPTV280_500_BFilter.DAOD_SUSY2.e5271_s3126_r9364_p4189
mc16_13TeV.364112.Sherpa_221_NNPDF30NNLO_Zmumu_MAXHTPTV500_1000.DAOD_SUSY2.e5271_s3126_r9364_p4189
mc16_13TeV.364113.Sherpa_221_NNPDF30NNLO_Zmumu_MAXHTPTV1000_E_CMS.DAOD_SUSY2.e5271_s3126_r9364_p4189
mc16_13TeV.364114.Sherpa_221_NNPDF30NNLO_Zee_MAXHTPTV0_70_CVetoBVeto.DAOD_SUSY2.e5299_s3126_r9364_p4189
mc16_13TeV.364115.Sherpa_221_NNPDF30NNLO_Zee_MAXHTPTV0_70_CFilterBVeto.DAOD_SUSY2.e5299_s3126_r9364_p4189
mc16_13TeV.364116.Sherpa_221_NNPDF30NNLO_Zee_MAXHTPTV0_70_BFilter.DAOD_SUSY2.e5299_s3126_r9364_p4189
mc16_13TeV.364117.Sherpa_221_NNPDF30NNLO_Zee_MAXHTPTV70_140_CVetoBVeto.DAOD_SUSY2.e5299_s3126_r9364_p4189
mc16_13TeV.364118.Sherpa_221_NNPDF30NNLO_Zee_MAXHTPTV70_140_CFilterBVeto.DAOD_SUSY2.e5299_s3126_r9364_p4189
mc16_13TeV.364119.Sherpa_221_NNPDF30NNLO_Zee_MAXHTPTV70_140_BFilter.DAOD_SUSY2.e5299_s3126_r9364_p4189
mc16_13TeV.364120.Sherpa_221_NNPDF30NNLO_Zee_MAXHTPTV140_280_CVetoBVeto.DAOD_SUSY2.e5299_s3126_r9364_p4189
mc16_13TeV.364121.Sherpa_221_NNPDF30NNLO_Zee_MAXHTPTV140_280_CFilterBVeto.DAOD_SUSY2.e5299_s3126_r9364_p4189
mc16_13TeV.364122.Sherpa_221_NNPDF30NNLO_Zee_MAXHTPTV140_280_BFilter.DAOD_SUSY2.e5299_s3126_r9364_p4189

mc16_13TeV.364123.Sherpa_221_NNPDF30NNLO_Zee_MAXHTPTV280_500_CVetoBVeto.DAOD_SUSY2.e5299_s3126_r9364_p4189
mc16_13TeV.364124.Sherpa_221_NNPDF30NNLO_Zee_MAXHTPTV280_500_CFilterBVeto.DAOD_SUSY2.e5299_s3126_r9364_p4189
mc16_13TeV.364125.Sherpa_221_NNPDF30NNLO_Zee_MAXHTPTV280_500_BFilter.DAOD_SUSY2.e5299_s3126_r9364_p4189
mc16_13TeV.364126.Sherpa_221_NNPDF30NNLO_Zee_MAXHTPTV500_1000.DAOD_SUSY2.e5299_s3126_r9364_p4189
mc16_13TeV.364127.Sherpa_221_NNPDF30NNLO_Zee_MAXHTPTV1000_E_CMS.DAOD_SUSY2.e5299_s3126_r9364_p4189
mc16_13TeV.364128.Sherpa_221_NNPDF30NNLO_Ztautau_MAXHTPTV0_70_CVetoBVeto.DAOD_SUSY2.e5307_s3126_r9364_p4189
mc16_13TeV.364129.Sherpa_221_NNPDF30NNLO_Ztautau_MAXHTPTV0_70_CFilterBVeto.DAOD_SUSY2.e5307_s3126_r9364_p4189
mc16_13TeV.364130.Sherpa_221_NNPDF30NNLO_Ztautau_MAXHTPTV0_70_BFilter.DAOD_SUSY2.e5307_s3126_r9364_p4189
mc16_13TeV.364131.Sherpa_221_NNPDF30NNLO_Ztautau_MAXHTPTV70_140_CVetoBVeto.DAOD_SUSY2.e5307_s3126_r9364_p4189
mc16_13TeV.364132.Sherpa_221_NNPDF30NNLO_Ztautau_MAXHTPTV70_140_CFilterBVeto.DAOD_SUSY2.e5307_s3126_r9364_p4189
mc16_13TeV.364133.Sherpa_221_NNPDF30NNLO_Ztautau_MAXHTPTV70_140_BFilter.DAOD_SUSY2.e5307_s3126_r9364_p4189
mc16_13TeV.364134.Sherpa_221_NNPDF30NNLO_Ztautau_MAXHTPTV140_280_CVetoBVeto.DAOD_SUSY2.e5307_s3126_r9364_p4189
mc16_13TeV.364135.Sherpa_221_NNPDF30NNLO_Ztautau_MAXHTPTV140_280_CFilterBVeto.DAOD_SUSY2.e5307_s3126_r9364_p4189
mc16_13TeV.364136.Sherpa_221_NNPDF30NNLO_Ztautau_MAXHTPTV140_280_BFilter.DAOD_SUSY2.e5307_s3126_r9364_p4189
mc16_13TeV.364137.Sherpa_221_NNPDF30NNLO_Ztautau_MAXHTPTV280_500_CVetoBVeto.DAOD_SUSY2.e5307_s3126_r9364_p4189
mc16_13TeV.364138.Sherpa_221_NNPDF30NNLO_Ztautau_MAXHTPTV280_500_CFilterBVeto.DAOD_SUSY2.e5313_s3126_r9364_p4189
mc16_13TeV.364139.Sherpa_221_NNPDF30NNLO_Ztautau_MAXHTPTV280_500_BFilter.DAOD_SUSY2.e5313_s3126_r9364_p4189
mc16_13TeV.364140.Sherpa_221_NNPDF30NNLO_Ztautau_MAXHTPTV500_1000.DAOD_SUSY2.e5307_s3126_r9364_p4189
mc16_13TeV.364141.Sherpa_221_NNPDF30NNLO_Ztautau_MAXHTPTV1000_E_CMS.DAOD_SUSY2.e5307_s3126_r9364_p4189
mc16_13TeV.364198.Sherpa_221_NN30NNLO_Zmm_Mll10_40_MAXHTPTV0_70_BVeto.DAOD_SUSY2.e5421_s3126_r9364_p4189
mc16_13TeV.364199.Sherpa_221_NN30NNLO_Zmm_Mll10_40_MAXHTPTV0_70_BFilter.DAOD_SUSY2.e5421_s3126_r9364_p4189
mc16_13TeV.364200.Sherpa_221_NN30NNLO_Zmm_Mll10_40_MAXHTPTV70_280_BVeto.DAOD_SUSY2.e5421_s3126_r9364_p4189
mc16_13TeV.364201.Sherpa_221_NN30NNLO_Zmm_Mll10_40_MAXHTPTV70_280_BFilter.DAOD_SUSY2.e5421_s3126_r9364_p4189
mc16_13TeV.364202.Sherpa_221_NN30NNLO_Zmm_Mll10_40_MAXHTPTV280_E_CMS_BVeto.DAOD_SUSY2.e5421_s3126_r9364_p4189
mc16_13TeV.364203.Sherpa_221_NN30NNLO_Zmm_Mll10_40_MAXHTPTV280_E_CMS_BFilter.DAOD_SUSY2.e5421_s3126_r9364_p4189
mc16_13TeV.364204.Sherpa_221_NN30NNLO_Zee_Mll10_40_MAXHTPTV0_70_BVeto.DAOD_SUSY2.e5421_s3126_r9364_p4189
mc16_13TeV.364205.Sherpa_221_NN30NNLO_Zee_Mll10_40_MAXHTPTV0_70_BFilter.DAOD_SUSY2.e5421_s3126_r9364_p4189
mc16_13TeV.364206.Sherpa_221_NN30NNLO_Zee_Mll10_40_MAXHTPTV70_280_BVeto.DAOD_SUSY2.e5421_s3126_r9364_p4189
mc16_13TeV.364207.Sherpa_221_NN30NNLO_Zee_Mll10_40_MAXHTPTV70_280_BFilter.DAOD_SUSY2.e5421_s3126_r9364_p4189
mc16_13TeV.364208.Sherpa_221_NN30NNLO_Zee_Mll10_40_MAXHTPTV280_E_CMS_BVeto.DAOD_SUSY2.e5421_s3126_r9364_p4189
mc16_13TeV.364209.Sherpa_221_NN30NNLO_Zee_Mll10_40_MAXHTPTV280_E_CMS_BFilter.DAOD_SUSY2.e5421_s3126_r9364_p4189
mc16_13TeV.364210.Sherpa_221_NN30NNLO_Ztt_Mll10_40_MAXHTPTV0_70_BVeto.DAOD_SUSY2.e5421_s3126_r9364_p4189
mc16_13TeV.364211.Sherpa_221_NN30NNLO_Ztt_Mll10_40_MAXHTPTV0_70_BFilter.DAOD_SUSY2.e5421_s3126_r9364_p4189
mc16_13TeV.364212.Sherpa_221_NN30NNLO_Ztt_Mll10_40_MAXHTPTV70_280_BVeto.DAOD_SUSY2.e5421_s3126_r9364_p4189
mc16_13TeV.364213.Sherpa_221_NN30NNLO_Ztt_Mll10_40_MAXHTPTV70_280_BFilter.DAOD_SUSY2.e5421_s3126_r9364_p4189
mc16_13TeV.364214.Sherpa_221_NN30NNLO_Ztt_Mll10_40_MAXHTPTV280_E_CMS_BVeto.DAOD_SUSY2.e5421_s3126_r9364_p4189
mc16_13TeV.364215.Sherpa_221_NN30NNLO_Ztt_Mll10_40_MAXHTPTV280_E_CMS_BFilter.DAOD_SUSY2.e5421_s3126_r9364_p4189
mc16_13TeV.364358.Sherpa_221_NNPDF30NNLO_Zee_Mll2Ml_MAXHTPTV70_140.DAOD_SUSY2.e6544_a875_r9364_p4189
mc16_13TeV.364359.Sherpa_221_NNPDF30NNLO_Zmumu_Mll2Ml_MAXHTPTV70_140.DAOD_SUSY2.e6544_a875_r9364_p4189
mc16_13TeV.364360.Sherpa_221_NNPDF30NNLO_Ztautau_Mll2Ml_MAXHTPTV70_140.DAOD_SUSY2.e6544_a875_r9364_p4189
mc16_13TeV.364361.Sherpa_221_NNPDF30NNLO_Zee_Mll2Ml_MAXHTPTV140_280.DAOD_SUSY2.e6544_a875_r9364_p4189
mc16_13TeV.364362.Sherpa_221_NNPDF30NNLO_Zmumu_Mll2Ml_MAXHTPTV140_280.DAOD_SUSY2.e6544_a875_r9364_p4189
mc16_13TeV.364363.Sherpa_221_NNPDF30NNLO_Ztautau_Mll2Ml_MAXHTPTV140_280.DAOD_SUSY2.e6544_a875_r9364_p4189

W+jets
mc16_13TeV.364156.Sherpa_221_NNPDF30NNLO_Wmunu_MAXHTPTV0_70_CVetoBVeto.DAOD_SUSY2.e5340_s3126_r9364_p4189
mc16_13TeV.364157.Sherpa_221_NNPDF30NNLO_Wmunu_MAXHTPTV0_70_CFilterBVeto.DAOD_SUSY2.e5340_s3126_r9364_p4189
mc16_13TeV.364158.Sherpa_221_NNPDF30NNLO_Wmunu_MAXHTPTV0_70_BFilter.DAOD_SUSY2.e5340_s3126_r9364_p4189
mc16_13TeV.364159.Sherpa_221_NNPDF30NNLO_Wmunu_MAXHTPTV70_140_CVetoBVeto.DAOD_SUSY2.e5340_s3126_r9364_p4189
mc16_13TeV.364160.Sherpa_221_NNPDF30NNLO_Wmunu_MAXHTPTV70_140_CFilterBVeto.DAOD_SUSY2.e5340_s3126_r9364_p4189
mc16_13TeV.364161.Sherpa_221_NNPDF30NNLO_Wmunu_MAXHTPTV70_140_BFilter.DAOD_SUSY2.e5340_s3126_r9364_p4189
mc16_13TeV.364162.Sherpa_221_NNPDF30NNLO_Wmunu_MAXHTPTV140_280_CVetoBVeto.DAOD_SUSY2.e5340_s3126_r9364_p4189
mc16_13TeV.364163.Sherpa_221_NNPDF30NNLO_Wmunu_MAXHTPTV140_280_CFilterBVeto.DAOD_SUSY2.e5340_s3126_r9364_p4189
mc16_13TeV.364164.Sherpa_221_NNPDF30NNLO_Wmunu_MAXHTPTV140_280_BFilter.DAOD_SUSY2.e5340_s3126_r9364_p4189
mc16_13TeV.364165.Sherpa_221_NNPDF30NNLO_Wmunu_MAXHTPTV280_500_CVetoBVeto.DAOD_SUSY2.e5340_s3126_r9364_p4189
mc16_13TeV.364166.Sherpa_221_NNPDF30NNLO_Wmunu_MAXHTPTV280_500_CFilterBVeto.DAOD_SUSY2.e5340_s3126_r9364_p4189
mc16_13TeV.364167.Sherpa_221_NNPDF30NNLO_Wmunu_MAXHTPTV280_500_BFilter.DAOD_SUSY2.e5340_s3126_r9364_p4189
mc16_13TeV.364168.Sherpa_221_NNPDF30NNLO_Wmunu_MAXHTPTV500_1000.DAOD_SUSY2.e5340_s3126_r9364_p4189
mc16_13TeV.364169.Sherpa_221_NNPDF30NNLO_Wmunu_MAXHTPTV1000_E_CMS.DAOD_SUSY2.e5340_s3126_r9364_p4189
mc16_13TeV.364170.Sherpa_221_NNPDF30NNLO_Wenu_MAXHTPTV0_70_CVetoBVeto.DAOD_SUSY2.e5340_s3126_r9364_p4189
mc16_13TeV.364171.Sherpa_221_NNPDF30NNLO_Wenu_MAXHTPTV0_70_CFilterBVeto.DAOD_SUSY2.e5340_s3126_r9364_p4189
mc16_13TeV.364172.Sherpa_221_NNPDF30NNLO_Wenu_MAXHTPTV0_70_BFilter.DAOD_SUSY2.e5340_s3126_r9364_p4189
mc16_13TeV.364173.Sherpa_221_NNPDF30NNLO_Wenu_MAXHTPTV70_140_CVetoBVeto.DAOD_SUSY2.e5340_s3126_r9364_p4189
mc16_13TeV.364174.Sherpa_221_NNPDF30NNLO_Wenu_MAXHTPTV70_140_CFilterBVeto.DAOD_SUSY2.e5340_s3126_r9364_p4189
mc16_13TeV.364175.Sherpa_221_NNPDF30NNLO_Wenu_MAXHTPTV70_140_BFilter.DAOD_SUSY2.e5340_s3126_r9364_p4189
mc16_13TeV.364176.Sherpa_221_NNPDF30NNLO_Wenu_MAXHTPTV140_280_CVetoBVeto.DAOD_SUSY2.e5340_s3126_r9364_p4189
mc16_13TeV.364177.Sherpa_221_NNPDF30NNLO_Wenu_MAXHTPTV140_280_CFilterBVeto.DAOD_SUSY2.e5340_s3126_r9364_p4189
mc16_13TeV.364178.Sherpa_221_NNPDF30NNLO_Wenu_MAXHTPTV140_280_BFilter.DAOD_SUSY2.e5340_s3126_r9364_p4189
mc16_13TeV.364179.Sherpa_221_NNPDF30NNLO_Wenu_MAXHTPTV280_500_CVetoBVeto.DAOD_SUSY2.e5340_s3126_r9364_p4189
mc16_13TeV.364180.Sherpa_221_NNPDF30NNLO_Wenu_MAXHTPTV280_500_CFilterBVeto.DAOD_SUSY2.e5340_s3126_r9364_p4189
mc16_13TeV.364181.Sherpa_221_NNPDF30NNLO_Wenu_MAXHTPTV280_500_BFilter.DAOD_SUSY2.e5340_s3126_r9364_p4189
mc16_13TeV.364182.Sherpa_221_NNPDF30NNLO_Wenu_MAXHTPTV500_1000.DAOD_SUSY2.e5340_s3126_r9364_p4189
mc16_13TeV.364183.Sherpa_221_NNPDF30NNLO_Wenu_MAXHTPTV1000_E_CMS.DAOD_SUSY2.e5340_s3126_r9364_p4189
mc16_13TeV.364184.Sherpa_221_NNPDF30NNLO_Wtaunu_MAXHTPTV0_70_CVetoBVeto.DAOD_SUSY2.e5340_s3126_r9364_p4189
mc16_13TeV.364185.Sherpa_221_NNPDF30NNLO_Wtaunu_MAXHTPTV0_70_CFilterBVeto.DAOD_SUSY2.e5340_s3126_r9364_p4189
mc16_13TeV.364186.Sherpa_221_NNPDF30NNLO_Wtaunu_MAXHTPTV0_70_BFilter.DAOD_SUSY2.e5340_s3126_r9364_p4189
mc16_13TeV.364187.Sherpa_221_NNPDF30NNLO_Wtaunu_MAXHTPTV70_140_CVetoBVeto.DAOD_SUSY2.e5340_s3126_r9364_p4189
mc16_13TeV.364188.Sherpa_221_NNPDF30NNLO_Wtaunu_MAXHTPTV70_140_CFilterBVeto.DAOD_SUSY2.e5340_s3126_r9364_p4189
mc16_13TeV.364189.Sherpa_221_NNPDF30NNLO_Wtaunu_MAXHTPTV70_140_BFilter.DAOD_SUSY2.e5340_s3126_r9364_p4189
mc16_13TeV.364190.Sherpa_221_NNPDF30NNLO_Wtaunu_MAXHTPTV140_280_CVetoBVeto.DAOD_SUSY2.e5340_s3126_r9364_p4189
mc16_13TeV.364191.Sherpa_221_NNPDF30NNLO_Wtaunu_MAXHTPTV140_280_CFilterBVeto.DAOD_SUSY2.e5340_s3126_r9364_p4189
mc16_13TeV.364192.Sherpa_221_NNPDF30NNLO_Wtaunu_MAXHTPTV140_280_BFilter.DAOD_SUSY2.e5340_s3126_r9364_p4189
mc16_13TeV.364193.Sherpa_221_NNPDF30NNLO_Wtaunu_MAXHTPTV280_500_CVetoBVeto.DAOD_SUSY2.e5340_s3126_r9364_p4189
mc16_13TeV.364194.Sherpa_221_NNPDF30NNLO_Wtaunu_MAXHTPTV280_500_CFilterBVeto.DAOD_SUSY2.e5340_s3126_r9364_p4189
mc16_13TeV.364195.Sherpa_221_NNPDF30NNLO_Wtaunu_MAXHTPTV280_500_BFilter.DAOD_SUSY2.e5340_s3126_r9364_p4189
mc16_13TeV.364196.Sherpa_221_NNPDF30NNLO_Wtaunu_MAXHTPTV500_1000.DAOD_SUSY2.e5340_s3126_r9364_p4189
mc16_13TeV.364197.Sherpa_221_NNPDF30NNLO_Wtaunu_MAXHTPTV1000_E_CMS.DAOD_SUSY2.e5340_s3126_r9364_p4189
mc16_13TeV.308096.Sherpa_221_NNPDF30NNLO_Wenu2jets_Min_N_TChannel.DAOD_SUSY2.e5789_s3126_r9364_p4189

mc16_13TeV.308097.Sherpa_221_NNPDF30NNLO_Wmunu2jets_Min_N_TChannel.DAOD_SUSY2.e5767_s3126_r9364_p4189
mc16_13TeV.308098.Sherpa_221_NNPDF30NNLO_Wtaunu2jets_Min_N_TChannel.DAOD_SUSY2.e5767_s3126_r9364_p4189

VV (Diboson)
mc16_13TeV.345708.Sherpa_222_NNPDF30NNLO_ggllllNoHiggs_0M4l130.DAOD_SUSY2.e6213_s3126_r9364_p4458
mc16_13TeV.345709.Sherpa_222_NNPDF30NNLO_ggllllNoHiggs_130M4l.DAOD_SUSY2.e6213_s3126_r9364_p4458
mc16_13TeV.345714.Sherpa_222_NNPDF30NNLO_ggllvv.DAOD_SUSY2.e7668_s3126_r9364_p4458
mc16_13TeV.345715.Sherpa_222_NNPDF30NNLO_ggllvvInt.DAOD_SUSY2.e6525_s3126_r9364_p4189
mc16_13TeV.345716.Sherpa_222_NNPDF30NNLO_ggllvvIntNoHiggs.DAOD_SUSY2.e6480_s3126_r9364_p4458
mc16_13TeV.345718.Sherpa_222_NNPDF30NNLO_ggllvvWW.DAOD_SUSY2.e6525_s3126_r9364_p4189
mc16_13TeV.345720.Sherpa_222_NNPDF30NNLO_ggllvvWWNoHiggs.DAOD_SUSY2.e6937_s3126_r9364_p4458
mc16_13TeV.345723.Sherpa_222_NNPDF30NNLO_ggllvvZZ.DAOD_SUSY2.e6213_s3126_r9364_p4189
mc16_13TeV.345725.Sherpa_222_NNPDF30NNLO_ggllvvZZNoHiggs.DAOD_SUSY2.e6213_s3126_r9364_p4458
mc16_13TeV.363355.Sherpa_221_NNPDF30NNLO_ZqqZvv.DAOD_SUSY2.e5525_s3126_r9364_p4189
mc16_13TeV.363356.Sherpa_221_NNPDF30NNLO_ZqqZll.DAOD_SUSY2.e5525_s3126_r9364_p4189
mc16_13TeV.363357.Sherpa_221_NNPDF30NNLO_WqqZvv.DAOD_SUSY2.e5525_s3126_r9364_p4189
mc16_13TeV.363358.Sherpa_221_NNPDF30NNLO_WqqZll.DAOD_SUSY2.e5525_s3126_r9364_p4189
mc16_13TeV.363359.Sherpa_221_NNPDF30NNLO_WpqqWmlv.DAOD_SUSY2.e5583_s3126_r9364_p4189
mc16_13TeV.363360.Sherpa_221_NNPDF30NNLO_WplvWmqq.DAOD_SUSY2.e5983_s3126_r9364_p4189
mc16_13TeV.363489.Sherpa_221_NNPDF30NNLO_WlvZqq.DAOD_SUSY2.e5525_s3126_r9364_p4189
mc16_13TeV.364250.Sherpa_222_NNPDF30NNLO_llll.DAOD_SUSY2.e5894_s3126_r9364_p4189
mc16_13TeV.364253.Sherpa_222_NNPDF30NNLO_lllv.DAOD_SUSY2.e5916_s3126_r9364_p4189
mc16_13TeV.364254.Sherpa_222_NNPDF30NNLO_llvv.DAOD_SUSY2.e5916_s3126_r9364_p4189
mc16_13TeV.364255.Sherpa_222_NNPDF30NNLO_lvvv.DAOD_SUSY2.e5916_s3126_r9364_p4189
mc16_13TeV.364288.Sherpa_222_NNPDF30NNLO_llll_lowMllPtComplement.DAOD_SUSY2.e6096_s3126_r9364_p4189
mc16_13TeV.364289.Sherpa_222_NNPDF30NNLO_lllv_lowMllPtComplement.DAOD_SUSY2.e6133_s3126_r9364_p4189
mc16_13TeV.364290.Sherpa_222_NNPDF30NNLO_llvv_lowMllPtComplement.DAOD_SUSY2.e6096_s3126_r9364_p4189
mc16_13TeV.364302.Sherpa_222_NNPDF30NNLO_ggZllZqq.DAOD_SUSY2.e6273_s3126_r9364_p4189
mc16_13TeV.364303.Sherpa_222_NNPDF30NNLO_ggZvvZqq.DAOD_SUSY2.e6273_s3126_r9364_p4189
mc16_13TeV.364304.Sherpa_222_NNPDF30NNLO_ggWmlvWpqq.DAOD_SUSY2.e6273_s3126_r9364_p4189
mc16_13TeV.364305.Sherpa_222_NNPDF30NNLO_ggWplvWmqq.DAOD_SUSY2.e6273_s3126_r9364_p4189
mc16_13TeV.366086.Sh_222_NN30NNLO_llljj_Min_N_TChannel.DAOD_SUSY2.e7448_s3126_r9364_p4189
mc16_13TeV.366087.Sh_222_NN30NNLO_lllvjj_Min_N_TChannel.DAOD_SUSY2.e7448_s3126_r9364_p4189
mc16_13TeV.366088.Sh_222_NN30NNLO_llvvjj_ss_Min_N_TChannel.DAOD_SUSY2.e7448_s3126_r9364_p4189
mc16_13TeV.366089.Sh_222_NN30NNLO_llvvjj_Min_N_TChannel.DAOD_SUSY2.e7448_s3126_r9364_p4189

Higgs
mc16_13TeV.345053.PowhegPythia8EvtGen_NNPDF3_AZNLO_WmH125J_MINLO_lvbb_VpT.DAOD_SUSY2.e5706_s3126_r9364_p4189
mc16_13TeV.345054.PowhegPythia8EvtGen_NNPDF3_AZNLO_WpH125J_MINLO_lvbb_VpT.DAOD_SUSY2.e5706_s3126_r9364_p4838
mc16_13TeV.345055.PowhegPythia8EvtGen_NNPDF3_AZNLO_ZH125J_MINLO_llbb_VpT.DAOD_SUSY2.e5706_s3126_r9364_p4458
mc16_13TeV.345057.PowhegPythia8EvtGen_NNPDF3_AZNLO_ggZH125_llbb.DAOD_SUSY2.e5706_s3126_r9364_p4458
mc16_13TeV.345113.PowhegPythia8EvtGen_NNPDF3_AZNLO_ggZH125_llcc.DAOD_SUSY2.e5765_s3126_r9364_p4189
mc16_13TeV.345120.PowhegPy8EG_NNLOPS_nnlo_30_ggH125_tautaul13l7.DAOD_SUSY2.e5814_s3126_r9364_p4189
mc16_13TeV.345121.PowhegPy8EG_NNLOPS_nnlo_30_ggH125_tautaulm15hp20.DAOD_SUSY2.e5814_s3126_r9364_p4189
mc16_13TeV.345122.PowhegPy8EG_NNLOPS_nnlo_30_ggH125_tautaulp15hm20.DAOD_SUSY2.e5814_s3126_r9364_p4189
mc16_13TeV.345123.PowhegPy8EG_NNLOPS_nnlo_30_ggH125_tautauh30h20.DAOD_SUSY2.e5814_s3126_r9364_p4189
mc16_13TeV.345211.PowhegPy8EG_NNPDF30_AZNLO_WmH125J_Winc_MINLO_tautau.DAOD_SUSY2.e5808_s3126_r9364_p4458
mc16_13TeV.345212.PowhegPy8EG_NNPDF30_AZNLO_WpH125J_Winc_MINLO_tautau.DAOD_SUSY2.e5808_s3126_r9364_p4458
mc16_13TeV.345217.PowhegPy8EG_NNPDF30_AZNLO_ZH125J_Zinc_MINLO_tautau.DAOD_SUSY2.e5808_s3126_r9364_p4458
mc16_13TeV.345324.PowhegPythia8EvtGen_NNLOPS_NN30_ggH125_WWlvlv_EF_15_5.DAOD_SUSY2.e5769_s3126_r9364_p4458
mc16_13TeV.345325.PowhegPythia8EvtGen_NNPDF3_AZNLO_WpH125J_MINLO_qqWWlvlv.DAOD_SUSY2.e5811_s3126_r9364_p4458
mc16_13TeV.345336.PowhegPythia8EvtGen_NNPDF3_AZNLO_ZH125J_MINLO_qqWWlvlv.DAOD_SUSY2.e5813_s3126_r9364_p4189
mc16_13TeV.345433.PowhegPythia8EvtGen_NNPDF3_AZNLO_WmH125J_MINLO_qqWWlvlv.DAOD_SUSY2.e5811_s3126_r9364_p4458
mc16_13TeV.345948.PowhegPy8EG_NNPDF30_AZNLOCTEQ6L1_VBFH125_WWlvlv.DAOD_SUSY2.e7172_s3126_r9364_p4458
mc16_13TeV.345949.PowhegPythia8EvtGen_NNPDF30_AZNLOCTEQ6L1_VBFH125_bb.DAOD_SUSY2.e7252_s3126_r9364_p4189
mc16_13TeV.346190.PowhegPy8EG_NNPDF30_AZNLOCTEQ6L1_VBFH125_tautaul13l7.DAOD_SUSY2.e7259_s3126_r9364_p4458
mc16_13TeV.346191.PowhegPy8EG_NNPDF30_AZNLOCTEQ6L1_VBFH125_tautaulm15hp20.DAOD_SUSY2.e7259_s3126_r9364_p4458
mc16_13TeV.346192.PowhegPy8EG_NNPDF30_AZNLOCTEQ6L1_VBFH125_tautaulp15hm20.DAOD_SUSY2.e7259_s3126_r9364_p4458
mc16_13TeV.346193.PowhegPy8EG_NNPDF30_AZNLOCTEQ6L1_VBFH125_tautauh30h20.DAOD_SUSY2.e7259_s3126_r9364_p4458
mc16_13TeV.346343.PhPy8EG_A14NNPDF23_NNPDF30ME_ttH125_allhad.DAOD_SUSY2.e7148_s3126_r9364_p4189
mc16_13TeV.346344.PhPy8EG_A14NNPDF23_NNPDF30ME_ttH125_semilep.DAOD_SUSY2.e7148_s3126_r9364_p4189
mc16_13TeV.346345.PhPy8EG_A14NNPDF23_NNPDF30ME_ttH125_dilep.DAOD_SUSY2.e7148_s3126_r9364_p4189
mc16_13TeV.346524.PowhegPythia8EvtGen_NNPDF3_AZNLO_ggZH125J_MINLO_ZinclWWlvlv.DAOD_SUSY2.e7523_s3126_r9364_p4189
mc16_13TeV.346560.PowhegPythia8EvtGen_NNPDF3_AZNLO_WmH125J_MINLO_lvWWlvqq.DAOD_SUSY2.e7552_s3126_r9364_p4458
mc16_13TeV.346561.PowhegPythia8EvtGen_NNPDF3_AZNLO_WpH125J_MINLO_lvWWlvqq.DAOD_SUSY2.e7552_s3126_r9364_p4458

A.8 Cutflow of SR, CR and VR

Table A.3: Cutflow of Signal Region Selection defined in Table 5.5.

Cut	$ssWWH, \kappa_\lambda = 1$	$t\bar{t}$	stop	$t\bar{t} + V$	$Z \to ll$	Diboson	Higgs	Wjets
Base cut (2 leptons), Trigger matching	0.5499 ± 0.0015	4079000 ± 600	161570 ± 150	9120 ± 11	3179000 ± 4955	36050 ± 46	4833.7 ± 3.7	271 ± 6
Same charge	0.5458 ± 0.0015	27060 ± 50	1890 ± 13	1798 ± 4	9850 ± 213	1233 ± 7	484.9 ± 0.9	124 ± 4
NAllJets>=4	0.4484 ± 0.0013	16590 ± 40	720 ± 8	1512 ± 3	3340 ± 83	557.5 ± 3.8	413.3 ± 0.8	76 ± 3
NBJets>=2	0.2168 ± 0.0009	5610 ± 23	128 ± 4	736 ± 2	350 ± 22	52.6 ± 1.1	209.9 ± 0.6	6.4 ± 0.7
MET >= 30 GeV	0.1971 ± 0.0009	4840 ± 22	111 ± 4	655 ± 2	140 ± 18	38.2 ± 0.9	187.1 ± 0.5	5.1 ± 0.6
VBFJet Pt >25	0.1754 ± 0.0008	3640 ± 19	80 ± 3	576 ± 2	100 ± 17	31.1 ± 0.8	172.5 ± 0.5	4.2 ± 0.6
BJet Pt >25	0.1628 ± 0.0008	3280 ± 18	71 ± 3	533 ± 2	75 ± 16	22.9 ± 0.6	159.6 ± 0.5	3.1 ± 0.5
Lepton Pt >25	0.1337 ± 0.0007	2130 ± 14	44 ± 2	398 ± 2	70 ± 3	16.0 ± 0.4	103.16 ± 0.39	0.14 ± 0.08
VBS cuts njj>3	0.1136 ± 0.0007	1260 ± 11	28 ± 2	191 ± 1	46 ± 3	9.2 ± 0.3	55.46 ± 0.29	0.11 ± 0.07
VBS cuts mjj >900	0.0816 ± 0.0006	360 ± 6	6.4 ± 0.9	43.9 ± 0.6	16 ± 2	2.67 ± 0.15	13.19 ± 0.15	0.07 ± 0.07
Bmass window: 100 GeV <m_{bb} <160 GeV	0.0596 ± 0.0005	100 ± 3	1.63 ± 0.43	11.3 ± 0.3	4.5 ± 1.2	0.54 ± 0.06	3.73 ± 0.09	0.0
DRbb <2	0.0505 ± 0.0004	37.1 ± 1.8	0.95 ± 0.32	5.1 ± 0.2	1.4 ± 0.2	0.31 ± 0.05	1.63 ± 0.07	0.0

Table A.4: Cutflow of Control Region Selection defined in Table 5.5.

Cut	$ssWWH, \kappa_\lambda = 1$	$t\bar{t}$	stop	$t\bar{t} + V$	$Z \to ll$	Diboson	Higgs	Wjets
Base cut (2 leptons), Trigger matching	0.5499 ± 0.0015	4079000 ± 600	161570 ± 150	9120 ± 11	3179000 ± 5000	36050 ± 40	4833.7 ± 3.7	271 ± 6
Same charge	0.5458 ± 0.0015	27060 ± 50	1894 ± 13	1798.1 ± 3.7	9850 ± 210	1233 ± 7	484.9 ± 0.9	124 ± 4
NAllJets>=4	0.4484 ± 0.0013	16590 ± 40	720 ± 8	1512.2 ± 3.5	3340 ± 80	557 ± 4	413.3 ± 0.8	75.6 ± 3.1
NBJets>=2	0.2168 ± 0.0009	5610 ± 23	128.1 ± 3.7	735.9 ± 2.4	353 ± 22	52.6 ± 1.1	209.9 ± 0.6	6.4 ± 0.7
MET >= 30 GeV	0.1971 ± 0.0009	4837 ± 22	110.7 ± 3.5	655.5 ± 2.3	140 ± 18	38.2 ± 0.9	187.1 ± 0.5	5.1 ± 0.6
VBFJet Pt >25	0.1754 ± 0.0008	3643 ± 19	80 ± 3	576.5 ± 2.1	100 ± 17	31.1 ± 0.8	172.5 ± 0.5	4.2 ± 0.6
BJet Pt >25	0.1628 ± 0.0008	3278 ± 18	70.7 ± 2.8	533.3 ± 2.1	75 ± 16	22.9 ± 0.6	159.6 ± 0.5	3.1 ± 0.5
Lepton Pt >25	0.1337 ± 0.0007	2130 ± 14	43.9 ± 2.4	397.7 ± 1.8	70.1 ± 3.1	16.0 ± 0.4	103.2 ± 0.4	0.14 ± 0.08
inverted VBS cuts njj<3	0.0201 ± 0.0003	866 ± 9	16.3 ± 1.5	206.7 ± 1.3	24.0 ± 1.3	6.6 ± 0.3	47.7 ± 0.3	0.04 ± 0.02

Table A.5: Cutflow of Validation Region Selection defined in Table 5.5.

Cut	$ssWWH, \kappa_\lambda = 1$	$t\bar{t}$	stop	$t\bar{t} + V$	$Z \to ll$	Diboson	Higgs	Wjets
Base cut (2 leptons), Trigger matching	0.5499 ± 0.0015	4079000 ± 600	161570 ± 150	9120 ± 10	3179000 ± 5000	36051.7249 ± 46.1702	4833.7445 ± 3.6823	271.1225 ± 5.6775
Same charge	0.5458 ± 0.0015	27060 ± 50	1894 ± 13	1798 ± 4	9850 ± 210	1233.4505 ± 7.4426	484.9436 ± 0.9120	123.7037 ± 4.0397
NAllJets>=4	0.4484 ± 0.0013	16590 ± 40	720 ± 8	1512.2 ± 3.5	3340 ± 80	557.4782 ± 3.7798	413.2737 ± 0.8129	75.6122 ± 3.1044
NBJets>=2	0.2168 ± 0.0009	5612 ± 23	128 ± 4	735.9 ± 2.4	352 ± 22	52.5725 ± 1.1385	209.9163 ± 0.5632	6.3787 ± 0.6931
MET >= 30 GeV	0.1971 ± 0.0009	4837 ± 22	111 ± 3.5	655.5 ± 2.3	140 ± 18	38.1563 ± 0.8602	187.1368 ± 0.5279	5.1308 ± 0.6266
VBFJet Pt >25	0.1754 ± 0.0008	3640 ± 19	80 ± 3	576 ± 2	100 ± 17	31.1 ± 0.8	172.5 ± 0.5	4.2 ± 0.6
BJet Pt >25	0.1628 ± 0.0008	3280 ± 18	71 ± 3	533 ± 2	75 ± 16	22.9 ± 0.6	159.6 ± 0.5	3.1 ± 0.5
Lepton Pt >25	0.1337 ± 0.0007	2130 ± 14	44 ± 2	398 ± 2	70 ± 3	16.0 ± 0.4	103.16 ± 0.39	0.14 ± 0.08
VBS cuts njj>3	0.1136 ± 0.0007	1260 ± 11	28 ± 2	191 ± 1	46 ± 3	9.2 ± 0.3	55.46 ± 0.29	0.11 ± 0.07
VBS cuts mjj >900	0.0816 ± 0.0006	360 ± 6	6.4 ± 0.9	43.9 ± 0.6	16 ± 2	2.67 ± 0.15	13.19 ± 0.15	0.07 ± 0.07
Bmass window: $70GeV > m_{bb} \vert\vert m_{bb} > 160GeV$	0.0049 ± 0.0001	211 ± 4	3.8 ± 0.7	27.4 ± 0.4	8.9 ± 1.6	1.61 ± 0.12	7.92 ± 0.11	0.07 ± 0.07

Appendix - Memes

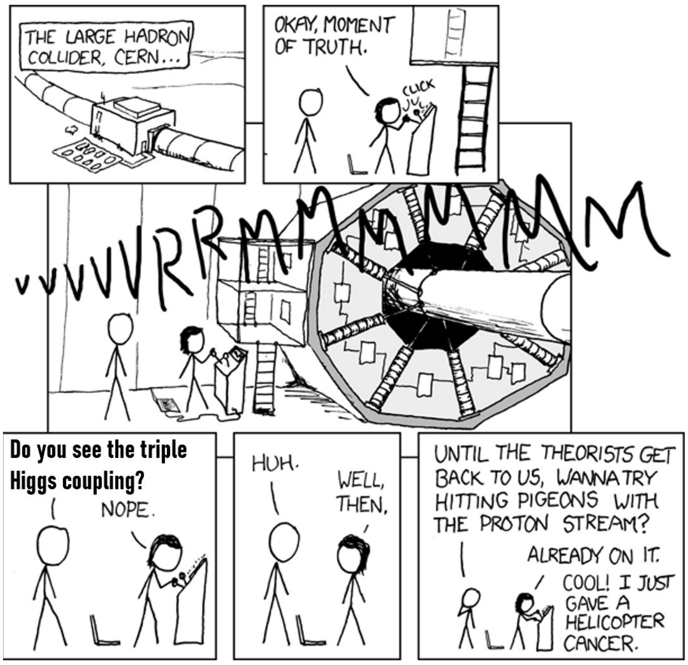

Taken and adapted from [91].

List of Figures

List of Tables

Bibliography

[1] G. Aad *et al.* ‘Observation of a New Particle in the Search for the Standard Model Higgs Boson with the ATLAS Detector at the LHC’. In: *Physics Letters B* 716 (17th Sept. 2012), pp. 1–29 (cit. on p. 1).

[2] *Dark Matter*. CERN. 10th Apr. 2024. URL: `https://home.cern/science/physics/dark-matter` (visited on 23/04/2024) (cit. on p. 1).

[3] *The Matter-Antimatter Asymmetry Problem*. CERN. 10th Apr. 2024. URL: `https://home.cern/science/physics/matter-antimatter-asymmetry-problem` (visited on 23/04/2024) (cit. on p. 1).

[4] T. Biekötter *et al.* ‘The Trap in the Early Universe: Impact on the Interplay between Gravitational Waves and LHC Physics in the 2HDM’. In: *JCAP* 03 (2023), p. 031. DOI: `10.1088/1475-7516/2023/03/031` (cit. on p. 1).

[5] acapellascience, director. *Rolling in the Higgs (Adele Parody) | A Capella Science*. 20th Aug. 2012. URL: `https://www.youtube.com/watch?v=VtItBX1l1VY` (visited on 23/04/2024) (cit. on p. 1).

[6] T. A. Collaboration *et al.* ‘The ATLAS Experiment at the CERN Large Hadron Collider’. In: *J. Inst.* 3.08 (14th Aug. 2008), S08003–S08003. ISSN: 1748-0221. DOI: `10.1088/1748-0221/3/08/S08003` (cit. on pp. 1, 18, 19).

[7] C. Englert *et al.* *VBS W+-W+-H Production at the HL-LHC and a 100 TeV Pp-Collider*. 7th Feb. 2017. DOI: `10.48550/arXiv.1702.01930`. arXiv: `1702.01930 [hep-ex, physics:hep-ph]`. preprint (cit. on pp. 2, 14).

[8] B. Henning *et al.* ‘Higgs Couplings without the Higgs’. In: *Phys. Rev. Lett.* 123.18 (29th Oct. 2019), p. 181801. ISSN: 0031-9007, 1079-7114. DOI: `10.1103/PhysRevLett.123.181801`. arXiv: `1812.09299 [hep-ex, physics:hep-ph]` (cit. on pp. 2, 14, 31, 52, 57, 58, 59, 60).

[9] J. Chen *et al.* ‘Measuring Higgs Boson Self-couplings with $2\rightarrow 3$ VBS Processes’. In: *J. High Energ. Phys.* 2021.10 (13th Oct. 2021), p. 99. ISSN: 1029-8479. DOI: `10.1007/JHEP10(2021)099`. arXiv: `2105.11500 [hep-ph]` (cit. on pp. 2, 14).

[10] M. Thomson. *Modern Particle Physics*. Higher Education from Cambridge University Press. 5th Sept. 2013. DOI: `10.1017/CBO9781139525367` (cit. on p. 3).

[11] Arno Straessner. *Lecture on "Higgs and Beyond Standard Model Physics"; Winter Term 2022/2023* (cit. on p. 3).

[12] Frank Siegert. *Lecture Notes of "Vertiefende Grundlagen Der Teilchenphysik"; Summer Term 2023* (cit. on p. 3).

[13] M. Kobel et al. *Teilchenphysik - Unterrichtsmaterial Ab Klasse 10*. 2022 (cit. on pp. 3, 6).

[14] *Standard Model of Elementary Particles.* URL: https://upload.wikimedia.org/wikipedia/commons/0/00/Standard_Model_of_Elementary_Particles.svg (visited on 26/01/2024) (cit. on p. 4).

[15] C. S. Wu *et al.* 'Experimental Test of Parity Conservation in Beta Decay'. In: *Phys. Rev.* 105.4 (15th Feb. 1957), pp. 1413–1415. DOI: 10.1103/PhysRev.105.1413 (cit. on p. 6).

[16] P. W. Higgs. 'Spontaneous Symmetry Breakdown without Massless Bosons'. In: *Phys. Rev.* 145.4 (27th May 1966), pp. 1156–1163. DOI: 10.1103/PhysRev.145.1156 (cit. on p. 8).

[17] F. Englert *et al.* 'Broken Symmetry and the Mass of Gauge Vector Mesons'. In: *Phys. Rev. Lett.* 13.9 (31st Aug. 1964), pp. 321–323. DOI: 10.1103/PhysRevLett.13.321 (cit. on p. 8).

[18] K. Leney. *Recent searches for Higgs boson pair-production at ATLAS.* Indico. 23rd Nov. 2021. URL: https://indico.cern.ch/event/1065153/ (visited on 22/04/2024) (cit. on p. 9).

[19] Y. Nambu. 'Quasi-Particles and Gauge Invariance in the Theory of Superconductivity'. In: *Phys. Rev.* 117.3 (1st Feb. 1960), pp. 648–663. DOI: 10.1103/PhysRev.117.648 (cit. on p. 9).

[20] J. Goldstone *et al.* 'Broken Symmetries'. In: *Phys. Rev.* 127.3 (1st Aug. 1962), pp. 965–970. DOI: 10.1103/PhysRev.127.965 (cit. on p. 9).

[21] T. A. Collaboration. 'Observation of a New Particle in the Search for the Standard Model Higgs Boson with the ATLAS Detector at the LHC'. In: *Physics Letters B* 716.1 (Sept. 2012), pp. 1–29. ISSN: 03702693. DOI: 10.1016/j.physletb.2012.08.020. arXiv: 1207.7214 [hep-ex] (cit. on pp. 11, 17).

[22] T. C. Collaboration. 'Observation of a New Boson at a Mass of 125 GeV with the CMS Experiment at the LHC'. In: *Physics Letters B* 716.1 (Sept. 2012), pp. 30–61. ISSN: 03702693. DOI: 10.1016/j.physletb.2012.08.021. arXiv: 1207.7235 [hep-ex] (cit. on p. 11).

[23] ATLAS Collaboration *et al.* 'Observation of Electroweak Production of a Same-Sign W Boson Pair in Association with Two Jets in pp Collisions at 13 TeV with the ATLAS Detector'. In: *Phys. Rev. Lett.* 123.16 (15th Oct. 2019), p. 161801. DOI: 10.1103/PhysRevLett.123.161801 (cit. on pp. 12, 13, 14, 43).

[24] C. Collaboration. 'Observation of Electroweak Production of Same-Sign W Boson Pairs in the Two Jet and Two Same-Sign Lepton Final State in Proton-Proton Collisions at $\13 TeV'. In: *Phys. Rev. Lett.* 120.8 (22nd Feb. 2018), p. 081801. ISSN: 0031-9007, 1079-7114. DOI: 10.1103/PhysRevLett.120.081801. arXiv: 1709.05822 [hep-ex] (cit. on p. 12).

[25] M. S. Chanowitz *et al.* 'The TeV Physics of Strongly Interacting W's and Z's'. In: *Nuclear Physics B* 261 (1st Jan. 1985), pp. 379–431. ISSN: 0550-3213. DOI: 10.1016/0550-3213(85)90580-2 (cit. on p. 12).

[26] P. Agrawal *et al.* 'Determining the Shape of Higgs Potential at Future Colliders'. In: *Phys. Rev. D* 101.7 (15th Apr. 2020), p. 075023. ISSN: 2470-0010, 2470-0029. DOI: 10.1103/PhysRevD.101.075023. arXiv: 1907.02078 [hep-ex, physics:hep-ph] (cit. on p. 12).

[27] A. Noble *et al.* 'Higgs Self-Coupling as a Probe of Electroweak Phase Transition'. In: *Phys. Rev. D* 78.6 (11th Sept. 2008), p. 063518. ISSN: 1550-7998, 1550-2368. DOI: 10.1103/PhysRevD.78.063518. arXiv: 0711.3018 [hep-ph] (cit. on p. 12).

[28] *DiHiggs Graphic Design Department.* URL: https://twiki.cern.ch/twiki/bin/viewauth/AtlasProtected/HHGDD (visited on 16/04/2024) (cit. on p. 12).

[29] G. Aad *et al.* 'Search for Non-Resonant Higgs Boson Pair Production in the 2b+2l+met final State in Pp Collisions at 13 TeV with the ATLAS Detector'. In: *J. High Energ. Phys.* 2024.2 (7th Feb. 2024), p. 37. ISSN: 1029-8479. DOI: 10.1007/JHEP02(2024)037 (cit. on pp. 13, 41, 42, 44, 45, 46, 53, 70).

[30] ATLAS Collaboration *et al.* 'Search for Higgs Boson Pair Production in the Two Bottom Quarks plus Two Photons Final State in pp Collisions at 13 TeV with the ATLAS Detector'. In: *Phys. Rev. D* 106.5 (6th Sept. 2022), p. 052001. DOI: 10.1103/PhysRevD.106.052001 (cit. on pp. 13, 58, 60).

[31] M. Grazzini *et al.* 'Higgs Boson Pair Production at NNLO with Top Quark Mass Effects'. In: *J. High Energ. Phys.* 2018.5 (May 2018), p. 59. ISSN: 1029-8479. DOI: 10.1007/JHEP05(2018)059 (cit. on pp. 13, 14).

[32] F. A. Dreyer *et al.* 'Vector-Boson Fusion Higgs Pair Production at NNNLO'. In: *Phys. Rev. D* 98.11 (17th Dec. 2018), p. 114016. DOI: 10.1103/PhysRevD.98.114016 (cit. on pp. 13, 14).

[33] S. Todt. 'The W+-W+- Scattering Process - Theoretical Studies, Observation, Cross-section Measurement, and EFT Reinterpretation at 13 TeV with the ATLAS Detector'. PhD thesis. Dresden, Tech. U., Sept. 2022 (cit. on pp. 14, 31).

[34] B. Di Micco *et al.* 'Higgs Boson Potential at Colliders: Status and Perspectives'. In: *Reviews in Physics* 5 (Nov. 2020), p. 100045. ISSN: 24054283. DOI: 10.1016/j.revip.2020.100045. arXiv: 1910.00012 [hep-ex, physics:hep-ph] (cit. on pp. 14, 15, 57).

[35] G. D. Kribs *et al.* 'Electroweak Oblique Parameters as a Probe of the Trilinear Higgs Boson Self-Interaction'. In: *Phys. Rev. D* 95.9 (30th May 2017), p. 093004. ISSN: 2470-0010, 2470-0029. DOI: 10.1103/PhysRevD.95.093004. arXiv: 1702.07678 [hep-ph] (cit. on p. 14).

[36] F. Bishara *et al.* 'Higgs Pair Production in Vector-Boson Fusion at the LHC and Beyond'. In: *Eur. Phys. J. C* 77.7 (July 2017), p. 481. ISSN: 1434-6044, 1434-6052. DOI: 10.1140/epjc/s10052-017-5037-9. arXiv: 1611.03860 [hep-ex, physics:hep-ph] (cit. on pp. 15, 32, 61).

[37] G. Degrassi *et al.* 'Probing the Higgs Self Coupling via Single Higgs Production at the LHC'. In: *J. High Energ. Phys.* 2016.12 (Dec. 2016), p. 80. ISSN: 1029-8479. DOI: 10.1007/JHEP12(2016)080. arXiv: 1607.04251 [hep-ph] (cit. on pp. 15, 57).

[38] *CERN Experiment Traps Antimatter Atoms for 1000 Seconds*. CERN. 10th Apr. 2024. URL: https://home.web.cern.ch/news/press-release/cern/cern-experiment-traps-antimatter-atoms-1000-seconds (visited on 20/04/2024) (cit. on p. 17).

[39] *ISOLDE Takes a Solid Tick Forward towards a Nuclear Clock*. CERN. 10th Apr. 2024. URL: https://home.cern/news/news/physics/isolde-takes-solid-tick-forward-towards-nuclear-clock (visited on 20/04/2024) (cit. on p. 17).

[40] F. Landua. *The CERN Accelerator Complex Layout in 2022. Complexe Des Accélérateurs Du CERN En Janvier 2022*. 2022. URL: https://cds.cern.ch/record/2813716 (visited on 19/04/2024) (cit. on p. 18).

[41] L. Evans *et al.* 'LHC Machine'. In: *J. Inst.* 3.08 (Aug. 2008), S08001. ISSN: 1748-0221. DOI: 10.1088/1748-0221/3/08/S08001 (cit. on p. 17).

[42] T. C. Collaboration *et al.* 'The CMS Experiment at the CERN LHC'. In: *J. Inst.* 3.08 (Aug. 2008), S08004. ISSN: 1748-0221. DOI: 10.1088/1748-0221/3/08/S08004 (cit. on p. 18).

[43] T. A. Collaboration *et al.* 'The ALICE Experiment at the CERN LHC'. In: *J. Inst.* 3.08 (Aug. 2008), S08002. ISSN: 1748-0221. DOI: 10.1088/1748-0221/3/08/S08002 (cit. on p. 18).

[44] T. Lhc. Collaboration *et al.* 'The LHCb Detector at the LHC'. In: *J. Inst.* 3.08 (Aug. 2008), S08005. ISSN: 1748-0221. DOI: 10.1088/1748-0221/3/08/S08005 (cit. on p. 18).

[45] M. Lamont. *The First Years of LHC Operation for Luminosity Production*. 2013. URL: https://cds.cern.ch/record/2010134 (cit. on p. 18).

[46] F. Pastore. 'The ATLAS Trigger System: Past, Present and Future'. In: *Nuclear and Particle Physics Proceedings*. 37th International Conference on High Energy Physics (ICHEP) 273–275 (1st Apr. 2016), pp. 1065–1071. ISSN: 2405-6014. DOI: 10.1016/j.nuclphysbps.2015.09.167 (cit. on p. 22).

[47] M. H. Seymour *et al. Monte Carlo Event Generators*. 24th Apr. 2013. arXiv: 1304.6677 [hep-ph]. preprint (cit. on p. 22).

[48] T. Gleisberg *et al.* 'Event Generation with SHERPA 1.1'. In: *J. High Energy Phys.* 2009.02 (3rd Feb. 2009), pp. 007–007. ISSN: 1029-8479. DOI: 10.1088/1126-6708/2009/02/007. arXiv: 0811.4622 [hep-ph] (cit. on pp. 22, 23).

[49] A. Buckley *et al.* 'General-Purpose Event Generators for LHC Physics'. In: *Physics Reports* 504.5 (July 2011), pp. 145–233. ISSN: 03701573. DOI: 10.1016/j.physrep.2011.03.005. arXiv: 1101.2599 [hep-ex, physics:hep-ph] (cit. on p. 22).

[50] C. Degrande *et al.* 'UFO - The Universal FeynRules Output'. In: *Computer Physics Communications* 183.6 (June 2012), pp. 1201–1214. ISSN: 00104655. DOI: 10.1016/j.cpc.2012.01.022. arXiv: 1108.2040 [hep-ph] (cit. on p. 22).

[51] T. A. Collaboration. 'The ATLAS Simulation Infrastructure'. In: *Eur. Phys. J. C* 70.3 (Dec. 2010), pp. 823–874. ISSN: 1434-6044, 1434-6052. DOI: 10.1140/epjc/s10052-010-1429-9. arXiv: 1005.4568 [hep-ex, physics:physics] (cit. on p. 23).

[52] J. Alwall *et al.* 'The Automated Computation of Tree-Level and next-to-Leading Order Differential Cross Sections, and Their Matching to Parton Shower Simulations'. In: *J. High Energ. Phys.* 2014.7 (July 2014), p. 79. ISSN: 1029-8479. DOI: 10.1007/JHEP07(2014)079. arXiv: 1405.0301 [hep-ph] (cit. on p. 24).

[53] C. Bierlich *et al. A Comprehensive Guide to the Physics and Usage of PYTHIA 8.3.* 22nd Mar. 2022. arXiv: 2203.11601 [hep-ex, physics:hep-ph]. preprint (cit. on pp. 24, 61).

[54] S. Agostinelli *et al.* 'Geant4—a Simulation Toolkit'. In: *Nuclear Instruments and Methods in Physics Research Section A: Accelerators, Spectrometers, Detectors and Associated Equipment* 506.3 (1st July 2003), pp. 250–303. ISSN: 0168-9002. DOI: 10.1016/S0168-9002(03)01368-8 (cit. on pp. 24, 41).

[55] J. Allison *et al.* 'Recent Developments in Geant4'. In: *Nuclear Instruments and Methods in Physics Research Section A: Accelerators, Spectrometers, Detectors and Associated Equipment* 835 (1st Nov. 2016), pp. 186–225. ISSN: 0168-9002. DOI: 10.1016/j.nima.2016.06.125 (cit. on pp. 24, 41).

[56] *ATLAS Computing: Technical Design Report.* Geneva: CERN, 2005. URL: https://cds.cern.ch/record/837738 (cit. on pp. 24, 27).

[57] *Terascale Statistics School 2024.* DESY-Konferenzverwaltung (Indico). 2nd Apr. 2024. URL: https://indico.desy.de/event/43398/ (cit. on p. 24).

[58] G. Cowan *et al.* 'Asymptotic Formulae for Likelihood-Based Tests of New Physics'. In: *Eur. Phys. J. C* 71.2 (Feb. 2011), p. 1554. ISSN: 1434-6044, 1434-6052. DOI: 10.1140/epjc/s10052-011-1554-0. arXiv: 1007.1727 [hep-ex, physics:physics] (cit. on pp. 25, 54, 58).

[59] T. Herrmann. 'Total and Differential Cross-Section Measurement and Interpretation of W+- W+- Scattering in Effective Field Theories with the Run 2 Data of the ATLAS Experiment'. PhD thesis. TU Dresden, 13th Sept. 2023 (cit. on p. 25).

[60] *ATLAS Analysis Software Tutorial.* ATLAS Software Documentation. URL: https://atlassoftwaredocs.web.cern.ch/ASWTutorial/ (visited on 19/04/2024) (cit. on p. 28).

[61] R. Brun *et al.* 'ROOT — An Object Oriented Data Analysis Framework'. In: *Nuclear Instruments and Methods in Physics Research Section A: Accelerators, Spectrometers, Detectors and Associated Equipment.* New Computing Techniques in Physics Research V 389.1 (11th Apr. 1997), pp. 81–86. ISSN: 0168-9002. DOI: 10.1016/S0168-9002(97)00048-X (cit. on p. 28).

[62] L. M. Lehmann. *Truth-Level Analysis of VBS ssWWh.* GitLab. 14th Mar. 2024. URL: https://gitlab.cern.ch/lmlehman/masterproject-analysis/ (cit. on p. 28).

[63] S. Alekhin *et al.* 'The 3, 4, and 5-Flavor NNLO Parton from Deep-Inelastic-Scattering Data and at Hadron Colliders'. In: *Phys. Rev. D* 81 (2010), p. 014032. DOI: 10.1103/PhysRevD.81.014032 (cit. on p. 29).

[64] A. S. Tegetmeier. *[ATLMCPROD-10785] Non-resonant VBF HH->bbyy Signal Request - CERN Central Jira.* URL: https://its.cern.ch/jira/browse/ATLMCPROD-10785 (visited on 19/04/2024) (cit. on p. 29).

[65] G. Aad *et al.* 'Observation of Gauge Boson Joint-Polarisation States in W+- Z Production from pp Collisions at TeV with the ATLAS Detector'. In: *Physics Letters B* 843 (10th Aug. 2023), p. 137895. ISSN: 0370-2693. DOI: 10.1016/j.physletb.2023.137895 (cit. on p. 29).

[66] C. Bittrich. 'Evidence for Scattering of Electroweak Gauge Bosons in the W^\pmZ Channel with the ATLAS Detector at the Large Hadron Collider'. PhD thesis. Dresden, Tech. U., TU, Dresden (main), 2020 (cit. on p. 29).

[67] *Question #695855 "Higgs Branching Fraction to B\bar{b} Using Com..." : Questions : MadGraph5_ aMC@NLO*. Launchpad. 4th Mar. 2021. URL: https://answers.launchpad.net/mg5amcnlo/+question/695855/+index (visited on 20/04/2024) (cit. on p. 31).

[68] I. Brivio *et al.* 'The SMEFTsim Package, Theory and Tools'. In: *J. High Energ. Phys.* 2017.12 (Dec. 2017), p. 70. ISSN: 1029-8479. DOI: 10.1007/JHEP12(2017)070 (cit. on p. 32).

[69] *Higgs/HHVBF_ UFO*. GitLab. 19th Sept. 2023. URL: https://gitlab.cern.ch/atlas-generators-team/MadGraphModels/-/tree/main/Higgs/HHVBF_UFO (visited on 19/04/2024) (cit. on pp. 32, 61).

[70] *[AGENE-2264] Wrong HardScatterParticles Information in TRUTH3 in Re23 - CERN Central Jira*. URL: https://its.cern.ch/jira/browse/AGENE-2264 (visited on 20/04/2024) (cit. on p. 35).

[71] O. Kolay *et al. QT Report: Sherpa Diphoton Bulk Samples and Studies on Phase Space Biasing*. Geneva: CERN, 2023. URL: https://cds.cern.ch/record/2860089 (cit. on p. 35).

[72] D. Abbott *et al. Supporting Document: The Search for Non-Resonant ggF and VBF HH Production Decaying to the 4b Final State Using the Full Run-2 Data*. Geneva: CERN, 2021. URL: https://cds.cern.ch/record/2780536 (cit. on p. 35).

[73] A. S. Tegetmeier. 'Multivariate Analysis of Polarized Vector Boson Scattering of a W and Z Boson with the ATLAS Detector'. Technische Universitaet Dresden (DE), 2022 (cit. on p. 36).

[74] J.-E. Nitschke. 'Studies on Polarization in the Scattering of Two Vector Bosons with the ATLAS Experiment at the LHC'. Technische Universitaet Dresden (DE), 8th June 2021. URL: https://cds.cern.ch/record/2771952 (cit. on p. 39).

[75] *[ATLMCPROD-10816] Request for ssWWhjj Signal (W Decay Leptonically, H>bb) - CERN Central Jira*. URL: https://its.cern.ch/jira/browse/ATLMCPROD-10816 (cit. on p. 41).

[76] *The SUSY2 Production Code*. GitLab. 19th Oct. 2020. URL: https://gitlab.cern.ch/atlas/athena/blob/21.2/PhysicsAnalysis/DerivationFramework/DerivationFrameworkSUSY/share/SUSY2.py (visited on 21/04/2024) (cit. on p. 41).

[77] *Overview on the SUSYxAODDerivations Software*. URL: https://twiki.cern.ch/twiki/bin/viewauth/AtlasProtected/SUSYxAODDerivationsr20#Release_21_2_X_git (visited on 21/04/2024) (cit. on p. 41).

[78] *Collection of CxAODFramework Packages for the HH->bbll Analysis*. GitLab. 4th Oct. 2022. URL: `https://gitlab.cern.ch/atlas-physics/HDBS/DiHiggs/bbll/CxAODFramework` (visited on 21/04/2024) (cit. on p. 41).

[79] M. J. R. Olsson *et al. Search for Higgs Boson Pair Production in 2b+2l+E^miss_ T Final States in Pp Collisions at \sqrts = 13 \mathrmTeV with the ATLAS Experiment*. Geneva: CERN, 2021 (cit. on p. 41).

[80] *ATLAS Common Analysis Framework*. URL: `https://atlas-caf-tutorial.web.cern.ch/` (visited on 21/04/2024) (cit. on p. 42).

[81] *Performance of the Reconstruction of Large Impact Parameter Tracks in the ATLAS Inner Detector*. Geneva: CERN, 2017. URL: `https://cds.cern.ch/record/2275635` (cit. on p. 42).

[82] J. Almond *et al. Search for Heavy Neutrino, W_ R and Z_ R Gauge Bosons in Events with Two High-P_ T Leptons and Jets with the ATLAS Detector in Pp Collisions at 8 TeV*. Geneva: CERN, 2013. URL: `https://cds.cern.ch/record/1555805` (cit. on p. 43).

[83] *Introduction to Overlap Removal*. ATLAS Software Documentation. URL: `https://atlassoftwaredocs.web.cern.ch/AnalysisSWTutorial/obj_olr_intro/` (visited on 21/04/2024) (cit. on p. 45).

[84] A. Collaboration. *Electron and Photon Efficiencies in LHC Run 2 with the ATLAS Experiment*. 25th Aug. 2023. DOI: `10.48550/arXiv.2308.13362`. arXiv: `2308.13362 [hep-ex]`. URL: `http://arxiv.org/abs/2308.13362` (visited on 21/04/2024). preprint (cit. on p. 45).

[85] A. Collaboration. 'Muon Reconstruction and Identification Efficiency in ATLAS Using the Full Run 2 pp Collision Data Set at 13 TeV'. In: *Eur. Phys. J. C* 81.7 (July 2021), p. 578. ISSN: 1434-6044, 1434-6052. DOI: `10.1140/epjc/s10052-021-09233-2`. arXiv: `2012.00578 [hep-ex]` (cit. on p. 45).

[86] M. Cacciari *et al.* 'The Anti-Kt Jet Clustering Algorithm'. In: *J. High Energy Phys.* 2008.04 (Apr. 2008), p. 063. ISSN: 1126-6708. DOI: `10.1088/1126-6708/2008/04/063` (cit. on p. 46).

[87] *Selection of Jets Produced in 13TeV Proton-Proton Collisions with the ATLAS Detector*. Geneva: CERN, 2015. URL: `https://cds.cern.ch/record/2037702` (cit. on p. 46).

[88] A. Collaboration. 'ATLAS Flavour-Tagging Algorithms for the LHC Run 2 pp Collision Dataset'. In: *Eur. Phys. J. C* 83.7 (31st July 2023), p. 681. ISSN: 1434-6052. DOI: `10.1140/epjc/s10052-023-11699-1`. arXiv: `2211.16345 [hep-ex, physics:physics]` (cit. on p. 47).

[89] C. Anastopoulos *et al. Electron Identification and Efficiency Measurements in 2017 Data*. Geneva: CERN, 2019. URL: `https://cds.cern.ch/record/2652163` (cit. on p. 50).

[90] L. M. Lehmann. *Event Generation for VBS ssWWh*. GitLab. 25th Jan. 2024. URL: `https://gitlab.cern.ch/lmlehman/masterproject-eventgeneration` (cit. on p. 61).

[91] R. Monroe. *XKCD 401*. URL: `https://xkcd.com/401/` (cit. on p. 78).

Acknowledgements

I cannot finish this project and thus my master's degree without acknowledging all the wonderful people who have supported me throughout the last year and beyond.
I am extremely grateful for the opportunity to have worked under the supervision of Joany Manjarres. Thank you for welcoming me to Toulouse and for not only being a knowledgeable supervisor but also a great mentor.
The same goes for Frank Siegert, who is a fantastic group leader and always was willing to listen to any minor or major problems.
I loved working with the VBS group in Dresden and the ATLAS group at L2IT. A big thanks is needed especially to Jan-Eric Nitschke, who was oftentimes the first call for any inconveniences MadGraph, the world or Root, had to offer and almost always helped immediately. Thank you also to Maren Bühring, Alexandro Martone, Anna Tegetmeier, Max Stange, Tim Herrmann, and Karolos Potamianos for fruitful discussions on my master's thesis work and/or for commenting on my drafts.
I am thankful for all the support my family, especially my parents, grandparents and sister gave me. We will always have each other's backs, no matter what fate brings us. Ich hab' euch lieb!
Thank you, Henrik, for being a great partner and the best supporter of all time. This year, an era of studying in Dresden is coming to an end. I am so grateful to have spent this time with friends who were willing to solve physics problems at night in bars. Thank you, Ossi, Bertolt, Birte, Daniil, Max, Joni, Friedrich and Christoph but also everyone associated to the student council.
Last but not least, I want to thank Michael Kobel, whose lectures and openness have sparked my interest in particle physics.

Erklärung

Hiermit erkläre ich, dass ich die vorliegende Arbeit im Rahmen der Betreuung am Institut für Kern- und Teilchenphysik ohne unzulässige Hilfe Dritter verfasst habe und alle verwendeten Quellen als solche gekennzeichnet habe.

Ort, Datum Unterschrift